

**Photocatalytic treatment of organic and inorganic  
water pollutants using zinc phthalocyanine- cobalt  
ferrite magnetic nanoparticle conjugates.**

**A thesis submitted in fulfilment of the requirements for the degree of**

**MASTER OF SCIENCE**

**OF**

**RHODES UNIVERSITY**

**BY**

**Sivuyisiwe Mapukata**

**MARCH 2018**

# DEDICATIONS

This thesis is dedicated to:

**My paternal grandparents**

Nzima Honey Mapukata

Nomalinge Mapukata

**My maternal grandparents**

Joseph Rhorha Mbhele

Diana Nozizwe Mbombo

**To my parents**

Griffiths Mvuyiswa Mapukata

Glory Nosisi Mapukata

**To *utatomncinci***

Mlandeli Mapukata

*Avumile amaNkwali!!*

# ACKNOWLEDGEMENTS

*“Udumo malubekuye owenza iZulu nomhlaba , Amen!”*

To my supervisor Distinguished Prof Tebello Nyokong, no words could ever be enough to express my gratitude for the guidance, motherly love and discipline as well as all the opportunities you have granted me. You have literally brought out the best in me academically and inspired me in many ways as a young black woman in science, I will forever be grateful.

To Prof Kobayashi, Prof Kimura and the students at Shinshu University, thank you for the guidance and supervision and for making my stay in Japan a pleasant one, I sure learnt a lot.

Thank you to Gail, Dr Mack, Dr Britton, Papa Francis, Marvin and Shirley for your help and individual contributions in making my academic journey a bit easier. A huge thank you to Prof Darkwa for believing in me even when I didn't believe in myself, for the motivation, advice and encouragement.

To my parents, Mvuyiswa and Nosisi Mapukata thank you for your sacrifices, prayers, motivation and support. Thank you for putting aside your wishes and desires so I could fulfil my own, for believing in me and encouraging me, couldn't have asked for better parents.

Thank you to my brothers, Mlungisi and Indiphile Mapukata, your encouragement has been amazing. To my big sister, best friend and human diary, Mbali Mapukata, thank you mntase for the financial and emotional support and for always cheering me on, I totally appreciate you. To Nozizwe Mbombo, Cikizwa Mbombo, Wendy Fipaza, and Fana Bareng thank you for the love and support and for your individual roles in raising me.

A very big thank you to the Department of Science and Technology/Mintek Nanotechnology Innovation Centre (DST/MINTEK (NIC)) as well as the National Research Foundation (NRF) for funding. A special thank you to all my friends and colleagues in S22 for the pleasant working environment and support. A big thank you to Drs Osifeko, Oluwole and Sekhosana for the help and advice with my work. To Tatenda Chatikobo and Neville Natal, you guys have been awesome and the past two years staying you have been pure bliss.

Last but not least I'd like to thank “my ride or die” Nosimo Vena for the decade of love, prayers and support, you have been nothing short of amazing.

# ABSTRACT

This work explores the synthesis and photophysical properties of zinc phthalocyanines when conjugated to cobalt ferrite magnetic nanoparticles. Phthalocyanines with amine and carboxylic acid functional groups were synthesised so as to covalently link them via amide bonds to cobalt ferrite magnetic nanoparticles with carboxylic acid and amine groups, respectively. Spectroscopic and microscopic studies confirmed the formation and purity of the phthalocyanine-cobalt ferrite magnetic nanoparticle conjugates which exhibited enhanced triplet and singlet quantum yields compared to the phthalocyanines alone. The studies showed that the presence of cobalt ferrite nanoparticles significantly lowered fluorescence quantum yields and lifetimes. The conjugates not only showed much higher singlet oxygen quantum yields compared to the phthalocyanines alone but were also attractive because of their magnetic regeneration and hence reusability properties, making them appealing for photocatalytic applications. The photocatalytic ability of some of the phthalocyanines and their conjugates were then tested based on their photooxidation and photoreduction abilities on Methyl Orange and hexavalent chromium, respectively. For catalyst support, some of the zinc phthalocyanines, cobalt ferrite magnetic nanoparticles and their respective conjugates were successfully incorporated into electrospun polystyrene and polyamide-6 fibers. Spectral characteristics of the functionalized electrospun fibers confirmed the incorporation of the photocatalysts and indicated that the phthalocyanines and their respective conjugates remained intact with their integrity maintained within the polymeric fiber matrices. The photochemical properties of the complexes were equally maintained within the electrospun fibers hence they were applied in the photooxidation of azo dyes using Orange G and Methyl Orange as model organic compounds.

# Table of Contents

Title Page.....	i
Dedications.....	ii
Acknowledgements.....	iii
Abstract.....	iv
Table of Contents.....	v
List of Symbols.....	xii
List of Abbreviations.....	xiii
<b>Chapter 1</b> .....	<b>1</b>
<b>1. Introduction.....</b>	<b>2</b>
1.1 Ferrites: Properties and Applications.....	2
1.1.1 Synthesis and Characterisation of ferrites.....	4
1.1.2 Photocatalytic behaviour of cobalt ferrite magnetic nanoparticles (CoFe <sub>2</sub> O <sub>4</sub> MNPs) .....	4
1.2 Phthalocyanines (Pcs) .....	5
1.2.1 Structure and synthetic methods.....	6
1.2.1.1 Synthesis of Symmetrical Tetrasubstituted Phthalocyanines.....	7
1.2.1.2 Synthesis of Unsymmetrical Phthalocyanines.....	8
1.2.2 Electronic Absorption Spectra of Pcs.....	9
1.2.3 Phthalocyanines synthesized in this thesis.....	10
1.2.4 Photocatalytic behaviour of Pcs.....	14
1.3 Electrospinning .....	18
1.3.1 Introduction to Electrospinning.....	18

1.3.2	Optimization of Electrospinning.....	19
1.3.3	Properties and Applications of electrospun fibers.....	20
1.4	Background on water pollutants used in this thesis.....	20
1.4.1	Azo dyes.....	21
1.4.2	Hexavalent Chromium (Cr(VI)).....	21
1.5	Photophysical Parameters.....	22
1.5.1	Fluorescence Quantum yields ( $\Phi_F$ ) and fluorescence lifetimes ( $\tau_F$ ).....	23
1.5.2	Triplet Quantum yields ( $\Phi_T$ ) and triplet lifetimes ( $\tau_T$ ).....	24
1.5.3	Singlet Oxygen Quantum yields ( $\Phi_\Delta$ ).....	25
1.6	Aims of thesis.....	27
<b>Chapter 2</b>		<b>28</b>
<b>2. Experimental.....</b>		<b>29</b>
2.1	Materials.....	29
2.1.1	Solvents.....	29
2.1.2	Reagents for synthesis of phthalocyanines.....	29
2.1.3	Reagents for synthesis and functionalisation of $\text{CoFe}_2\text{O}_4$ MNPs.....	29
2.1.4	Polymers for Electrospinning.....	30
2.1.5	Standards and Quenchers for determination of Photophysical Parameters.....	30
2.1.6	Reagents for Photocatalysis.....	30
2.2	Instrumentation.....	31
2.3	Phthalocyanine synthesis .....	37

2.3.1 2-[dimethyl 5-(phenoxy)-isophthalate] 9(10), 16(17) 23(24)-tri- <i>tert</i> -butyl phthalocyaninato zinc (II) (5) (Scheme 3.1).....	37
2.3.2. 2-[5-(phenoxy)-isophthalic acid] 9(10), 16(17), 23(24)-tri- <i>tert</i> -butyl phthalocyaninato zinc (II) (6) (Scheme 3.1).....	38
2.4 Synthesis and functionalisation of CoFe <sub>2</sub> O <sub>4</sub> MNPs.....	39
2.4.1 Oleic acid coated CoFe <sub>2</sub> O <sub>4</sub> MNPs (Scheme 3.2).....	39
2.4.2 Silica coated magnetic nanoparticles (CoFe <sub>2</sub> O <sub>4</sub> -SiO <sub>2</sub> MNPs, Scheme 3.2).....	39
2.4.3 Amine functionalised CoFe <sub>2</sub> O <sub>4</sub> magnetic nanoparticles (CoFe <sub>2</sub> O <sub>4</sub> -NH <sub>2</sub> MNPs, Scheme 3.2).....	40
2.4.4 Carboxylic acid functionalised magnetic nanoparticles (CoFe <sub>2</sub> O <sub>4</sub> -COOH MNPs, Scheme 3.2).....	40
2.4.5 Synthesis of glutathione functionalised CoFe <sub>2</sub> O <sub>4</sub> magnetic nanoparticles (CoFe <sub>2</sub> O <sub>4</sub> -GSH MNPs, Scheme 3.3).....	40
2.5 Conjugation of Pc complexes to CoFe <sub>2</sub> O <sub>4</sub> MNPs.....	41
2.5.1 Conjugation of complexes 1, 4 and 6 to CoFe <sub>2</sub> O <sub>4</sub> -NH <sub>2</sub> MNPs (Scheme 3.4).....	41
2.5.2 Conjugation of complex 2 to CoFe <sub>2</sub> O <sub>4</sub> -COOH MNPs (Scheme 3.5) .	42
2.5.3 Conjugation of complexes 2 and 7 to CoFe <sub>2</sub> O <sub>4</sub> -GSH MNPs (Scheme 3.6).....	42
2.6 Preparation of functionalised electrospun fibers .....	43
2.6.1 Preparation of functionalised polystyrene (PS) fibers.....	43

2.6.1 Preparation of functionalised polyamide-6 (PA-6) fibers.....	44
2.7 Photocatalysis .....	45
2.8 Photophysical and photochemical methods.....	45
2.7.1 Fluorescence Quantum Yields ( $\Phi_F$ ) and Lifetimes ( $\tau_F$ ).....	45
2.7.2 Triplet Quantum Yields ( $\Phi_T$ ) and Lifetimes ( $\tau_T$ ).....	46
2.7.3 Singlet Oxygen Quantum Yields ( $\Phi_\Delta$ ).....	46
<b>Results and Discussion.....</b>	<b>48</b>
<b>Publications.....</b>	<b>49</b>
<b>Chapter 3</b>	<b>50</b>
<b>3. Synthesis and Characterisation .....</b>	<b>51</b>
3.1 Phthalocyanines (Pcs).....	51
3.1.1 Synthesis.....	51
3.1.2 UV-vis spectroscopy.....	54
3.2 Synthesis and Characterisation of CoFe <sub>2</sub> O <sub>4</sub> MNPs and their respective Pc-CoFe <sub>2</sub> O <sub>4</sub> conjugates.....	57
3.2.1 Synthesis.....	57
3.2.2 Energy Dispersive X-ray Spectroscopy (EDS).....	66
3.2.3 Transmission Electron Microscopy (TEM).....	67
3.2.4 Dynamic Light Scattering (DLS).....	68
3.2.5 X-ray Diffraction (XRD).....	69



3.2.6 X-ray Photoelectron Spectroscopy (XPS).....	71
3.2.7 Thermal Analyses.....	76
3.8.8 UV-vis spectroscopy .....	77
3.4 Closing Remarks.....	79
<b>Chapter 4</b>	<b>80</b>
<b>4. Photophysical properties of phthalocyanines and Pc-MNP conjugates.....</b>	<b>81</b>
4.1 Fluorescence Quantum Yields ( $\Phi_F$ ) and Lifetimes ( $\tau_F$ ).....	81
4.2 Triplet Quantum Yields ( $\Phi_T$ ) and Lifetimes ( $\tau_T$ ).....	85
4.3 Singlet Oxygen Quantum Yields ( $\Phi_\Delta$ ).....	87
4.4 Closing Remarks.....	91
<b>Chapter 5</b>	<b>92</b>
<b>5. Electrospun polymer fibers.....</b>	<b>93</b>
5.1 Characterisation of functionalised electrospun fibers.....	93
5.1.1 Scanning Electron Microscopy.....	94
5.1.2 Surface area and Porosity analyses.....	96
5.1.3 Thermal Stability.....	97
5.1.4 UV-visible spectroscopy.....	99
5.2 Singlet oxygen generating ability of the functionalised fibers.....	100
5.3 Closing remarks.....	104

**6 Photocatalytic treatment of organic and inorganic pollutants... .....106**

6.1 Photooxidation of Orange G (OG).....	106
6.1.1 Application of Polystyrene (PS) fibers.....	106
6.1.1.1 UV-vis spectra.....	107
6.1.1.2 Kinetics studies .....	107
6.1.2 Application of Polyamide (PA-6) fibers .....	113
6.1.2.1 UV-vis spectra.....	114
6.1.2.2 Kinetics studies .....	114
6.2 Photooxidation of Methyl Orange (MO) with PA-6 fibers.....	117
6.2.1 UV-vis spectra.....	117
6.2.2 Kinetics studies.....	118
6.2.3 Reusability studies.....	121
6.3 Dual photooxidation of MO and photoreduction of Cr(VI).....	122
6.3.1 Photooxidation of Methyl Orange (MO).....	123
6.3.1.1 UV-vis spectra.....	123
6.3.1.2 Kinetics studies.....	124
6.3.2 Photoreduction of Hexavalent Chromium (Cr(VI)).....	127
6.3.2.1 UV-vis spectra.....	127
6.3.2.2 Kinetics studies.....	129
6.4 Mechanism of photocatalysis of Pc-CoFe <sub>2</sub> O <sub>4</sub> MNP conjugates.....	132
6.3 Closing Remarks.....	134

<b>Chapter 7</b>	<b>135</b>
<b>7. Conclusions and future plans.....</b>	<b>136</b>
7.1 Conclusions.....	136
7.2 Future Prospects.....	136
<b>References.....</b>	<b>138</b>

# List of Symbols

$K_A$	Adsorption coefficient
$\Phi_{ADMA}$	ADMA Quantum Yield
$\Phi_F$	Fluorescence Quantum Yield
$\Phi_T$	Triplet Quantum Yield
$\Phi_\Delta$	Singlet Oxygen Quantum Yield
$t_{1/2}$	Half-life
$k$	Apparent reaction rate constant
$r_o$	Initial photocatalytic degradation rate
$C_o$	Initial concentration of pollutant
$\tau_F$	Fluorescence Lifetime
$\tau_T$	Triplet Lifetime
$I_{abs}$	Light intensity
$n$	Refractive index of sample solvent
$n_{std}$	Refractive index of standard solvent

# List of Abbreviations

AA	Acetic acid
ADMA	Anthracene-9,10-bis-methylmalonate
AOP	Advanced Oxidative Process
APTES	(3-Aminopropyl)triethoxysilane
APTMS	(3-Aminopropyl)trimethoxysilane
BET	Brunauer–Emmett–Teller
DBU	1,8-Diazabicyclo[5.4.0]undec-7ene
DCC	Dicyclohexylcarbodiimide
DCM	Dichloromethane
DMSO	Dimethyl sulfoxide
DMF	N,N-Dimethylformamide
DPBF	1,3- Diphenylisobenzofuran
EDC	N,N'-dicyclohexylcarbodiimide
EDX	Energy Dispersive X-ray
FA	Formic acid
GSH	Glutathione
HPLC	High performance liquid chromatography
$^1\text{H}$ NMR	Proton Nuclear Magnetic resonance
HOMO	Highest Occupied Molecular Orbital
IC	Internal conversion
ISC	Intersystem crossing
LUMO	Lowest Unoccupied Molecular Orbital

MALDI-TOF	Matrix- Assisted Laser Desorption Ionization- Time of Flight
MPc	Metallophthalocyanine
MO	Methyl Orange
MNP	Magnetic Nanoparticles
OG	Orange G
PBS	Phosphate Buffer Solution
PA-6	Polyamide-6
Pc	Phthalocyanine
PS	Polystyrene
ROS	Reactive Oxygen Species
SEM	Scanning Electron Microscopy
TCD	Tip to Collector Distance
TCSPC	Time-Correlated Single Photon Counting
TEM	Transmission Electron Microscopy
TEOS	Tetraethoxysilane
TGA	Thermo-gravimetric Analysis
THF	Tetrahydrofuran
XRD	X-ray Diffraction
XPS	X-ray Photoelectron Spectroscopy

# CHAPTER 1

## Introduction

## 1. Introduction

The conjugation of nanoparticles with macrocycles such as phthalocyanines often yields a new class multi-functional composites with unique photophysicochemical properties and hence applications. Herein, various zinc-phthalocyanine derivatives are reported and so is their linkage to magnetic nanoparticles (MNPs) (bimetallic cobalt ferrite MNPs ( $\text{CoFe}_2\text{O}_4$  MNPs) to be precise) for enhanced photophysical and photochemical properties. The photocatalytic abilities of the composites are evaluated and their incorporation into electrospun fibers is also studied and reported herein.

### 1.1 Ferrites: Properties and Applications

Spinel ferrites, with a general formula of  $\text{MFe}_2\text{O}_4$ , where M represents is a metal cation, are magnetic materials, making them attractive for applications in magnetic resonance imaging (MRI), electronic devices, and drug delivery [1-3]. Their spinel crystal structures offer enhanced efficiency due to the available extra catalytic sites [4]. These MNPs are non-toxic and biocompatible, making them popular in the removal of heavy metals, as chemical sensors and as pigments amongst others [5-7].

Ferrites are also a class of popular photocatalysts, they have band gaps of approximately 2 eV which enable them to absorb visible light and they possess chemical and thermal stability [4, 8]. As demonstrated in **Figure 1.1**, when ferrites are irradiated with light, an electron ( $e^-$ ) is excited from the valence band (VB) to the conduction band (CB), leaving behind a photogenerated hole ( $h^+$ ). The generated  $e^-$  and  $h^+$  facilitate oxidation and reduction processes which are prerequisites for the degradation of water pollutants. The photocatalytic oxidation of organic compounds in water has been shown to be achieved by attack with hydroxyl radicals ( $\cdot\text{OH}$ ). The process of generating these  $\cdot\text{OH}$  can occur through two



pathways, denoted Route 1 and Route 2 in **Figure 1.1**. In the first pathway (Route 1),  $O_2$  present in water is reduced to form  $O_2^{\cdot-}$ , which then reacts with  $H^+$  to form  $\cdot OOH$ . Rapid decomposition of  $\cdot OOH$  forming  $\cdot OH$  then follows. The second pathway (Route 2) involves the oxidation of hydroxide ions ( $OH^-$ ) from water forming  $\cdot OH$  which have the ability to completely oxidise organic pollutants [9].

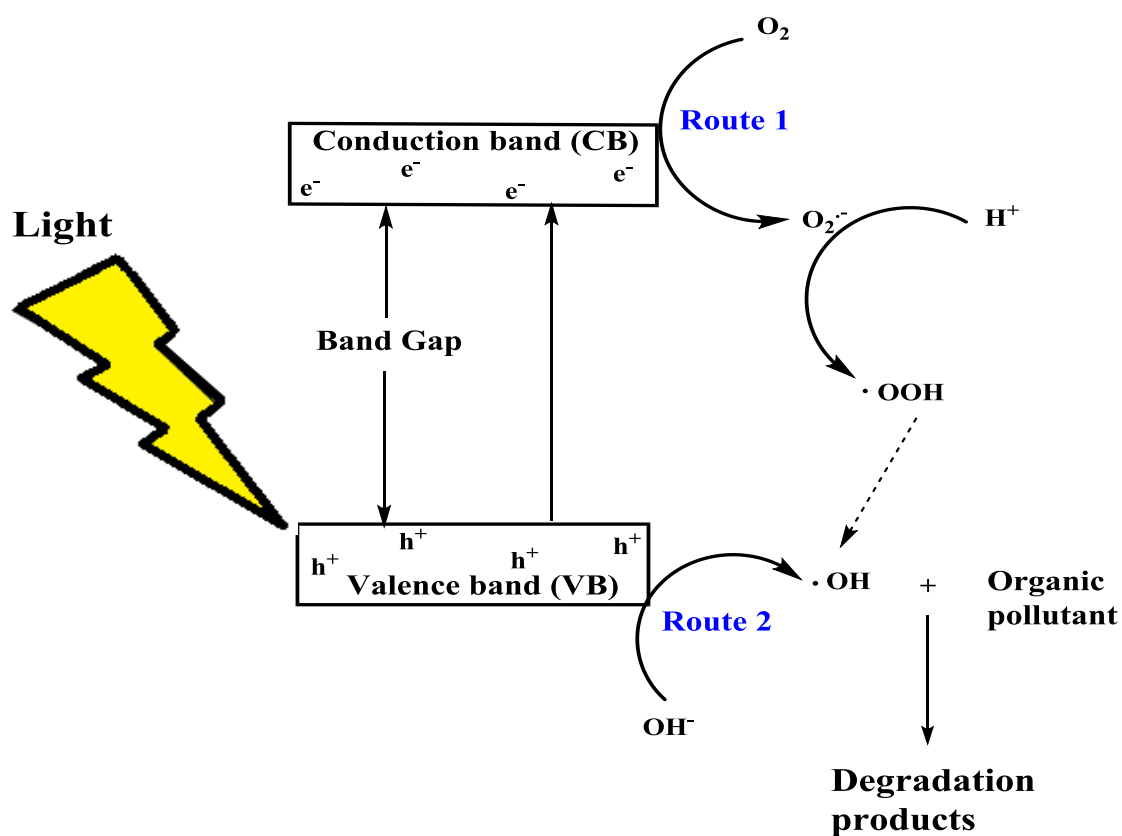


**Figure 1.1:** Modified schematic representation of the formation of hydroxyl radicals ( $\cdot OH$ ) which promote photocatalysis by ferrites [9].

Even though ferrites have been reported to have photocatalytic activity, the addition of oxidants such as  $H_2O_2$  is often required to enhance their reactive oxygen species (ROS) production and hence photocatalytic ability. This is because the  $e^-/h^+$  pairs tend to recombine quickly, thereby reducing the photocatalytic efficiency of the ferrites [9,10]. The conjugation

of ferrites to other photocatalysts including  $\text{TiO}_2$  has also been reported to remedy this [11,12]. In this work however,  $\text{CoFe}_2\text{O}_4$  MNPs are conjugated to other known photocatalysts; phthalocyanines for the first time for enhanced photocatalytic efficiency.

### **1.1.1 Synthesis and Characterisation of ferrites**

Numerous methods have been explored for the synthesis of ferrites, including co-precipitation, thermal, sol-gel and citrate methods, as well as solid-state reactions amongst others, all of which use Fe(III) and M(II) (M = metal cation) salts as precursors [13-16]. In this work the synthesis of ferrites ( $\text{CoFe}_2\text{O}_4$  MNPs) is conducted through the co-precipitation method wherein the nanoparticles are precipitated from aqueous solution with basic pH in which Fe(III) and Co(II) are dispersed [17].

The advantage of using these MNPs is that they can be functionalised with different moieties making their conjugation to other photocatalysts like phthalocyanines possible. In this work the  $\text{CoFe}_2\text{O}_4$  MNPs are functionalised with glutathione (-COOH terminal group), succinic anhydride (-COOH terminal groups) and (3-aminopropyl)triethoxysilane (- $\text{NH}_2$  terminal groups).

### **1.1.2 Photocatalytic behaviour of cobalt ferrite magnetic nanoparticles ( $\text{CoFe}_2\text{O}_4$ MNPs)**

As shown in **Table 1.1** [18-23], the photocatalytic activity of  $\text{CoFe}_2\text{O}_4$  MNPs and their respective composites has been exploited in numerous applications. Although  $\text{Fe}_3\text{O}_4$  MNPs have been conjugated to phthalocyanines before, there are no reports on the conjugation of bimetallic MNPs with phthalocyanines. This is explored in this work as it has been reported that mixed metal MNPs show more catalytic activity compared to the corresponding single component metal oxides [24].

**Table 1.1:** Examples of cobalt ferrite magnetic nanoparticle based composites as photocatalysts.

<b>CoFe<sub>2</sub>O<sub>4</sub> based catalyst</b>	<b>Application</b>	<b>Ref</b>
CoFe <sub>2</sub> O <sub>4</sub> -Fe <sub>3</sub> O <sub>4</sub> nanocomposite	Degradation of Methyl Orange	<b>18</b>
CoFe <sub>2</sub> O <sub>4</sub> @SiO <sub>2</sub> @TiO <sub>2</sub>	Degradation of Methylene Blue	<b>19</b>
CoFe <sub>2</sub> O <sub>4</sub> -Graphene nanocomposite	Degradation of Methylene Blue	<b>20</b>
CoFe <sub>2</sub> O <sub>4</sub> /oleic acid and Fe <sub>3</sub> O <sub>4</sub> /oleic acid	Antimicrobial and antifungal activity	<b>21</b>
Ag-CoFe <sub>2</sub> O <sub>4</sub> -GO nanocomposite	Antibacterial and Pb (II) removal	<b>22</b>
CoFe <sub>2</sub> O <sub>4</sub>	Water splitting	<b>23</b>

**GO = Graphene oxide**

The added advantage of these Pc-MNP conjugates is the magnetic regeneration and hence reusability of these generated photocatalysts. When ferrites are used alone as photocatalysts or in combination with others, they can be easily separated from reaction mixtures [25,26].

## 1.2 Phthalocyanines (Pcs)

Phthalocyanines (Pcs) are synthetic tetrapyrrolic macrocycles containing four iminoisoindoline rings with a conjugated 18  $\pi$ -electron system [27,28]. They are structural analogues of other macrocyclic pigments such as porphyrins and were first characterized and documented by Linstead and co-workers [29]. The central cavity of Pcs can accommodate numerous metals or metalloids thereby offering the advantage of designing a wide range of chemical structures having different properties and hence applications [30].

Pcs have attractive properties such as excellent visible/near infrared absorption, high chemical and thermal stability and the ability of generate singlet oxygen [31-33]. These

properties make Pcs good candidates for numerous applications including in electrochemical sensors, photodynamic therapy, dye sensitised solar cells (DSSC), and photocatalysis [34-37].

### 1.2.1 Structure and synthetic methods

The Pc ring can be easily modified allowing for attachment of substituents either on the  $\alpha$ -position (non-peripheral) or  $\beta$ -position (peripheral). According to nomenclature of tetrapyrroles [38],  $\alpha$ -substituents are positioned at the 1, 4, 8, 11, 15, 18, 22, and 25 positions on the Pc ring, while  $\beta$ -substituents are located at the 2, 3, 9, 10, 16, 17, 23, and 24 positions on the Pc ring; **Figure 1.2**. The attachment of different types of substituents at these positions affects some properties of Pcs including solubility and aggregation [39,40].

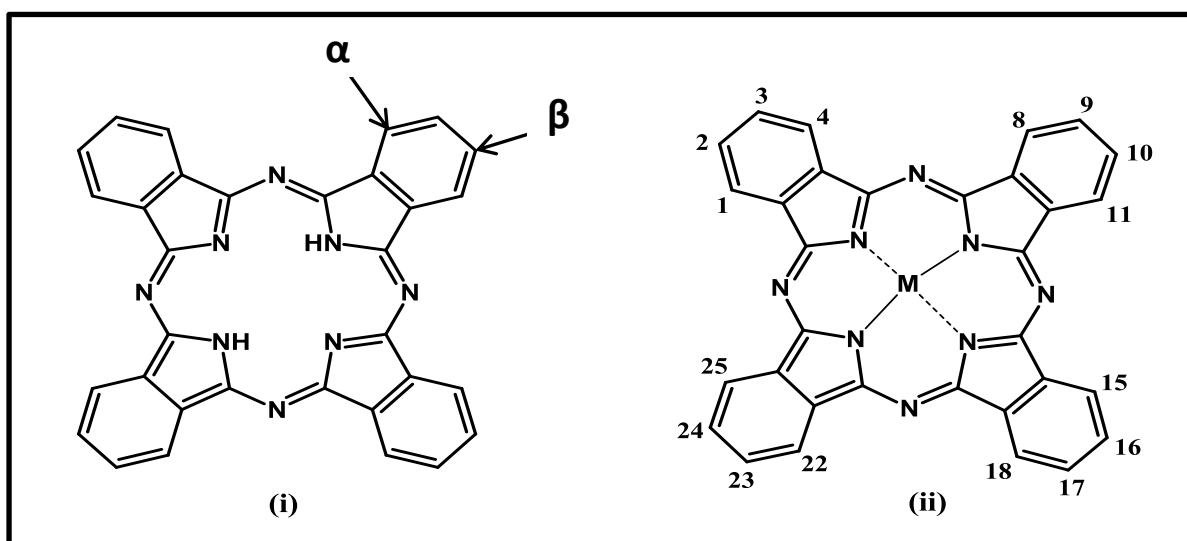


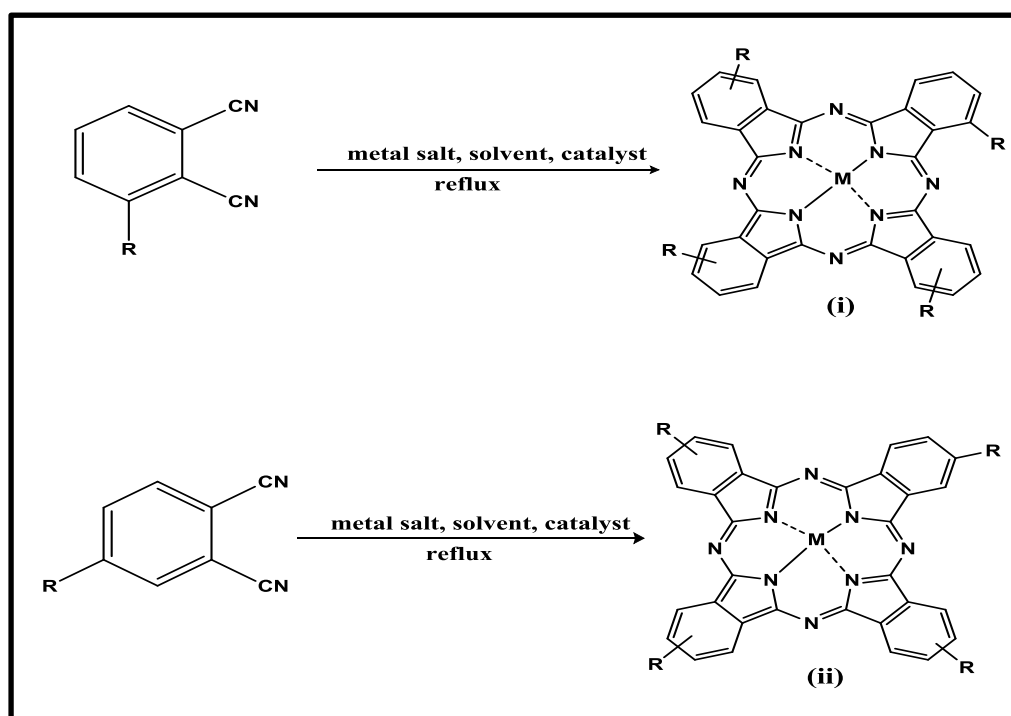
**Figure 1.2:** The structures of (i) an unmetallated phthalocyanine (H<sub>2</sub>Pc) and (ii) a metallophthalocyanine (MPc).

Various routes have been reported for the synthesis of Pcs, all of which depend on the type of the desired Pc, whether metallated or metal free (**Figure 1.2**), symmetrical or unsymmetrical.

### 1.2.1.1 Synthesis of Symmetrical Tetrasubstituted Phthalocyanines

Synthesis of symmetrical Pcs can be achieved by cyclotetramerization of phthalonitrile precursors in the presence of a metal salt (in the case of metallophthalocyanines), a base such as 1,8-diazabicycloundec-7ene (DBU) or dimethylaminoethanol (DMAE) and a high boiling point solvent such as quinoline and 1-pentanol [28,41].

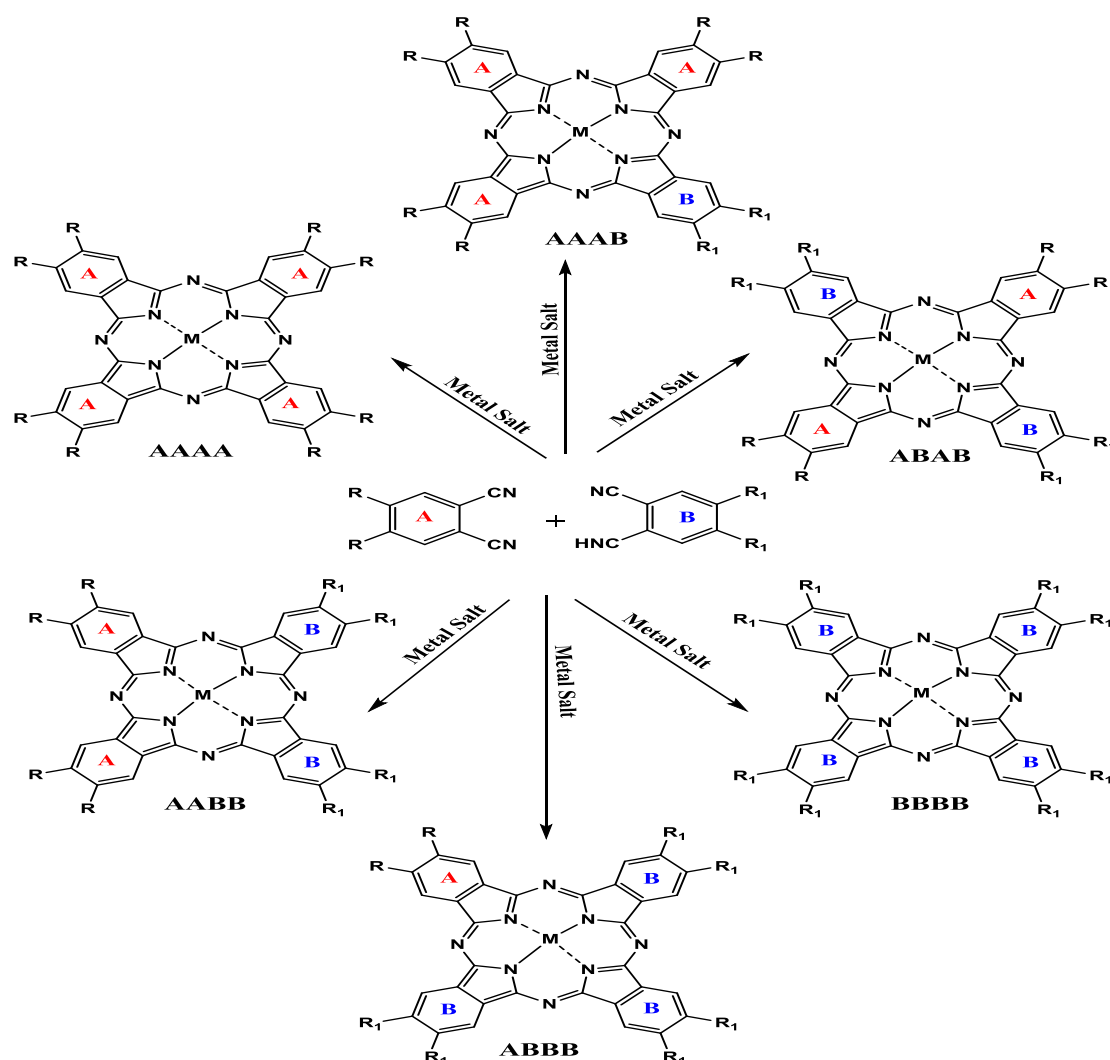
The cyclotetramerization of a mono-substituted phthalonitrile; **Scheme 1.1**, gives a mixture of isomers with the molecular symmetry of  $C_{4h}$ ,  $C_{2v}$ ,  $C_s$  and  $D_{2h}$ . Although time consuming, these isomers have been reported to be separable, even more so with the use of a specifically designed high performance liquid chromatographic column [42,43].



**Scheme 1.1:** Synthesis of tetrasubstituted metallophthalocyanines from monosubstituted phthalonitriles at (i) non-peripheral ( $\alpha$ ) and (ii) peripheral ( $\beta$ ) positions.

### 1.2.1.2 Synthesis of Unsymmetrical Phthalocyanines

Various methods have been reported for the synthesis of unsymmetrically substituted Pcs including the use of sub-phthalocyanine routes [44,45] and the conventional statistical mixed condensations of dinitriles [46,47]. The statistical condensation approach was implemented for the synthesis of AAAB or ABBB unsymmetrical Pcs in this work. This method requires two differently substituted phthalonitriles which upon cyclising in the presence of a metal salt give six possible constitutional isomers with varying percentage yields, **Scheme 1.2** [48]. The desired AAAB or ABBB Pcs are then separated using chromatography.



**Scheme 1.2:** Methods for the synthesis of unsymmetrical phthalocyanines by the statistical condensation method [48]

## 1.2.2 Electronic Absorption Spectra of Pcs

Phthalocyanines have distinct absorption spectra which are influenced by numerous factors including the presence or absence of a central metal ion, the nature of the substituents, solvents and aggregation tendencies. Phthalocyanines consist of two major absorption bands, the Q band in the near infrared region and a weaker absorption band towards the ultraviolet region of the spectrum called the B band [49,50]. Metallated Pcs have a single Q band while metal free Pcs ( $H_2Pc$ ) have a split Q band due to the low symmetry associated with them, **Figure 1.3** [30]. The Q band is accompanied by one or two weak vibronic bands ( $Q_{vib}$ ) and the B band consists of  $B_1$  and  $B_2$  bands.

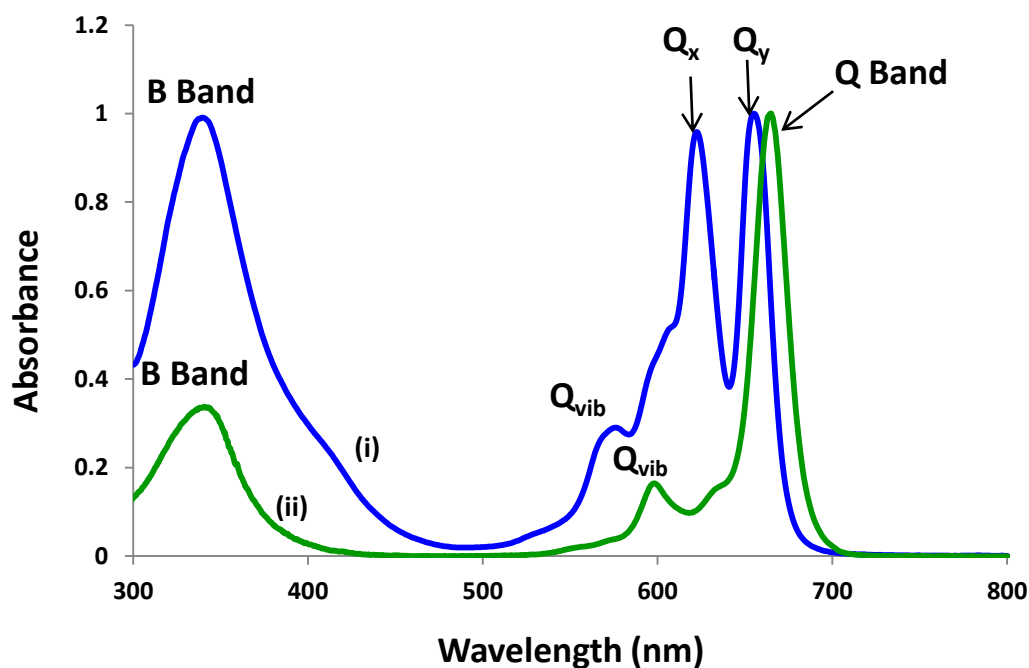


**Figure 1.3:** Electronic absorption spectra of: (i)  $H_2Pc$  and (ii)  $MPc$ .

Gouterman's four orbital model explains the origin of the  $B_1$  and  $B_2$  bands as transitions from the  $a_{2u}$  and  $b_{2u}$  to the  $e_g$  orbitals respectively, **Figure 1.4**. For  $MPc$ s the degeneracy in the lowest unoccupied molecular orbitals (LUMOs) is maintained due to their  $D_{4h}$  symmetry while in  $H_2Pc$ s, the degeneracy is broken down due to their low symmetry ( $D_{2h}$ ), **Figure 1.4**.

In MPcs, the Q band is therefore a result of the excitation from the ground state  $a_{1u}$  highest occupied molecular orbital (HOMO) to the  $e_g$  LUMO, **Figure 1.4** [51-53]. The observed split in the Q band for  $H_2Pc$  (denoted  $Q_x$  and  $Q_y$  on **Figure 1.4**) on the other hand arises from transitions from the  $a_{1u}$  HOMO to the  $b_{2g}$  and  $b_{3g}$  LUMO respectively [54].

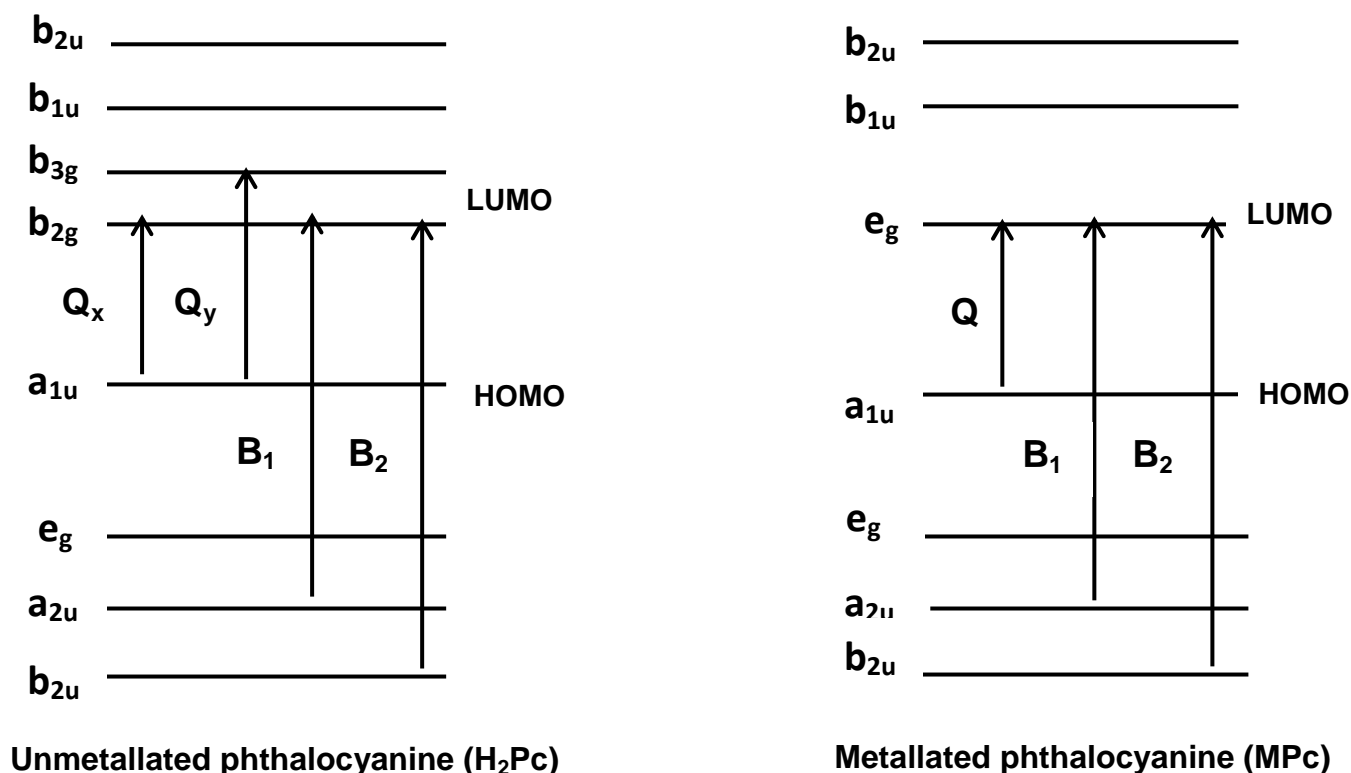


**Figure 1.4:** Electronic energy levels in Pc complexes showing the origin of the Q and B bands

### 1.2.3 Phthalocyanines synthesized in this thesis

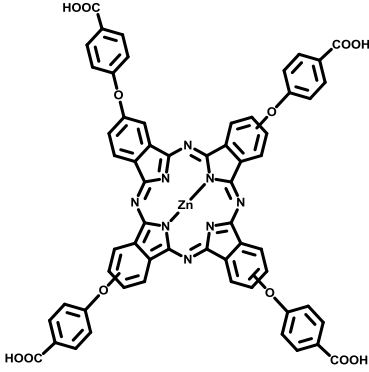
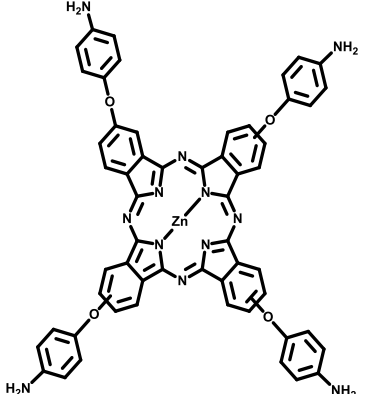
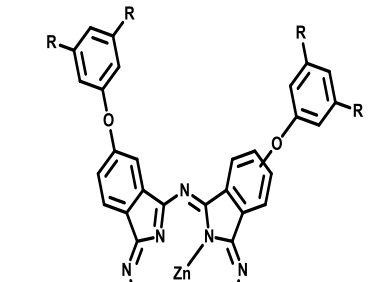

The Pcs used in this work are shown in **Table 1.2** and they were all chosen based on them having substituents that would complement those on the  $CoFe_2O_4$  MNPs and hence enable the formation of amide bonds between the two photocatalysts. Since  $CoFe_2O_4$  MNPs with amine and carboxylic acid functionalization were synthesised, Pcs with carboxylic acid and amine functionalization respectively were also synthesised. The effect of the spacer or chain

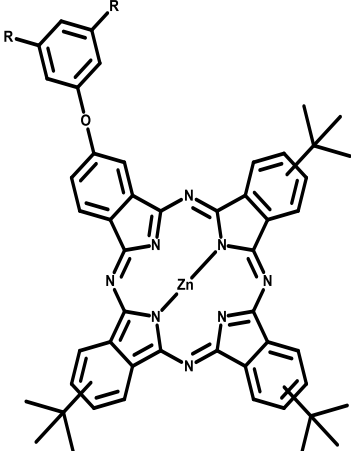
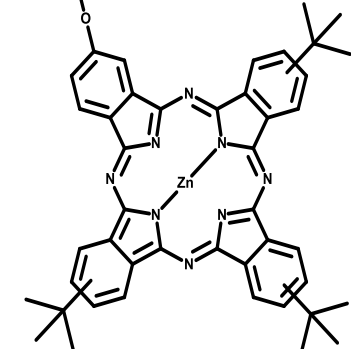
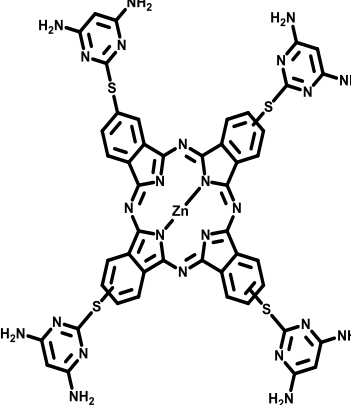


length between the Pcs and their respective MNPs on their photophysics and hence photocatalysis was studied for the first time in this work.

The photophysical and photochemical properties of Pcs are also influenced by the presence and nature of the central metal ion. Zinc Pcs have been reported to have high triplet and singlet oxygen quantum yields and are thus good photocatalysts [55-57]; hence all the Pcs used in this work have a  $Zn^{2+}$  central metal ion, **Table 1.2**. Complexes **1-4** and **7** are known [58-63] while **5** and **6** are new, however it is the first time that any of these Pcs have been conjugated to bimetallic  $CoFe_2O_4$  MNPs and applied in the photodegradation of pollutants. It is also the first time that the photophysicochemical properties of complexes **3** and **4** have been reported. The conjugation of an unsymmetrical Pc to  $Fe_3O_4$  MNPs and the use of the conjugate for inactivation of bacteria has been reported [64]. In this work however, the conjugation of an unsymmetrical Pc (complex **6**) to  $CoFe_2O_4$  MNPs is explored for the first time and so is its application in the degradation of water pollutants.

**Table 1.2:** Phthalocyanine complexes used in this thesis.

Phthalocyanine	Name and Study conducted	Complex
	<p><b>Zinc tetracarboxyphenoxy phthalocyanine</b></p> <p>Study: Photophysics when the Pc is conjugated to amine functionalised <math>\text{CoFe}_2\text{O}_4</math> MNPs and its photooxidising ability on azo dyes when electrospun in fibers.</p>	<p><b>1</b></p> <p><b>[58]</b></p>
	<p><b>Zinc tetraaminophenoxy phthalocyanine</b></p> <p>Study: Photophysics when the Pc is conjugated to carboxylic acid functionalised <math>\text{CoFe}_2\text{O}_4</math> MNPs, photoreduction ability on <math>\text{Cr(VI)}</math> and photooxidising ability on azo dyes when electrospun in fibers.</p>	<p><b>2</b></p> <p><b>[59, 60]</b></p>
	<p><math>\text{R} = \text{COOCH}_3</math></p> <p><b>2,10,16,24-Tetrakis dimethyl 5-(phenoxy)-isophthalate phthalocyaninato] zinc (II)</b></p> <p>Study: Photophysicochemical properties</p>	<p><b>3</b></p> <p><b>[61]</b></p>
	<p><math>\text{R} = \text{COOH}</math></p> <p><b>2(3),9(10),16(17),23(24)-Tetra 5-(phenoxy)-isophthalic acid phthalocyaninato zinc (II)</b></p> <p>Study: Photophysics before and after conjugation to amine functionalised <math>\text{CoFe}_2\text{O}_4</math> MNPs and photooxidising ability on azo dyes when electrospun in fibers.</p>	<p><b>4</b></p> <p><b>[62]</b></p>

	<p>R = COOCH<sub>3</sub></p> <p><b>2-[dimethyl 5-(phenoxy)-isophthalate] 9(10), 16(17)</b></p> <p><b>23(24)-tri-<i>tert</i>-butyl phthalocyaninato zinc (II)</b></p> <p>Study: Photophysicochemical properties</p>	<p><b>5</b></p> <p><b>NEW</b></p>
	<p>R = COOH</p> <p><b>2-[5-(phenoxy)-isophthalic acid] 9(10), 16(17), 23(24)-tri-<i>tert</i>-butyl phthalocyaninato zinc (II)</b></p> <p>Study: Photophysics before and after conjugation to amine functionalised CoFe<sub>2</sub>O<sub>4</sub> MNPs and photooxidising ability on azo dyes when electrospun in fibers.</p>	<p><b>6</b></p> <p><b>NEW</b></p>
	<p><b>2(3),9(10),16(17),23(24)-Tetrakis-(4'-(4'-6'-diaminopyrimidin-2'-ylthio))) phthalocyaninato zinc (II)</b></p> <p>Study: Photophysics when the Pc is conjugated to carboxylic acid functionalised CoFe<sub>2</sub>O<sub>4</sub> MNPs and photocatalysis on Methyl Orange and Cr(VI).</p>	<p><b>7</b></p> <p><b>[63]</b></p>

#### 1.2.4 Photocatalytic behaviour of Pcs

Photocatalysis entails the degradation of molecules using light in the presence of a photosensitiser. Phthalocyanines have been reported as efficient photosensitisers as they absorb visible/ near infrared light and have the ability to produce reactive oxygen species (ROS) which readily degrade pollutants [65,66].

Various photoinduced processes need to occur in order for the Pcs to exhibit photocatalytic activity towards pollutants and these are shown in **Figure 1.5**. When a Pc absorbs light of appropriate wavelength, it is excited from the ground state ( $S_0$ ) to the first singlet excited state ( $S_1$ ). The excited Pc can then dissipate energy either by fluorescence back to the ground state ( $S_0$ ) or by intersystem crossing (ISC) to the excited triplet state ( $T_1$ ) [67]. The triplet state ( $T_1$ ) has a longer lifetime ( $\mu\text{s}$ ) than that of the excited singlet state ( $S_1$ ) (ns), enabling the Pc in the triplet excited state to react with molecular oxygen in two different ways; Type I and Type II shown in **Figure 1.5** [68].

In the Type I mechanism (**Figure 1.5**), the Pc in the excited triplet state ( $^3\text{Pc}^*$ ) transfers an electron to molecular oxygen ( $^3\text{O}_2$ ) generating cytotoxic radicals and ROS including hydroxyl radicals ( $^{\bullet}\text{OH}$ ), peroxides ( $\text{H}_2\text{O}_2$ ) and hydroxide ions ( $\text{OH}^-$ ) [68]. It is these ROS which have the ability to readily degrade organic pollutants.

In the Type II mechanism; **Figure 1.5**, the Pc in triplet excited state ( $^3\text{Pc}^*$ ) transfers energy to molecular oxygen ( $^3\text{O}_2$ ) thereby generating singlet oxygen ( $^1\text{O}_2$ ) [68]. The singlet oxygen then reacts with the organic pollutants to yield the degradation products.

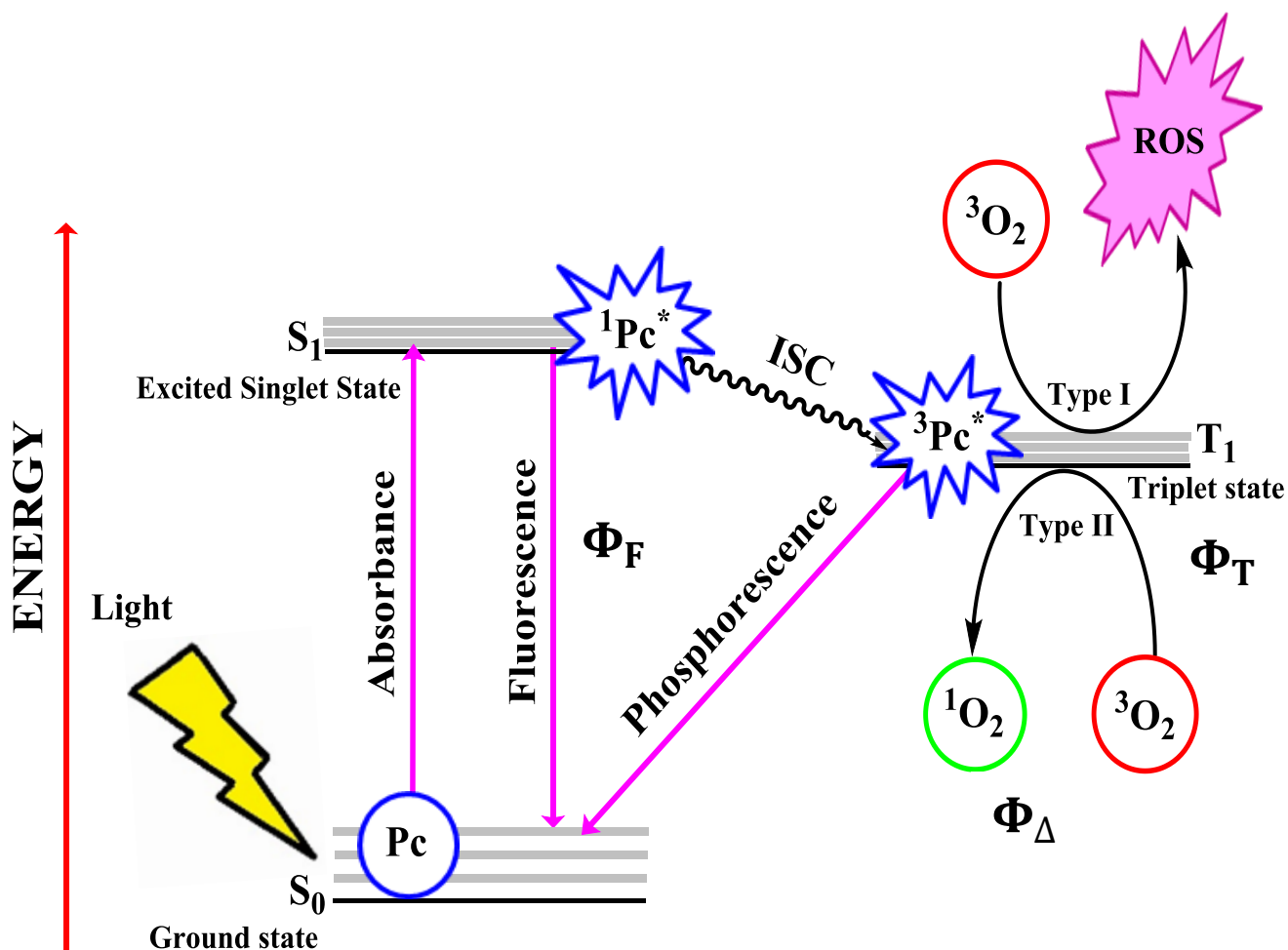


**Figure 1.5:** Modified Jablonski diagram showing the major photophysical processes that occur in Pcs.

Since it is the singlet oxygen amongst other species that is responsible for the photocatalytic ability of Pcs, the enhancement of its production is conducted in this work for improved photocatalysis. It has been reported that the conjugation of Pcs to nanoparticles including MNPs enhances the photophysics and hence photocatalytic ability of the Pcs. This is due to the heavy atom effect that the nanoparticles possess which enhances ISC, results in enhanced singlet oxygen production and hence photocatalytic activity [69,70]. In this work, the conjugation of Pcs to  $CoFe_2O_4$  MNPs is explored for the first time for enhanced singlet oxygen production and hence photocatalysis.

The photocatalytic activities of the Pc-CoFe<sub>2</sub>O<sub>4</sub> MNP conjugates reported herein are tested based on their ability to facilitate both photooxidation of organic pollutants and photoreduction of heavy metals, using azo dyes and hexavalent chromium as models respectively.

As shown in **Table 1.3 [69-79]**, the photooxidation of various organic pollutants has been achieved using Pc based photocatalysts before. However in this work the photooxidation of toxic organic pollutants is attempted for the first time using a composite of two photocatalysts; Pcs and CoFe<sub>2</sub>O<sub>4</sub> MNPs. **Table 1.3 [80-82]** also shows that the photoreduction of Cr(VI) using Pc based photocatalysts has also been reported before. In this work, the photoreduction ability of Pc-CoFe<sub>2</sub>O<sub>4</sub> MNP conjugates is tested for the first time wherein the electrons in the conduction band and LUMO of CoFe<sub>2</sub>O<sub>4</sub> MNPs and Pcs respectively are utilised to facilitate the photoreduction of hexavalent chromium. The simultaneous photooxidation and photoreduction ability of these conjugates is also explored in this work for the first time.

**Table 1.3:** Photocatalytic activity of phthalocyanine based photocatalysts

<b>Photocatalyst</b>	<b>Support</b>	<b>Pollutants</b>	<b>Ref</b>
Zinc tetracarboxyphenoxy phthalocyanine	Gd <sub>2</sub> O <sub>3</sub> /Polyamide-6	Orange G	<b>69</b>
ZnOCPc	Fe <sub>3</sub> O <sub>4</sub>	Orange G	<b>70</b>
Iron tetrasulfophthalocyanine	-	Rhodamine B (RhB), Salicylic acid, and Orange II	<b>71</b>
Zinc tetracarboxyphenoxy phthalocyanine	Gd <sub>2</sub> O <sub>3</sub>	Orange G	<b>72</b>
Iron (III) tetracarboxyphthalocyanine	TiO <sub>2</sub>	methylene blue, neutral red, rhodamine B, acid red, malachite green	<b>73</b>
Zinc phthalocyanine complexes	-	4-nitrophenol	<b>74</b>
Zinc(II) and Aluminium (III) mono- and polynuclear phthalocyanines	-	Phenols	<b>75</b>
ZnOCPc	Fe <sub>3</sub> O <sub>4</sub> / Electrospun Polyamide-6	Orange G	<b>76</b>
Lutetium tetraphenoxy phthalocyanine	Electrospun Polystyrene	4-Chlorophenol	<b>77</b>
TCbZnPc–ZnOMPs and TCbZnPc–AgNPs	Electrospun Polystyrene	Rhodamine-6G	<b>78</b>
Lutetium acetate tetra-2-pyridiloxy phthalocyanine	Electrospun Polystyrene	4-nitrophenol	<b>79</b>
HATCPc	TiO <sub>2</sub>	Cr(VI)	<b>80</b>

Copper(II) phthalocyanine	TiO <sub>2</sub>	Cr(VI)	<b>81</b>
H <sub>2</sub> phthalocyanines	TiO <sub>2</sub>	Cr(VI)	<b>82</b>

**ZnOCPC = Zinc octacarboxy phthalocyanine, TCbZnPc-ZnOMPs = 2,(3)-tetra(carbazol-2-yloxy)phthalocyaninato zinc(II)-Zinc Oxide Macro Particles, AgNPs = Silver Nanoparticles, HATCPC = Hydroxoaluminium-tricarboxymonoamide phthalocyanine, H<sub>2</sub> = metal free azomethine-bridged phenolic phthalocyanines**

## 1.3 Electrospinning

### 1.3.1 Introduction to Electrospinning

Phthalocyanines have been anchored in various support systems during photocatalysis including on amberlite [83], TiO<sub>2</sub> [84], polydivinylbenzene [85] and silica [86] amongst others. In this work the use electrospun fibers to anchor Pcs, CoFe<sub>2</sub>O<sub>4</sub> MNPs and their respective conjugates is explored. The electrospinning technique was developed in 1934 by Forhals [87]. This is a technique that generates fibers with diameters in the micro and nanometer scale with a general setup as shown in **Figure 1.6**.

The basic electrospinning components include a high voltage source, a ground/rotating collector (which is an electrical conductor) and a spinneret. Basically, a high voltage is applied to a polymer fluid which is fed through the spinneret with the help of the syringe pump. The discharged polymer solution undergoes a whipping wherein the solvent evaporates and the stretched polymer fibers deposit on the collector [88, 89].



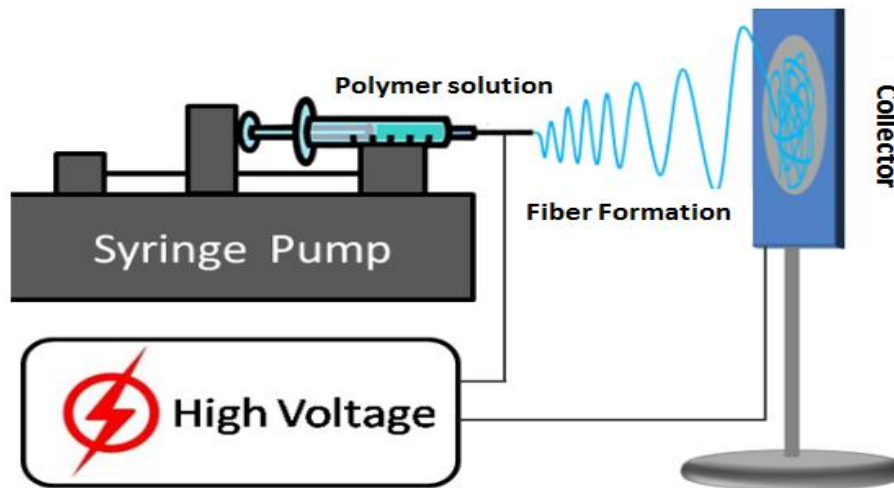


**Figure 1.6:** Schematic diagram of electrospinning setup [88].

### 1.3.2 Optimization of Electrospinning

Nanofibers with different morphologies and diameters can be obtained by varying certain parameters including:

- intrinsic properties of the polymer solution such as the type of polymer, solution viscosity, and solvent volatility
- processing parameters including the strength of the applied electric field, solution flow rate, and tip to collector distance (TCD) [90-92].

In addition, variables such as humidity and temperature of the surroundings may also determine the morphology and diameter of electrospun fibers [88].

Experimental investigations have drawn general relationships between these parameters and fiber morphology. For instance, a higher voltage has been observed to lead to larger fiber diameters, a trend that is not necessarily monotonic. It has also been observed that the more viscous the polymer solution, the larger the fiber diameter [88].

### **1.3.3 Properties and Applications of electrospun fibers**

Electrospinning is a promising technique for the incorporation of functional molecules such as Pcs into solid polymer supports. Electrospun fibers, due to their smaller pores, long length and higher surface areas are successfully used in various fields including tissue engineering scaffolds, protective clothing, filtration, and nanocatalysis amongst others [93-95].

As shown in **Table 1.3 [69,76-79]**, symmetrical Pc based photocatalysts have been embedded in electrospun fibers before and used in the photodegradation of various pollutants. In this work, Pc-CoFe<sub>2</sub>O<sub>4</sub> MNP conjugates are immobilised in electrospun polystyrene and polyamide-6 followed by application in the photodegradation of azo dyes; Orange G (OG) and Methyl Orange (MO) for the first time. In addition, this work studies the photocatalytic activity of an electrospun unsymmetrical Pc and its relative Pc-CoFe<sub>2</sub>O<sub>4</sub> MNP conjugate for the first time. This is done as asymmetry in Pcs is known to improve their triplet state parameters [96] and hence photocatalysis.

The advantage of incorporating the photocatalysts reported in this work in the electrospun fibers is that catalyst recovery is ensured by both the magnetic nature of the nanoparticles and by the use of the electrospun fibers. This ensures catalyst regeneration and hence reusability as well as cost effectiveness. In addition, embedding the photocatalysts in the fibers also ensures that they are protected from degradation and do not leach into the water, thereby further polluting it.

### **1.4 Background on water pollutants used in this thesis**

Since wastewaters contain various kinds of pollutants including organic and inorganic compounds amongst others, this work seeks to diminish the toxicity associated with such pollutants. The treatment of both organic and inorganic pollutants is studied, using azo dyes and hexavalent chromium as model compounds, respectively.

### **1.4.1 Azo dyes**

Azo dyes are synthetic dyes which are widely used in various fields including textile, tannery and cosmetic industries as well as paper printing amongst others [97-100]. They are water-soluble dyes possessing the characteristic azo (-N=N-) bond and are poorly biodegradable [100]. The azo bond determines the color of the dyes and is the most reactive moiety, usually undergoing oxidation leading to fading of the color of the dye solution upon degradation [101]. The complete degradation of azo dyes is however difficult due to their complex structures [102]. These dyes have also been reported to compromise aquatic life, they are carcinogenic and potential genotoxic agents, hence the importance of devising means for effectively degrading them [103-105].

Various techniques including filtration, coagulation, precipitation, adsorption and ion exchange have been reported for the removal of azo dyes [106-109]. These methods however merely change the dye from one phase to another and are not destructive, making treatment of azo dyes costly due to the required retreatment [110,111], hence alternative methods are required. Photocatalytic oxidation, an efficient advanced oxidative process (AOP) is reported here wherein the decomposition of azo dyes; MO and OG is conducted in a short reaction time.

### **1.4.2 Hexavalent Chromium (Cr(VI))**

Chromium commonly occurs in two oxidation states; Cr(III) and Cr(VI) [112]. Hexavalent chromium (Cr(VI)) is approximately 100 times more toxic than trivalent chromium (Cr(III)) and has been reported to be carcinogenic amongst other things [113,114]. Cr(III) is relatively nontoxic because it is not well absorbed into the body, and even when it is absorbed, it enters the cell poorly [115]. Cr(VI) on the other hand is extremely toxic, at physiological pH it exists as an oxyanion with an overall charge of -2 ( $\text{CrO}_4^{2-}$ ), structurally resembling phosphate

( $\text{PO}_4^{2-}$ ) and sulfate ( $\text{SO}_4^{2-}$ ) and is therefore efficiently transported into all cells in the place of these anions [116]. Intracellularly, the reduction of Cr(VI) to Cr(III) occurs which then ultimately interacts with the DNA, leading to neoplastic transformation of cells and ultimately causing cancer [117].

Not only is Cr(III) significantly less toxic, it is readily removable by alkaline precipitation [118]. Methods commonly used to treat wastewater containing Cr(VI) include adsorption [119] and ion exchange [120]. In this thesis, the focus is on the use of Pc-MNP conjugates as photocatalysts in the photoreduction of Cr(VI) to Cr (III). Removal of Cr(VI) by adsorption on  $\text{CoFe}_2\text{O}_4$  MNPs has been reported but only in the presence of other compounds such as Mg-Al layered double hydroxides (LDHs) [121]. The photocatalytic reduction of Cr(VI) to Cr (III) in the presence of  $\text{Fe}_2\text{O}_3$  MNPs has also been reported through the formation of  $e^-/h^+$  pairs of the latter [122].

It has been reported that the reduction of Cr(VI) to Cr(III) is accelerated in the presence of sacrificial donors such as 4-chlorophenol [80] which prevent the re-oxidation of Cr(III) to Cr(VI). In this work, in addition to studying the photodegradation of MO and OG, MO is also used as a sacrificial electron donor during the photoreduction of Cr(VI). In the presence of MO, the oxidation of Cr(III) to Cr(VI) is suppressed since MO acts as a sacrificial molecule and its photooxidation is promoted.

## 1.5 Photophysical Parameters

The major photophysical transitions that occur when Pcs are irradiated with light for photocatalytic applications; fluorescence, ISC to the excited triplet state as well as the quantity of singlet oxygen produced are all measurable and are denoted  $\Phi_F$ ,  $\Phi_T$ , and  $\Phi_\Delta$  in **Figure 1.5**.

### 1.5.1 Fluorescence Quantum Yields ( $\Phi_F$ ) and Fluorescence Lifetimes ( $\tau_F$ )

The fluorescence quantum yield ( $\Phi_F$ ) expresses the proportion of excited molecules that undergo relaxation back to the ground state by fluorescence [123].

Fluorescence quantum yield ( $\Phi_F$ ) may be determined by the comparative method [123] using

**Equation 1.1:**

$$\Phi_F = \Phi_{F(Std)} \frac{F A_{Std} n^2}{F_{Std} A n_{Std}^2} \quad 1.1$$

where  $F$  and  $F_{Std}$  are the areas under the fluorescence curve of the Pcs and standard respectively.  $A$  and  $A_{Std}$  are the absorbance values of the sample and standard at the excitation wavelength, while  $n$  and  $n_{Std}$  are the refractive indices of the solvents used for the preparation of the sample and standard solutions, respectively.  $\Phi_{F(Std)}$  is the fluorescence quantum yield of the standard in a particular solvent. The commonly used standard is unsubstituted zinc Pc (ZnPc).

Fluorescence lifetime on the other hand shows the average time an excited molecule stays in the excited state before losing all its energy by fluorescence. It is directly proportional to the fluorescence quantum yield and is usually in the order of nanosecond. Several methods have been reported for the determination of fluorescence lifetimes [124,125]. In this work however, time-correlated single photon counting (TCSPC) is used [126].

### 1.5.2 Triplet Quantum Yields( $\Phi_T$ ) and Triplet Lifetimes ( $\tau_T$ )

The triplet quantum yield ( $\Phi_T$ ) is the fraction of species that undergo radiationless decay from the excited singlet state to the triplet state [127]. Triplet lifetime is the amount of time it takes for the excited triplet state to be depopulated by either transferring energy to molecular oxygen or losing energy by phosphorescence. In this work, the triplet lifetimes were determined by exponential fitting of the kinetic curve using ORIGIN 8 Software.

The triplet quantum yields of the Pcs used in this work were determined using a comparative method [128] as shown in **Equation 1.2**; wherein unsubstituted zinc Pc (ZnPc) was used as a standard:

$$\Phi_T = \Phi_T^{Std} \frac{\Delta A_T \varepsilon_T^{Std}}{\Delta A_T^{Std} \varepsilon_T} \quad \mathbf{1.2}$$

where  $\Delta A_T$  and  $\Delta A_T^{Std}$  are the changes in the triplet state absorptions of the synthesized Pcs and standard, respectively.  $\Phi_T^{Std}$  is the triplet state quantum yield for the standard.  $\varepsilon_T$  and  $\varepsilon_T^{Std}$  are the triplet state extinction coefficients for the synthesized Pcs and the standard, respectively and are determined using **Equations 1.3** and **1.4** respectively:

$$\varepsilon_T = \varepsilon_S \frac{\Delta A_T}{\Delta A_S} \quad \mathbf{1.3}$$

$$\varepsilon_T^{Std} = \varepsilon_S^{Std} \frac{\Delta A_T^{Std}}{\Delta A_S^{Std}} \quad \mathbf{1.4}$$

where  $\varepsilon_S$  and  $\varepsilon_S^{Std}$  are ground state molar extinction coefficients of the samples and standard, respectively while  $\Delta A_S$  and  $\Delta A_S^{Std}$  are changes in the ground state absorptions of the synthesized Pcs and standard, respectively.

### 1.5.3 Singlet Oxygen Quantum Yields ( $\Phi_{\Delta}$ )

The singlet oxygen quantum yield ( $\Phi_{\Delta}$ ) can be defined as the amount of singlet oxygen that is obtained per photon of light that is absorbed by the Pcs. Singlet oxygen ( $^1\text{O}_2$ ), a metastable state of molecular oxygen ( $^3\text{O}_2$ ) is produced through energy transfer from the excited triplet state of the Pcs to molecular oxygen.

Experimentally, singlet oxygen quantum yields of Pcs can be quantified using optical or chemical methods. The optical method entails the time resolved phosphorescence decay of singlet oxygen at 1270 nm [129]. In this work the chemical method is used. This requires the use of singlet oxygen quenchers which react in a 1:1 ratio with singlet oxygen. Ideally the decomposition product of the quencher should not react with the generated singlet oxygen, interfere with the detection of singlet oxygen nor interfere with stability of the Pc.

In this work, 1,3- diphenylisobenzofuran (DPBF) and anthracene-9,10-bis-methylmalonate (ADMA) are used as singlet oxygen quenchers in organic and aqueous media, respectively. The experiment is usually carried out by irradiating a sample solution containing a Pc and quencher. The degradation of the quencher is then monitored spectroscopically [130,131] and the singlet oxygen is quantified using **Equation 1.5**:

$$\Phi_{\Delta} = \Phi_{\Delta}^{\text{Std}} \frac{R I_{\text{Abs}}^{\text{Std}}}{R^{\text{Std}} I_{\text{Abs}}} \quad \mathbf{1.5}$$

where  $\Phi_{\Delta}^{\text{std}}$  is the singlet oxygen quantum yield for the standard Pc (ZnPc). R and  $R^{\text{std}}$  are the rates of photodegradation of the singlet oxygen quencher by the samples and the standard, respectively.  $I_{\text{abs}}$  and  $I_{\text{abs}}^{\text{std}}$  are the rates of absorption of light by samples and standards, respectively and are defined by **Equations 1.6** and **1.7**:

$$I_{Abs} = \frac{\alpha \cdot A \cdot I}{N_A} \quad 1.6$$

$$I_{Abs}^{Std} = \frac{\alpha^{Std} \cdot A \cdot I}{N_A} \quad 1.7$$

where,  $\alpha = 1 - 10^{-A(\lambda)}$ ,  $A(\lambda)$  is the absorbance of the sensitizer at the irradiation wavelength,  $A$  is the irradiated area ( $2.5 \text{ cm}^2$ ),  $I$  is the intensity of light calculated using the wavelength of the Q band of the Pc (photons/ $\text{cm}^2 \text{ s}$ ) and  $N_A$  is the Avogadro's constant.

For the determination of  $\Phi_{\Delta}$  of Pcs (or conjugates) embedded in fibers, the direct chemical method was employed due to lack of standards. The studies were carried out in an aqueous solution, using ADMA as a chemical quencher for singlet oxygen where its degradation was spectroscopically monitored at 380 nm [132].

The quantum yield of ADMA ( $\Phi_{ADMA}$ ) was calculated using **Equation 1.8**:

$$(\Phi_{ADMA}) = \frac{(C_0 - C_t)V_R}{I_{Abs}t} \quad 1.8$$

where  $C_0$  and  $C_t$  are the ADMA concentrations prior to and after irradiation, respectively.  $V_R$  is the solution volume,  $t$  is the irradiation time per cycle and  $I_{abs}$  is defined in **Equation 1.6**.

The absorbances used for **Equation 1.8** are those of the phthalocyanines in the fibers (not in solution) measured by placing the modified fiber directly on a glass slide. The light intensity measured refers to the light reaching the spectrophotometer cells, and it is expected that some of the light may be scattered, hence the  $\Phi_{\Delta}$  values of the phthalocyanines in the fiber are estimates. The singlet oxygen quantum yields ( $\Phi_{\Delta}$ ) were calculated using **Equation 1.9**:



$$\frac{1}{\Phi_{ADMA}} = \frac{1}{\Phi_{\Delta}} + \frac{1}{\Phi_{\Delta}} \cdot \frac{k_d}{k_a} \cdot \frac{1}{[ADMA]} \quad 1.9$$

where  $k_d$  is the decay constant of singlet oxygen and  $k_a$  is the rate constant for the reaction of ADMA with  $^1O_2$  ( $^1\Delta_g$ ). The intercept obtained from the plot of  $1/\Phi_{ADMA}$  versus  $1/[ADMA]$  gives  $1/\Phi_{\Delta}$ .

## 1.6 Aims of thesis

This work seeks to devise means of treating organic and inorganic water pollutants using multifunctional nanocomposites derived from Pcs and ferrites.

The specific aims of the thesis include:

1. Synthesis and characterisation of carboxylic acid and amine functionalised zinc Pcs.
2. Synthesis and characterisation of carboxylic acid and amine functionalised  $CoFe_2O_4$  MNPs and their conjugation to the Pcs via amide bonds.
3. Evaluation of the photophysical properties of the Pcs and Pc-MNP conjugates.
4. Photocatalytic analyses of the Pc-MNP conjugates in the photooxidation of azo dyes and photoreduction of Cr(VI).
5. Fabrication of electrospun fibers functionalised with Pcs and Pc-MNP conjugates.
6. Characterisation of electrospun fibers and their application in the photooxidation of azo dyes.

# CHAPTER 2

## Experimental

## 2. Experimental

### 2.1 Materials

#### 2.1.1 Solvents

Toluene, dimethyl sulphoxide (DMSO), deuterated dimethyl sulphoxide (DMSO- $d_6$ ), deuterated chloroform (CDCl<sub>3</sub>), dichloromethane (DCM), N, N-dimethylformamide (DMF), tetrahydrofuran (THF), methanol, ethanol and hydrochloric acid (HCl) were purchased from SAARChem. Formic acid (FA) and acetic acid (AA) were purchased from Minema chemicals and 1-pentanol was purchased from Sigma-Aldrich.

#### 2.1.2 Reagents for synthesis of phthalocyanines

Zinc acetate dihydrate ((Zn(OAc)<sub>2</sub> · 2H<sub>2</sub>O) and 1,8-diazabicyclo[5.4.0]undec-7ene (DBU) were purchased from Sigma-Aldrich. Dimethyl 5-(3,4-dicyanophenoxy)-isophthalate (**8**) (**Scheme 3.1**) was synthesized according to literature procedures [**61,62**] and 4-*tert*-butylthalonitrile (**9**) (**Scheme 3.1**) was purchased from Wako Pure Chemical Industries. Zinc tetracarboxyphenoxy phthalocyanine (**1**) [**58**], zinc tetraaminophenoxy phthalocyanine (**2**) [**59,60**], 2,10,16,24-tetrakis dimethyl 5-(phenoxy)-isophthalate phthalocyaninato] zinc (II) (**3**) [**61**], 2(3),9(10),16(17),23(24)-Tetra 5-(phenoxy)-isophthalic acid phthalocyaninato] zinc (II) (**4**) [**62**] and 2(3),9(10),16(17),23(24)-tetrakis-(4'-(4'-6'-diaminopyrimidin-2'-ylthio))) phthalocyaninato zinc (II) (**7**) [**63**] were synthesised according to literature procedures.

#### 2.1.3 Reagents for synthesis and functionalisation of CoFe<sub>2</sub>O<sub>4</sub> MNPs

Cobalt (II) chloride was purchased from Fluka. Iron(III) chloride hexahydrate, oleic acid, tetraethoxysilane (TEOS), (3-aminopropyl)triethoxysilane (APTES), reduced glutathione,

succinic anhydride, (3-aminopropyl)trimethoxysilane (APTMS), dicyclohexylcarbodiimide (DCC) and *N,N'*-dicyclohexylcarbodiimide (EDC) and N-hydroxysuccinimide (NHS) were purchased from Sigma–Aldrich. Sodium hydroxide (NaOH) pellets were purchased from Minema chemicals.

#### **2.1.4 Polymers for Electrospinning**

Polystyrene (PS) ( $M_w = 192\,000$  g/mol) was purchased from Sigma-Aldrich and Polyamide-6 Ultramid® B32 grade ( $M_w = 90,000$  g/mol) was supplied by BASF.

#### **2.1.5 Standards and Quenchers for determination of Photophysical Parameters**

Anthracene-9,10-bis-methylmalonate (ADMA), unsubstituted zinc phthalocyanine (ZnPc) and 1,3- diphenylisobenzofuran (DPBF) were purchased from Sigma-Aldrich., AlPcSmix (a mixture of sulfonated aluminium Pcs) was synthesized according to literature [133].

#### **2.1.6 Reagents for Photocatalysis**

Chromium (VI) oxide, MO and OG were purchased from Sigma Aldrich. Phosphate buffer saline was prepared using appropriate quantities of sodium chloride (NaCl), potassium chloride (KCl) purchased from Minera as well as sodium hydrogen phosphate dihydrate ( $\text{Na}_2\text{HPO}_4 \cdot 2\text{H}_2\text{O}$ ) and potassium hydrogen phosphate ( $\text{KH}_2\text{PO}_4$ ) purchased from Riedel-de Haën. The salts were dissolved in ultra-pure water obtained from Milli-Q Water Systems (Millipore Corp, Bedford, MA, USA).

## 2.2 Instrumentation

1. UV–Vis absorption spectra were measured at room temperature on a Shimadzu UV-2550 spectrophotometer using a 1 cm pathlength cuvette in solution. A Perkin Elmer Lambda 950 UV-vis spectrophotometer was used for solid state spectra of the functionalised fibers.

2. Fluorescence emission and excitation spectra were obtained on a Varian Eclipse spectrofluorometer using a 1 cm pathlength quartz cuvette.

3. Fluorescence lifetimes were measured using a time correlated single photon counting (TCSPC) setup (FluoTime 300, Picoquant GmbH), **Figure 2.1**. The excitation source was a diode laser (LDH-P-670 driven by PDL 800-B, 670 nm, 20 MHz repetition rate, 44 ps pulse width, Pico quant GmbH). Fluorescence was detected under the magic angle with a peltier cooled photomultiplier tube (PMT) (PMA-C 192-N-M, Picoquant GmbH) and integrated electronics (PicoHarp 300E, Picoquant GmbH). A monochromator with a spectral width of 4 nm was used to select the required emission wavelength. The response function of the system, which was measured with a scattering Ludox solution (DuPont), had a full width at half-maximum (FWHM) of about 300 ns. The ratio of stop to start pulses was kept low (below 0.05) to ensure good statistics. The luminescence decay curve was measured at the maximum of the emission peak. The data was analyzed with the FluoFit Software program (Picoquant GmbH, Germany). The support plane approach was used to estimate the errors of the decay times.

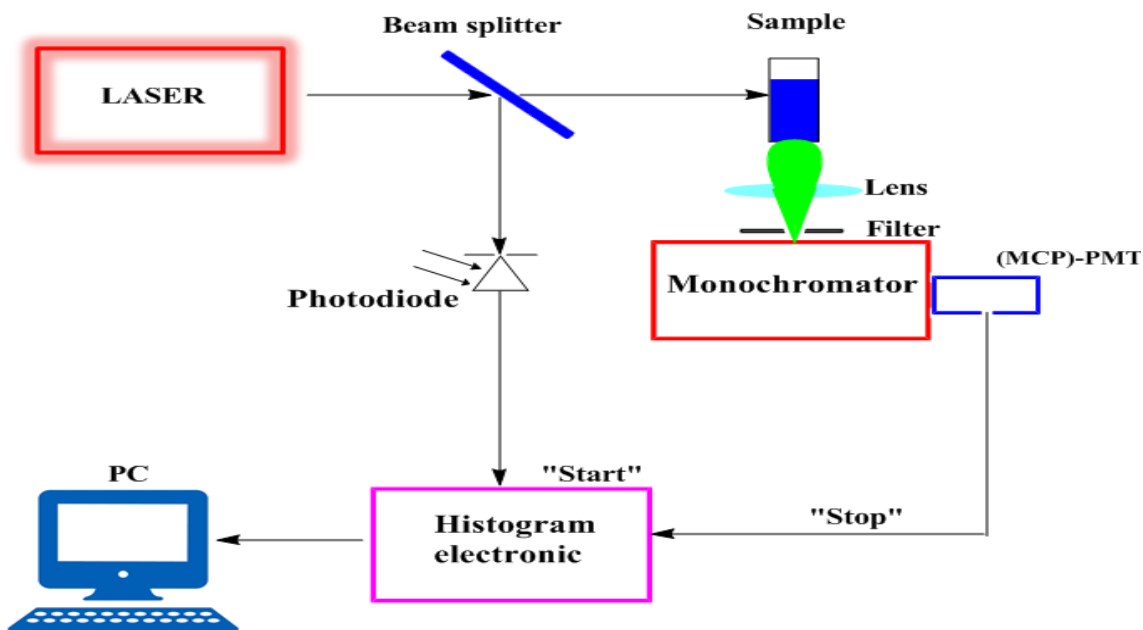


Figure 2.1: Schematic diagram of a TCSPC setup.

(MCP)-PMT= (Multichannel plate detector)-Photomultiplier tube, PC= Personal computer

4. Elemental Analyses (CHNS) were done using a Vario-Elementar Microcube ELIII Series.
5. Energy dispersive X-ray spectroscopy (EDX) was done on an INCA PENTA FET coupled to the VAGA TESCAM using 20 kV accelerating voltage.
6. Dynamic light scattering (DLS) experiments were done on a Malvern Zetasizer Nanoseries, Nano-ZS90.
7. Mass spectral data were collected with a Bruker AutoFLEX III Smartbeam TOF/TOF Mass spectrometer operated in the positive mode using  $\alpha$ -cyano-4-hydroxycinnamic acid as the MALDI matrix.
8. Transmission electron microscopy (TEM) images for the MNPs were obtained using a ZEISS LIBRA<sup>®</sup> TEM.

9. Scanning electron microscopy (SEM) images of the electrospun nanofibers were examined using a scanning electron microscope (JOEL JSM 840 scanning electron microscope) at an accelerating voltage of 20 kV.

10. Perkin Elmer TGA 7 Thermogravimetric analyser was used to study the thermal properties of the electrospun fibers under an inert nitrogen atmosphere flowing at 20 mL<sup>-1</sup> heating at a rate of 10 °C min<sup>-1</sup>.

11. Nitrogen adsorption/desorption isotherms were carried out at 77 K using a Micrometrics ASAP 2020 Surface Area and Porosity Analyzer. Prior to each measurement, degassing was carried at 50 °C for 48 h per sample. The Brunauer–Emmett–Teller (BET) method was employed to determine surface area and porosity. The BET surface area and total pore volume were calculated from the isotherms obtained.

12. A Metrohm Swiss 827 pH meter was used for all pH measurements.

13. X-ray powder diffraction patterns were recorded on a Bruker D8 Discover equipped with a LynxEye detector, using CuK $\alpha$  radiation ( $\lambda = 1.5405 \text{ \AA}$ , nickel filter). Data were collected in the range from  $2\theta = 5^\circ$  to  $100^\circ$ , scanning at  $1^\circ \text{ min}^{-1}$  with a filter time-constant of 2.5 s per step and a slit width of 6.0 mm. Samples were placed on a zero background silicon wafer slide. The X-ray diffraction data were treated using Eva (evaluation curve fitting) software. Baseline correction was performed on each diffraction pattern.

14. Triplet quantum yields were determined using a laser flash photolysis system (**Figure 2.2**). EKSPLA NT342N-20-AW tunable wavelength laser with excitation pulses (3-5 ns) was used as the laser. The analysing beam source was from a Thermo Oriel Xenon arc lamp, and photomultiplier tube (a Kratos Lis Projekte MLIS-X3) was used as a detector. Signals were

recorded with a two-channel 300 MHz digital real time oscilloscope (Tektronix TDS 3032C) and the kinetic curves were averaged over 256 laser pulses.

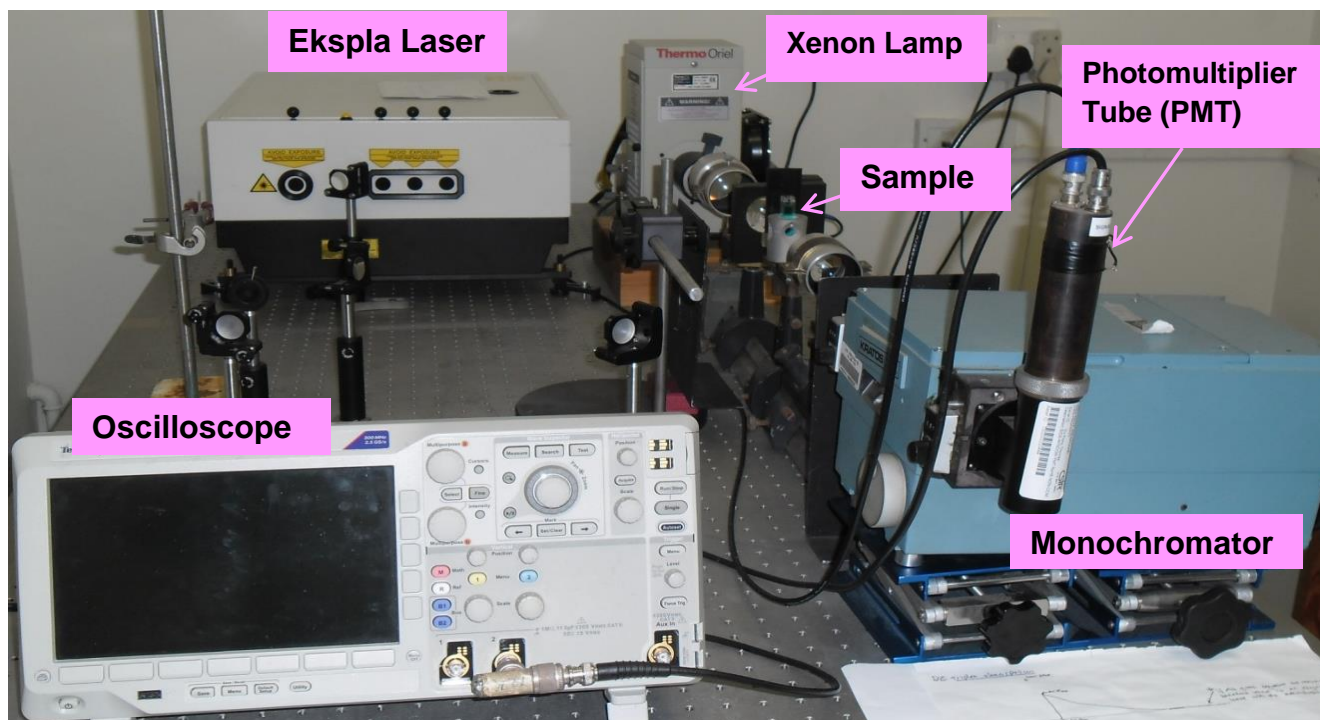


**Figure 2.2:** Laser flash photolysis setup.

15. X-ray photoelectron spectroscopy (XPS) analysis was done using an AXIS Ultra DLD, with Al (monochromatic) anode equipped with a charge neutraliser, supplied by Kratos Analytical. The following parameters were used: the emission was 10 mA, the anode (HT) was 15 kV and the operating pressure below  $5 \times 10^{-9}$  torr. A hybrid lens was used and resolution to acquire scans was at 160 eV pass energy in slot mode. The centre used for the scans was at 520 eV with a width of 1205 eV, with steps at 1 eV and dwell time at 100 ms as reported before [134]. The high resolution scans were acquired using 80 eV pass energy in slot mode.



16. The electrospun fibers were obtained from an electrospinning setup consisting of a high voltage source (Glassman High Voltage. Inc.m series, 0-40 kV), a pump (Kd Scientific, KDS-100-CE) and a plastic syringe equipped with a steel needle with diameter of a 0.60 mm,

**Figure 2.3.** An aluminium foil was as a ground collector for the fibers.

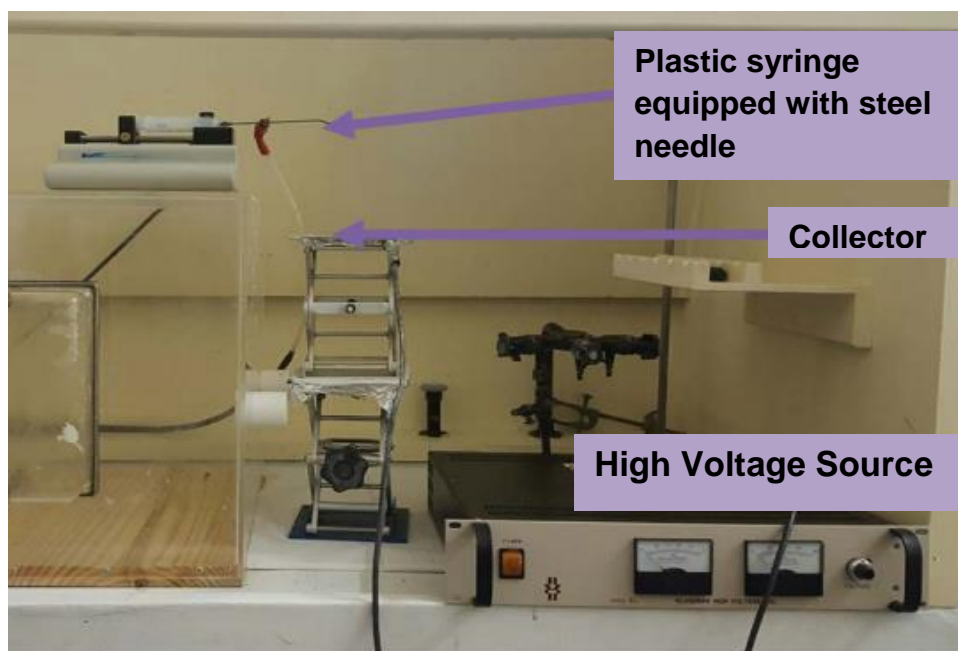


**Figure 2.3:** Electrospinning setup.

17. Irradiations for singlet oxygen determination were conducted using a general electric quartz lamp (300W), 600 nm glass (Schott) and water filters were used to filter off ultraviolet and far infrared radiations respectively, **Figure 2.4.** An interference filter of 670 nm with a band of 40 nm was placed in the light path just before the cell containing the sample. The intensity of the light reaching the cell was measured with a POWER MAX 5100 (Molelectron Detector Incorporated) power meter.

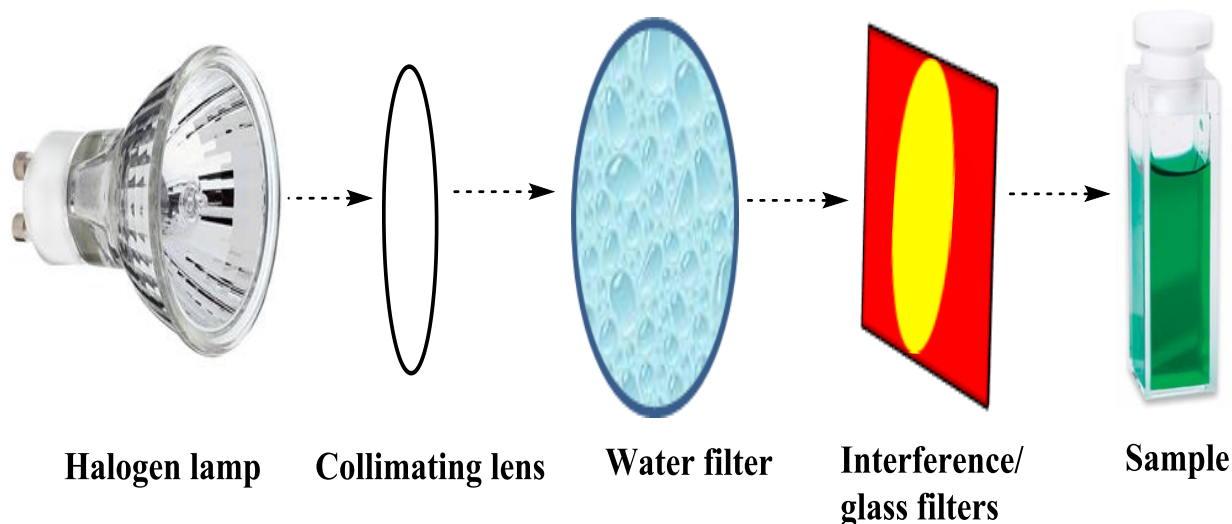


**Figure 2.4:** Schematic diagram of photochemical setup.

18.  $^1\text{H}$  nuclear magnetic resonance spectra were recorded on a Bruker AMX 400 MHz NMR spectrometer.

19. IR spectra were recorded on a Perkin-Elmer Spectrum 100 ATR FT-IR spectrometer.

20. Photocatalysis of pollutants was carried out using the Modulight® Medical Laser system (ML) 7710-680 with cylindrical output channels, aiming beam, integrated calibration module, foot/hand switch pedal, fiber sensors (subminiature version A) connectors and safety interlocks. The system was equipped with a magnetic stirrer and using a sample holder with spot diameter of 5.5 cm. The instrument setup is shown in **Figure 2.5**.

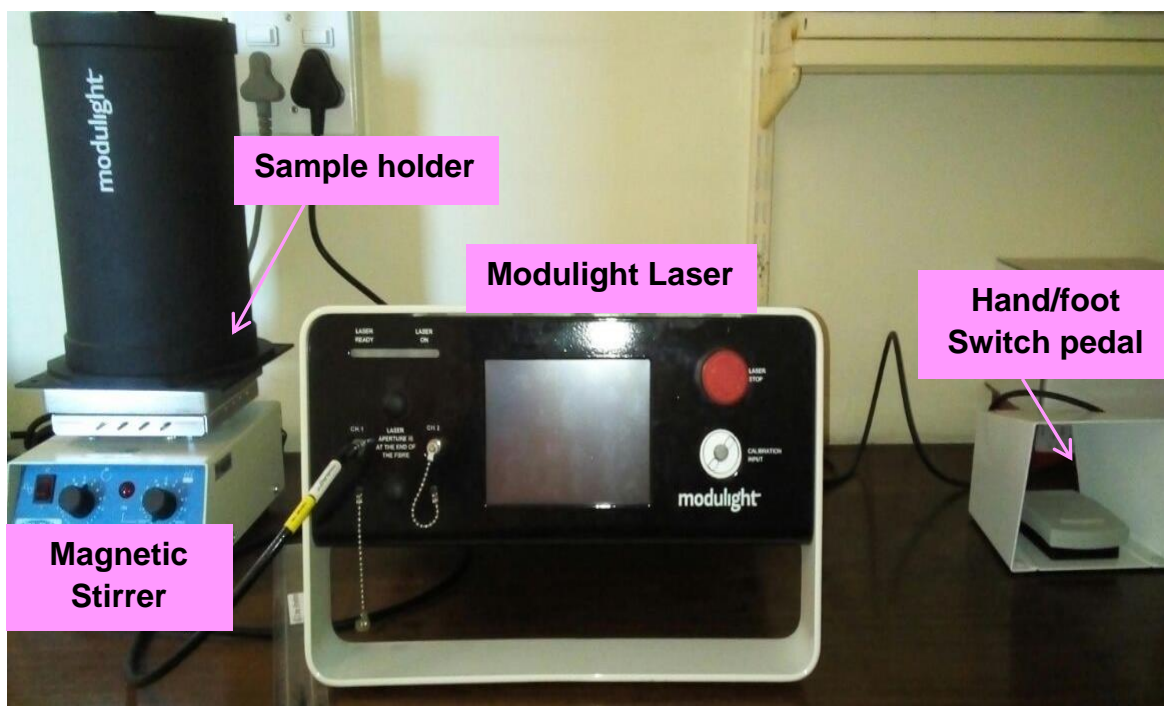


**Figure 2.5:** Photodegradation laser setup.

## 2.3 Phthalocyanine synthesis

### 2.3.1 2-[dimethyl 5-(phenoxy)-isophthalate] 9(10), 16(17), 23(24)-tri-*tert*-butyl phthalocyaninato zinc (II) (5) (Scheme 3.1)

Dimethyl 5-(3,4-dicyanophenoxy)-isophthalate (**8**) (100 mg, 0.297 mmol) and 4-(*tert*-butyl)phthalonitrile (**9**) (383, 2.08 mmol) were reacted with  $\text{Zn}(\text{OAc})_2$  (0.041 g, 0.19 mmol) and 0.3 mL of catalytic DBU in 1-pentanol (5 mL). The reaction mixture was heated to 200 °C with reflux under argon for 8 h followed by cooling to room temperature. The product was precipitated and subsequently washed with methanol followed by isolation of the required product (**5**) from its constitutional isomers with silica gel column chromatography using DCM/methanol (9:1) as eluents.

Yield= 33%.  $^1\text{H}$  NMR (400 MHz,  $\text{CDCl}_3$ ):  $\delta$  (ppm) 1.27 (s, 9H,  $\text{C}(\text{CH}_3)_3$ ), 1.31 – 1.43 (m, 18H,  $\text{C}(\text{CH}_3)_3$ ), 2.15-2.17 (d,  $J = 8.0$  Hz, 6H,  $\text{COOCH}_3$ ), 6.68 (s, 1H, Ar-**H**), 7.01 (s, 6H, Ar-**H**), 7.97 (m, 3H, Ar-**H**), 9.29(s, 5H, Ar-**H**). FT-IR ( $\text{V}_{\text{max}}/\text{cm}^{-1}$ ): 1286, 1350 (C-N), 1256, 1620 (C-O), 1756 (C=O) 2942 (C-H aromatic). UV-Vis (toluene):  $\lambda_{\text{max}}$  (nm) ( $\log \epsilon$ ): 676 (5.20), 610 (4.45), 348 (4.72). Calc. for  $\text{C}_{54}\text{H}_{48}\text{N}_8\text{O}_5\text{Zn}$ : C 67.96, H 5.07, N 11.74; Found: C 68.22, H 5.38, N 10.83. MS (MALDI-TOF)  $m/z$ : Calc. 952.3; Found  $[\text{M}]^+$  953.0.

### 2.3.2. 2-[5-(phenoxy)-isophthalic acid] 9(10), 16(17), 23(24)-tri-*tert*-butyl phthalocyaninato zinc (II) (6) (Scheme 3.1)

The hydrolysis of complex **5** to obtain complex **6** was then done as follows: complex **5** (0.1 g, 0.11 mmol) was dissolved in 5 mL THF followed by addition of 5 M NaOH. The resulting reaction mixture was stirred for 48 h at 80 °C under reflux. THF was then evaporated from the reaction mixture and dilute HCl was added to precipitate out the Pc. The precipitate was filtered and dried to obtain complex **6**.

Yield= 68%.  $^1\text{H}$  NMR (400 MHz,  $\text{DMSO-d}_6$ ):  $\delta$  (ppm) 1.12 – 1.47 (m, 9H,  $\text{C}(\text{CH}_3)_3$ ), 1.59 – 1.99 (m, 18H,  $\text{C}(\text{CH}_3)_3$ ), 6.98-7.18 (m, 4H, Ar-**H**), 7.76-7.80 (d,  $J = 16.0$  Hz, 6H, Ar-**H**), 8.23-8.28 (m, 3H, Ar-**H**), 9.29-9.44 (s, 2H, Ar-**H**), 12.32 (s, 2H,  $\text{COOH}$ ). FT-IR ( $\text{V}_{\text{max}}/\text{cm}^{-1}$ ): 1290 (C-N), 1675 (C=O), 2958 (C-H aromatic), 3250 (O-H). UV-Vis (DMSO):  $\lambda_{\text{max}}/\text{nm}$  ( $\log \epsilon$ ): 676 (5.21), 609 (4.51), 349 (4.91). Calc. for  $\text{C}_{52}\text{H}_{44}\text{N}_8\text{O}_5\text{Zn}$ : C 67.42, H 4.79, N 12.10; Found: C, 67.23, H 4.00 N, 11.05. MS (MALDI-TOF)  $m/z$ : Calcd. 924.3; Found  $[\text{M}]^+$  924.9.

## **2.4 Synthesis and functionalisation of CoFe<sub>2</sub>O<sub>4</sub> MNPs**

### **2.4.1 Oleic acid coated CoFe<sub>2</sub>O<sub>4</sub> MNPs (Scheme 3.2)**

The magnetite nanoparticles were prepared by the conventional co-precipitation method, using previously reported procedures [135] with modifications. Briefly, iron (III) chloride hexahydrate (25 mL, 0.4 M) and cobalt (II) chloride (25 mL, 0.2 M) were stirred together. Sodium hydroxide (25 mL, 3 M) was then added dropwise to the salt solution until a pH of 11–12 was reached. Oleic acid (2 mL) was added dropwise to the solution as a surfactant and the solution was then heated to a temperature of 80 °C while stirring for 1 h. The formed precipitate was washed twice with deionised water and then with ethanol to remove excess oleic acid followed by redispersion in deionized water.

### **2.4.2 Silica coated magnetic nanoparticles (CoFe<sub>2</sub>O<sub>4</sub>-SiO<sub>2</sub> MNPs, Scheme 3.2)**

The CoFe<sub>2</sub>O<sub>4</sub> MNPs were encapsulated with silica for easy functionalisation as reported previously [136]. Firstly, 80 mL ethanol, 169 µL TEOS and 14.4 µL APTMS were mixed in a beaker and subsequently 20 mL of the oleic acid capped CoFe<sub>2</sub>O<sub>4</sub> MNPs were added dropwise to the mixture while stirring at room temperature. Stirring was continued for 3 h and the silica coated cobalt ferrite nanoparticles (CoFe<sub>2</sub>O<sub>4</sub>-SiO<sub>2</sub>) were collected with a magnet. The nanoparticles were then washed three times with deionized water and then dried under vacuum overnight.

### **2.4.3 Amine functionalised CoFe<sub>2</sub>O<sub>4</sub> magnetic nanoparticles (CoFe<sub>2</sub>O<sub>4</sub>-NH<sub>2</sub> MNPs, Scheme 3.2)**

After coating the CoFe<sub>2</sub>O<sub>4</sub> nanoparticles with a silica shell, the surfaces of the nanoparticles were modified with amine groups using APTES [136] as follows: the CoFe<sub>2</sub>O<sub>4</sub>-SiO<sub>2</sub> MNPs (600 mg), 12 mL DMF and 8 mL toluene were vortexed in a 50 mL tube and then magnetically stirred while 200 µL APTES was added dropwise into the mixture. The stirring was continued for 24 h following the addition of APTES, then the functionalised nanoparticles (CoFe<sub>2</sub>O<sub>4</sub>-NH<sub>2</sub> MNPs) were collected with the magnet and washed with toluene. These nanoparticles were then finally dispersed in 10 mL DMF.

### **2.4.4 Carboxylic acid functionalised magnetic nanoparticles (CoFe<sub>2</sub>O<sub>4</sub>-COOH MNPs, Scheme 3.2)**

A ring opening linker elongation reaction was used to add carboxylic acid groups to the amine functionalised CoFe<sub>2</sub>O<sub>4</sub> nanoparticles [136]. Succinic anhydride was added and its ring structure was opened and reacted with the amine groups of the CoFe<sub>2</sub>O<sub>4</sub>-NH<sub>2</sub> MNPs as follows: 10 mL homogenous colloid suspension of the CoFe<sub>2</sub>O<sub>4</sub>-NH<sub>2</sub> MNPs was added dropwise to a 10 mL DMF solution containing 0.1 g (1.0 mmol) succinic anhydride and the mixture was stirred for 24 h at room temperature. The modified nanoparticles were washed and redispersed in DMF and kept for further use.

### **2.4.5 Synthesis of glutathione functionalised CoFe<sub>2</sub>O<sub>4</sub> magnetic nanoparticles (CoFe<sub>2</sub>O<sub>4</sub>-GSH MNPs, Scheme 3.3)**

The MNPs were prepared by the conventional co-precipitation method, using previously reported procedures [137] with modifications as follows: iron (III) chloride hexahydrate (25

mL, 0.4 M) and cobalt (II) chloride hexahydrate (25 ml, 0.2 M) were mixed together. Ammonium hydroxide (25%) was added dropwise to the solution until a pH of 10-12 was reached. The solution was then heated to 85 °C for 1 h and then cooled to room temperature. The precipitated nanoparticles were then retrieved by magnetic decantation, washed with deionised water three times and then dried overnight under vacuum to form the bare CoFe<sub>2</sub>O<sub>4</sub> MNPs. The bare CoFe<sub>2</sub>O<sub>4</sub> MNPs were modified by anchoring of glutathione (GSH) onto the surface of the ferrite as reported before [138] with slight modifications as follows: bare CoFe<sub>2</sub>O<sub>4</sub> MNPs (0.5 g) were dispersed in a solvent mixture of water (15 mL) and methanol (5 mL) and sonicated for 15 min. Reduced glutathione was then dissolved in water (15 mL) and added to the solvent mixture dropwise followed by sonication for a further 2 h. The resultant CoFe<sub>2</sub>O<sub>4</sub>-GSH MNPs were then magnetically separated, washed with methanol and dried under vacuum overnight.

## **2.5 Conjugation of Pc complexes to CoFe<sub>2</sub>O<sub>4</sub> MNPs**

### **2.5.1 Conjugation of complexes 1, 4 and 6 to CoFe<sub>2</sub>O<sub>4</sub>-NH<sub>2</sub> MNPs (Scheme 3.4)**

The conjugation of complexes **1** and **6** to the CoFe<sub>2</sub>O<sub>4</sub>-NH<sub>2</sub> MNPs was done using a method previously reported before in the conjugation of Pcs to other nanoparticles [72]. The carboxylic acid functional groups on the Pc were activated by adding the Pcs (0.1 g) to DCC (1.03 g, 5 mmol) in 5 mL DMSO followed by stirring for 12 h. NHS (0.58 g, 5 mmol) and CoFe<sub>2</sub>O<sub>4</sub>-NH<sub>2</sub> MNPs (0.38 g) were then added to the mixture followed by stirring for 48 h. The final products; **1**-CoFe<sub>2</sub>O<sub>4</sub> and **6**-CoFe<sub>2</sub>O<sub>4</sub> were washed with ethanol and toluene followed by drying.

The conjugation of the water soluble complex **4** to the CoFe<sub>2</sub>O<sub>4</sub>-NH<sub>2</sub> MNPs on the other hand was done as reported before [70]. The carboxylic acid groups of the Pc were activated by

dissolving complex **4** (0.15 g, 0.12 mmol) in 5 ml of PBS (pH 7.4), followed by addition of EDC (1.61 g, 7.8 mmol) and NHS (0.84 g, 7.0 mmol). The solution was then stirred for 6 h. The CoFe<sub>2</sub>O<sub>4</sub>-NH<sub>2</sub> MNPs (5 mg) were sonicated in 5 ml PBS (pH 7.4) and subsequently added dropwise to the complex **4** solution. The mixture was stirred for 12 h at room temperature under a N<sub>2</sub> gas flow. The product (**4**-CoFe<sub>2</sub>O<sub>4</sub>) was precipitated by addition of ethanol, a magnet was also used to separate the **4**-CoFe<sub>2</sub>O<sub>4</sub> from the unreacted Pcs.

### **2.5.2 Conjugation of complex 2 to CoFe<sub>2</sub>O<sub>4</sub>-COOH MNPs (Scheme 3.5)**

The conjugation of complex **2** to the CoFe<sub>2</sub>O<sub>4</sub>-COOH MNPs was done as reported before [139]. A mixture of 0.10 g of CoFe<sub>2</sub>O<sub>4</sub>-COOH and DCC (0.02 g, 0.097 mmol) was stirred in 4 mL DMF at room temperature for 48 h to activate the carboxylic acid terminal groups of the CoFe<sub>2</sub>O<sub>4</sub>-COOH MNPs. Complex **2** (0.1 g, 0.089 mmol) was then dissolved in 2 mL DMF and added dropwise to the CoFe<sub>2</sub>O<sub>4</sub>-COOH mixtures respectively, followed by continuous stirring for a further 48 h to get the crude product which was then collected and washed several times by centrifugation in acetone, methanol and absolute ethanol in succession. The obtained product is denoted **2**-CoFe<sub>2</sub>O<sub>4</sub>-COOH i.e. since complex **2** is conjugated to two different MNPs (CoFe<sub>2</sub>O<sub>4</sub>-COOH and CoFe<sub>2</sub>O<sub>4</sub>-GSH (below), the capping ligands are shown in their names for clarity.

### **2.5.3 Conjugation of complexes 2 and 7 to CoFe<sub>2</sub>O<sub>4</sub>-GSH MNPs (Scheme 3.6)**

The conjugation of complexes **2** and **7** to CoFe<sub>2</sub>O<sub>4</sub>-GSH MNPs were also done as reported before [139] (Scheme 3.6, using complex **2** as an example). In two separate round bottomed flasks, a mixture of 0.10 g of CoFe<sub>2</sub>O<sub>4</sub>-GSH and DCC (0.02 g, 0.097 mmol) was stirred in 4 mL DMF at room temperature for 48 h to activate the carboxylic acid terminal groups of



the CoFe<sub>2</sub>O<sub>4</sub>-GSH MNPs. Complexes **2** (0.1 g, 0.089 mmol) and **7** (0.1 g, 0.087 mmol) were then each dissolved in 2 mL DMF and added dropwise to the separate CoFe<sub>2</sub>O<sub>4</sub>-GSH reaction mixtures respectively, followed by continuous stirring for a further 48 h. The crude products; **2**-CoFe<sub>2</sub>O<sub>4</sub>-GSH and **7**-CoFe<sub>2</sub>O<sub>4</sub> respectively were collected and washed several times by centrifugation in acetone, methanol and absolute ethanol in succession.

In order to study the importance of having a covalent bond between the Pcs and CoFe<sub>2</sub>O<sub>4</sub> MNPs in enhancing their photocatalytic behavior, samples without a covalent bond were prepared (using complexes **2** and **7** as examples). The same amounts of CoFe<sub>2</sub>O<sub>4</sub>-GSH MNPs and complexes **2** and **7** respectively were reacted but without the addition of DCC. All the conditions and purification methods were the same as those for the covalent conjugation. The obtained products were denoted **2**-CoFe<sub>2</sub>O<sub>4</sub>-GSH (mix) and **7**-CoFe<sub>2</sub>O<sub>4</sub> (mix) respectively.

The conjugation of complexes **3** and **5** to the CoFe<sub>2</sub>O<sub>4</sub> MNPs was not possible because the Pcs do not have the necessary functional moieties required for amide bond formation with the MNPs.

## **2.6 Preparation of functionalised electrospun fibers**

### **2.6.1 Preparation of functionalised polystyrene (PS) fibers**

Homogenous PS solutions were prepared by dissolving PS in DMF:THF (4:1) (to make a 20% solution with final volume of 20 mL) followed by stirring at room temperature for 24 h. The PS fibers were then obtained by electrospinning the PS solution using a voltage of 15 kV, 0.15 mL/h flow rate and a tip to collector distance (TCD) of 12 cm. With evaporation of

the solvent, the PS fibers were deposited on a grounded collector (12 cm x 6 cm) covered with aluminium foil. Similar conditions were used for the fibers functionalised with the Pcs (complexes **1** and **2**), CoFe<sub>2</sub>O<sub>4</sub> MNPs (CoFe<sub>2</sub>O<sub>4</sub>-NH<sub>2</sub> and CoFe<sub>2</sub>O<sub>4</sub>-COOH) and their respective conjugates (**1**-CoFe<sub>2</sub>O<sub>4</sub> and **2**-CoFe<sub>2</sub>O<sub>4</sub>) wherein 120 mg of each of the photocatalysts was added to the PS solution followed by stirring for a further 24 hours. The resulting modified fibers were represented as CoFe<sub>2</sub>O<sub>4</sub>-NH<sub>2</sub>/PS, CoFe<sub>2</sub>O<sub>4</sub>-COOH/PS, **1**/PS, **2**/PS, **1**-CoFe<sub>2</sub>O<sub>4</sub>/PS and **2**-CoFe<sub>2</sub>O<sub>4</sub>/PS. The functionalised PS fibers were applied in the photocatalytic degradation of OG. When water soluble Pc (complex **4**) was electrospun with PS and applied in photocatalysis, there was observed leaching of the Pc from the fibers. Studies were therefore also conducted on a different polymer; polyamide-6 (PA-6) as an alternative fiber support.

### **2.6.2 Preparation of functionalised polyamide-6 (PA-6) fibers**

The preparation of homogenous PA-6 solution was achieved by dissolving PA-6 in FA/AA (1:1) (to make a 25% solution with final volume of 30 mL) followed by stirring at room temperature for 24 h. The PA-6 fibers were then obtained by electrospinning the PA-6 solution using a voltage of 20 kV, 0.8 mL/h flow rate, a tip to collector distance (TCD) of 10 cm and a ground collector (12 cm x 6 cm). Similar conditions were used for functionalisation of the fibers with the Pcs (complexes **4** and **6**), CoFe<sub>2</sub>O<sub>4</sub>-NH<sub>2</sub> MNPs and their respective conjugates (**4**-CoFe<sub>2</sub>O<sub>4</sub> and **6**-CoFe<sub>2</sub>O<sub>4</sub>) wherein 40 mg of each of the photocatalysts was added to the PA-6 solution followed by stirring for a further 24 h. The resulting modified fibers were represented as CoFe<sub>2</sub>O<sub>4</sub>-NH<sub>2</sub>/PA-6, **4**/PA-6, **6**/PA-6, **4**-CoFe<sub>2</sub>O<sub>4</sub>/PA-6 and **6**-CoFe<sub>2</sub>O<sub>4</sub>/PA-6.

Due to time constraints, the electrospinning of complex **7** as well as **2-CoFe<sub>2</sub>O<sub>4</sub>-GSH**, **7-CoFe<sub>2</sub>O<sub>4</sub>**, **2-CoFe<sub>2</sub>O<sub>4</sub>-GSH (mix)** and **7-CoFe<sub>2</sub>O<sub>4</sub> (mix)**, was not done and will be the subject of future work.

## 2.7 Photocatalysis

All the photocatalytic reactions were carried out in a magnetically stirred beaker using the laser setup shown in **Figure 2.5** as the photoexcitation source. The transformation of the pollutants was spectroscopically monitored post irradiation, using a Shimadzu UV-2550 spectrophotometer. The absorption bands of OG and MO were monitored at 476 nm and 464 nm respectively at pH 7.4. At pH 2.5, the absorption band of MO was then monitored at 506 nm while those of Cr(VI) was monitored at 252 nm and 349 nm. All the experiments were carried out under aerobic conditions using a range of concentrations of the pollutants.

## 2.8 Photophysical and photochemical methods

### 2.8.1 Fluorescence quantum yields ( $\Phi_F$ ) and Lifetimes ( $\tau_F$ )

The fluorescence quantum yields of the Pcs and their respective Pc-MNP conjugates reported herein were determined in either DMSO or toluene using the comparative method, **Equation 1.1** discussed in the previous chapter. An unsubstituted zinc ZnPc in DMSO with  $\Phi_F^{\text{Std}} = 0.2$  [140] (corrected for toluene using refractive indices) was employed as the standard. Both the sample and standard were excited at the same wavelength. Preparation of the solutions for the standard and samples were done such that their absorbances at the excitation wavelength were about 0.05 to avoid filter effects. The lifetimes of the Pcs were measured using a TCSPC setup (**Figure 2.1**) by exciting at the excitation wavelength of the Pcs.

### 2.8.2 Triplet quantum yields ( $\Phi_T$ ) and Lifetimes ( $\tau_T$ )

The decay kinetics of the triplet absorption of the Pcs and their respective Pc-MNP conjugates were obtained from the laser flash photolysis setup, **Figure 2.2**. Preparation of the sample solutions and the standard entailed adjusting their absorbances to be approximately 1.5 at the Q-band maxima. The solutions were introduced into 1 cm quartz cells and bubbled through with argon to remove dissolved oxygen before taking the readings. The triplet quantum yields of the samples were determined using **Equation 1.2**. Unsubstituted ZnPcs in DMSO  $\Phi_T^{\text{Std}} = 0.65$  [141] or toluene  $\Phi_T^{\text{Std}} = 0.65$  [142] were used as standards. Triplet lifetimes were determined from kinetic data obtained from Origin Pro 8 software.

### 2.8.3 Singlet oxygen quantum yields ( $\Phi_\Delta$ )

A chemical comparative method was used for the determination of  $\Phi_\Delta$  of the Pcs and their respective conjugates in DMSO, toluene and water using the experimental setup shown in **Figure 2.4**. The experiments were conducted in the presence of air wherein 1.5 mL of each of the sample solutions was prepared with absorbances of approximately 1 at the Q band. The sample solutions were then mixed with an equal volume of a solution of DPBF or ADMA with concentrations of approximately  $0.3 \mu\text{molL}^{-1}$  to avoid chain reactions. The resulting solution was irradiated at the Q band region and the degradation of DPBF/ADMA was then monitored by recording the UV-vis spectra of the sample solutions. The  $\Phi_\Delta$  values were determined using **Equation 1.5** with ZnPc in DMSO as a standard where  $\Phi_\Delta^{\text{Std}} = 0.67$  [143] and toluene where  $\Phi_\Delta^{\text{Std}} = 0.58$  [144]. AlPcSmix was employed as a standard ( $\Phi_\Delta = 0.42$  [144]) for water soluble Pcs.

Absolute methods were used for determination of the  $\Phi_{\Delta}$  of the functionalised fibers wherein ADMA was used as the singlet oxygen quencher. For each experiment 20 mg of the functionalised fibers were suspended as small pieces in an aqueous solution of ADMA and irradiated using the setup in **Figure 2.4**. The quantum yields of ADMA ( $\Phi_{\text{ADMA}}$ ) were estimated using **Equation 1.8** using the coefficient of ADMA in water,  $\log(\epsilon) = 4.1$  [145] and using the absorbances of the Pcs and their respective conjugates in the polymer fiber matrix.

# Results and Discussion

3. Synthesis and Characterisation
4. Photophysicochemical properties of phthalocyanines and Pc-MNP conjugates
5. Electrospun polymer fibers
6. Photocatalytic treatment of organic and inorganic pollutants

# Publications

The results discussed in the following chapters have been presented in the articles stated below that have been published or submitted for publication in peer-reviewed journals. These articles have not been referenced in this thesis.

1. **S. Mapukata**, F. Chindeka, K. E. Sekhosana, T. Nyokong, Laser induced photodegradation of Orange G using phthalocyanine – cobalt ferrite magnetic nanoparticle conjugates electrospun in polystyrene nanofibers. **J. Mol. Cat. A: Chem.** **439** (2017) 211-223. **Editor's Choice.**
2. **Sivuyisiwe Mapukata**, Olawale L. Osifeko, Tebello Nyokong, Phthalocyanine-cobalt ferrite based nanocomposites as dual photocatalysts for photodegradation of Methyl Orange and photoreduction of Chromium(VI). –**Submitted**
3. **Sivuyisiwe Mapukata**, Nagao Kobayashi, Mutsumi Kimura, Tebello Nyokong, Asymmetrical and symmetrical zinc phthalocyanine-cobalt ferrite conjugates embedded in electrospun fibers for photocatalytic degradation of azo dyes: Methyl Orange and Orange G.-**Submitted.**

# CHAPTER 3

## Results and Discussion



### 3. Synthesis and Characterisation

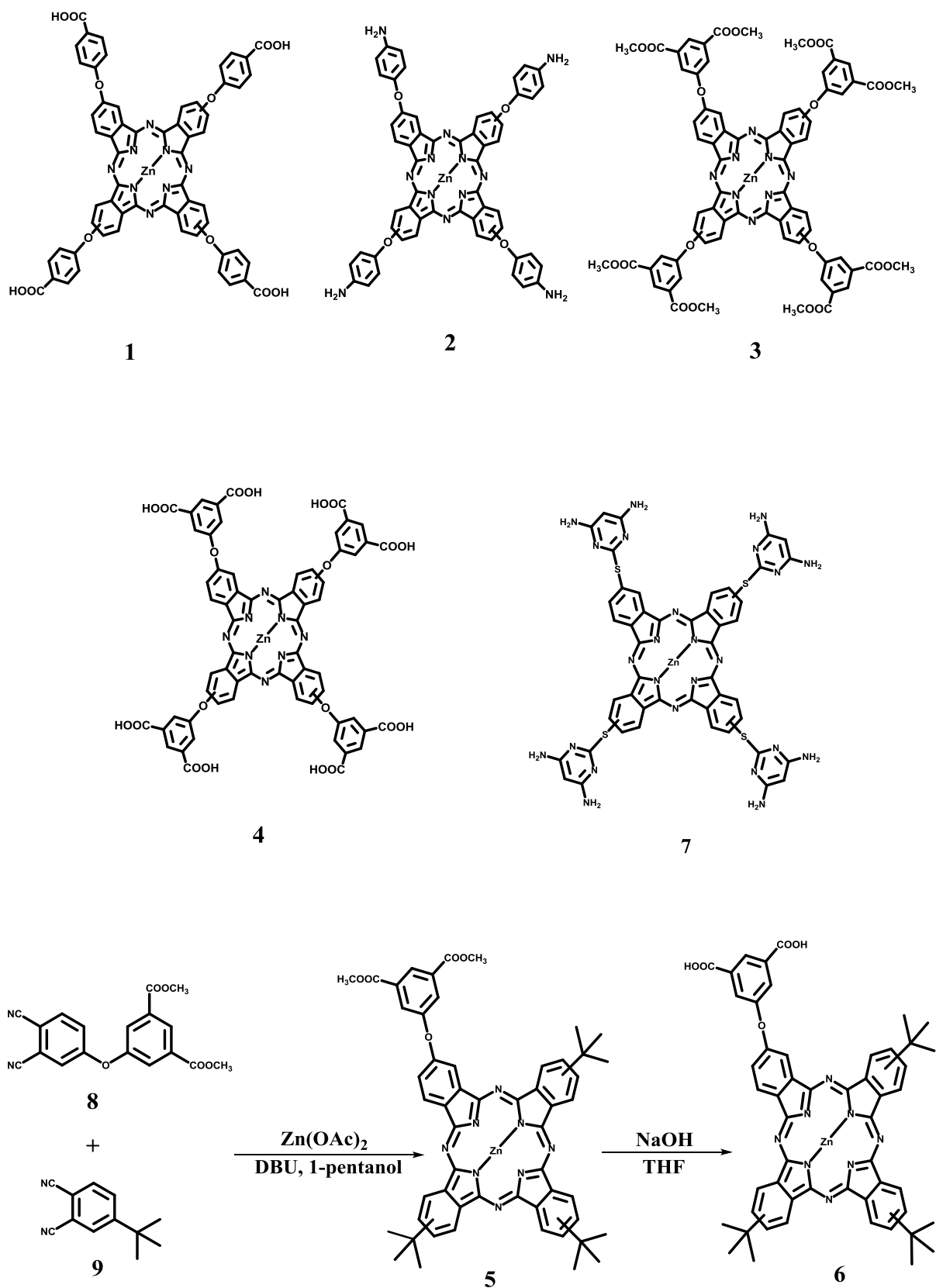
This chapter reports on the synthesis and characterisation of phthalocyanines,  $\text{CoFe}_2\text{O}_4$  MNPs as well as their respective conjugates, all of which have been employed in this thesis.

#### 3.1 Phthalocyanines (Pcs)

##### 3.1.1 Synthesis

All the Pc complexes reported in this work are tetra-substituted and were obtained by cyclotetramerization of their respective phthalonitrile precursors. The synthesis of Pc complexes **1-4** and **7** (Scheme 3.1) has been reported before [58-63] hence their synthesis and characterisation will not be discussed in this thesis. This thesis however reports on the photophysical and photochemical characterisation of complexes **3** and **4** for the first time. The synthesis and characterisation of the unsymmetrical Pcs (**5** and **6**) as well as their photophysical and photochemical properties are also reported herein for the first time. The synthesis of complex **5** was achieved by the statistical condensation of two different phthalonitriles; dimethyl 5-(3,4-dicyanophenoxy)-isophthalate (**8**) and 4-(*tert*-butyl)phthalonitrile (**9**) in the presence of catalytic DBU,  $\text{Zn}(\text{OAc})_2$  for metallation of the Pc and 1-pentanol as the solvent. Complex **6** was then obtained by hydrolysis of complex **5** in the presence of NaOH and THF. The structures of both Pc complexes were confirmed using UV-vis, CHN elemental analysis, FTIR,  $^1\text{H}$  NMR and MS spectroscopic data. The disappearance of the  $\text{C}\equiv\text{N}$  peaks at 2222 and 2230  $\text{cm}^{-1}$  for dimethyl 5-(3,4-dicyanophenoxy)-isophthalate and 4-(*tert*-butyl)phthalonitrile in their FT-IR spectra, respectively confirmed the formation of complex **5**. The  $^1\text{H}$  NMR spectrum for complex **5** displayed aromatic ring proton peaks between 6.68 and 9.29 ppm, and  $\text{CH}_3$

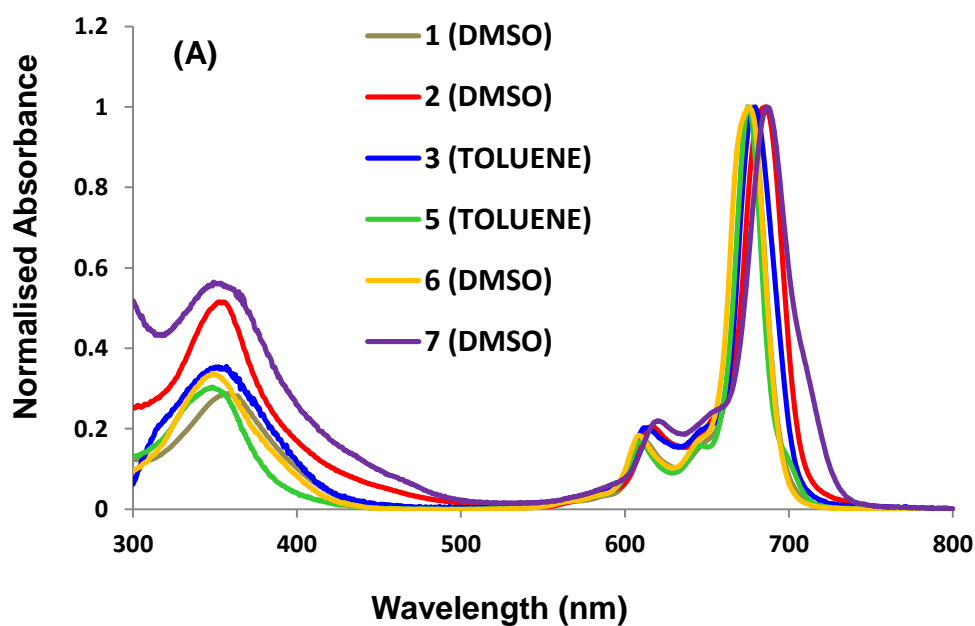
protons between 1.27 and 2.17 ppm. The  $^1\text{H}$  NMR spectra of complex **6** on the other hand showed the disappearance of the protons representing the ester groups at 2.15-2.17 ppm for complex **5**, and the appearance of protons representing the carboxylic acid groups at 12.32 ppm. Peak integration of both complexes **5** and **6** also correctly gave the anticipated total number of protons. Complexes **3** and **5** were found to be soluble in toluene, chloroform and THF, complex **4** was found to be soluble in water and complex **6** was found to be soluble in DMSO and DMF hence their spectroscopic characterizations are done in different solvents.



**Scheme 3.1:** The structures of symmetrical zinc phthalocyanines (**1-4, 7**) as well as the synthesis of asymmetric zinc phthalocyanines (**5** and **6**), all of which have been used in this thesis.

### 3.1.2 UV-vis spectroscopy

The UV-vis spectra of the Pc complexes reported in this work are shown in **Figure 3.1**. The narrow Q band of all the Pc complexes with the exception of complex **4** confirms their monomeric behaviour. In the case of complex **4** in water, there is an observed splitting and broadening of the Q band which is attributed to aggregation of the Pc (**Figure 3.1B**). This is due to the coplanar association of the Pc rings progressing from monomer to dimer and even higher order complexes which can be driven by non-covalent interactions such as  $\pi - \pi$  interactions between the monomer Pcs [146]. The addition of a surfactant; Cremophor EL remedied this and a narrow Q band was then observed. The absorption wavelengths of the Q bands of the Pcs are listed in **Table 3.1**.



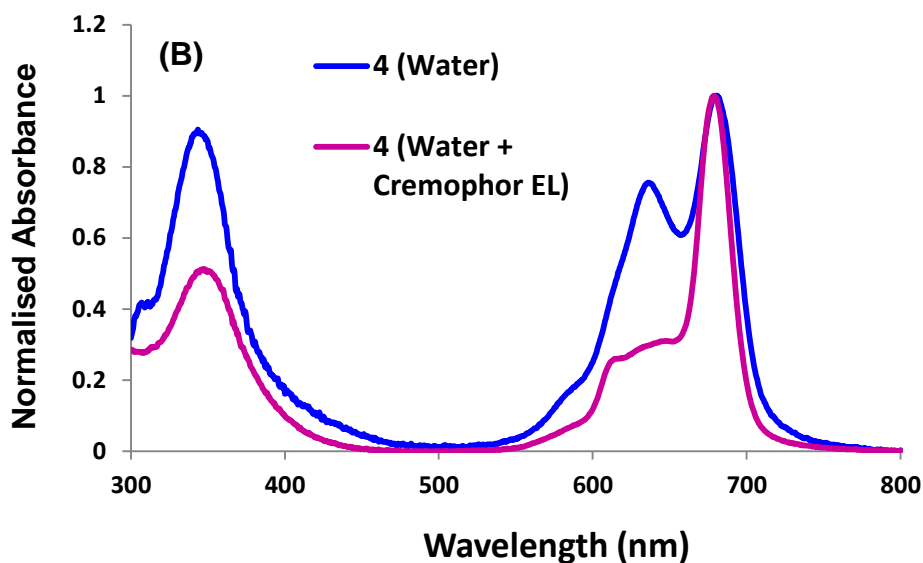


**Figure 3.1:** Normalised ground state absorption spectra of: (A) Pc complexes **1-3** as well as **5-7** and (B) complex **4** in the absence and presence of Cremophor EL (0.25 mL, 500mg/L).

The emission, excitation and absorption spectra of the novel Pc complexes **5** and **6** are shown in **Figure 3.2** (as examples). The emission spectra were observed to be mirror images of the excitation spectra while the latter are similar to the absorption spectra, an indication of non-aggregation of the Pcs in solution. The closeness of the Q band absorption maximum to that of excitation shows that the ground state nuclear configurations are not affected by excitation in either toluene or DMSO. The obtained fluorescence excitation and emission spectra for the Pc complexes **1, 2, 6** and **7** (in DMSO) as well as complexes **3** and **5** (in toluene) are typical for Pc complexes where Stokes shifts for the Pcs in both solvents generally range between 3 to 19 nm [147]. The slight differences between absorbance and excitation wavelengths are due to the differences in equipment used.

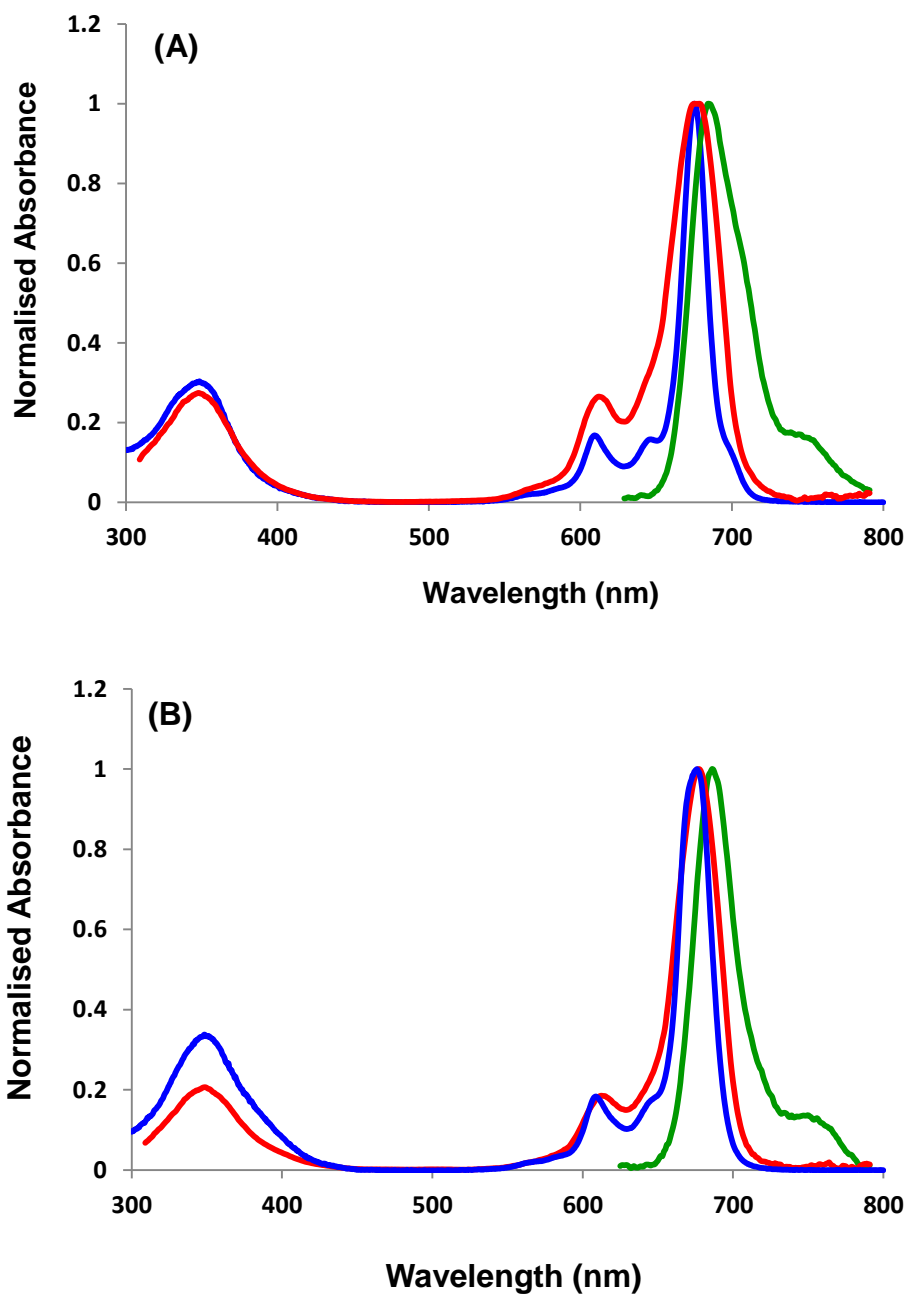


**Figure 3.2:** Normalized absorbance (blue), excitation (red) and emission (green) spectra of: (A) complex **5** in toluene and (B) complex **6** in DMSO.

**Table 3.1:** Ground state absorption, fluorescence excitation and emission spectral parameters for Pc complexes **1-7**.

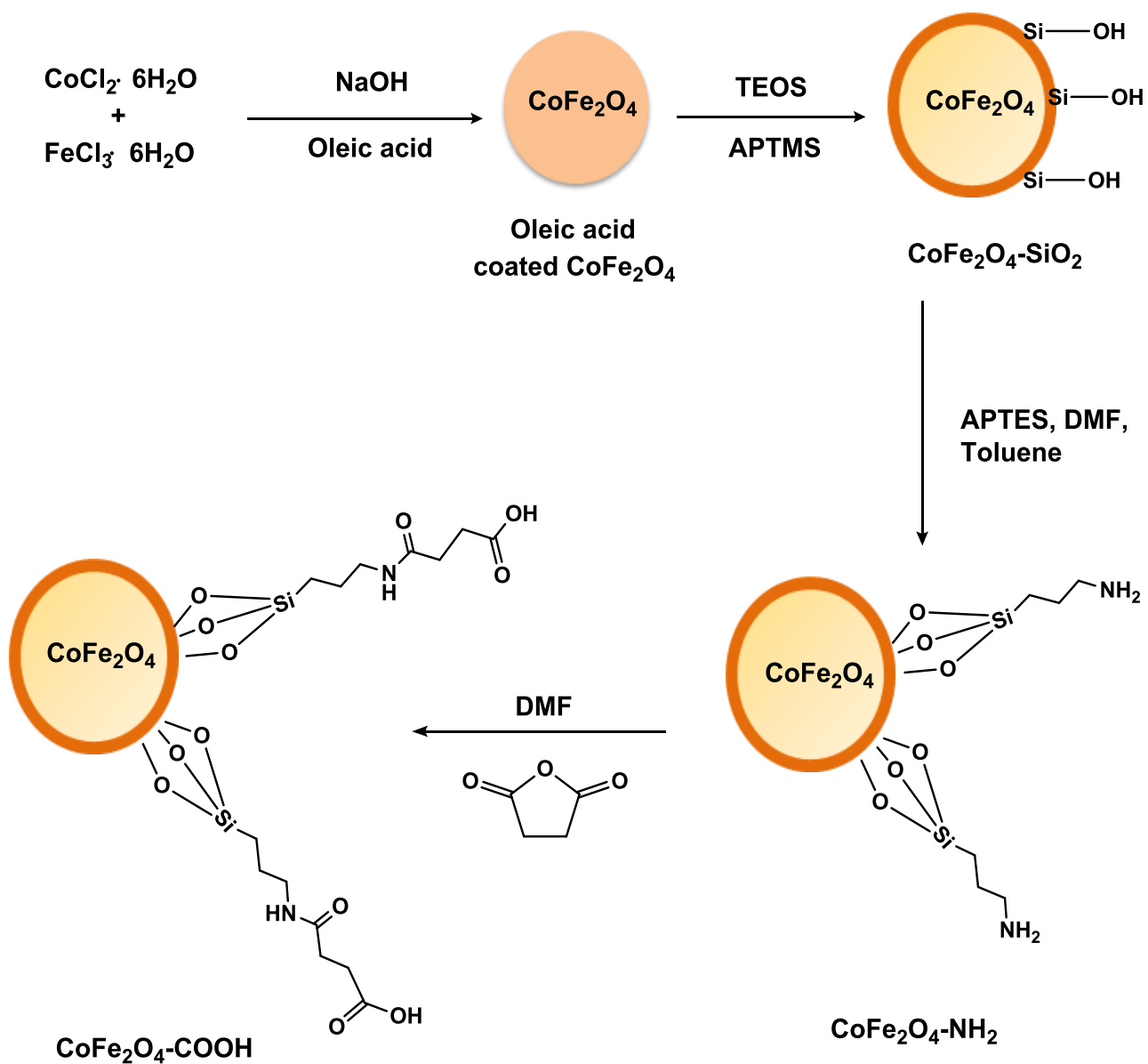
<b>Complex</b>	<b>Solvent</b>	$\lambda_{\text{abs}}$ (nm)	$\lambda_{\text{exc}}$ (nm)	$\lambda_{\text{em}}$ (nm)
<b>1</b>	DMSO	678	678	686
<b>2</b>	DMSO	686	686	695
<b>3</b>	Toluene	680	681	689
<b>4</b>	Water	683	-	-
<b>5</b>	Toluene	676	676	685
<b>6</b>	DMSO	676	677	686
<b>7</b>	DMSO	689	689	700

$\lambda_{\text{abs}}$  = absorption wavelength,  $\lambda_{\text{exc}}$  = excitation wavelength,  $\lambda_{\text{em}}$  = emission wavelength

## **3.2 Synthesis and characterisation of CoFe<sub>2</sub>O<sub>4</sub> MNPs and their respective Pc-CoFe<sub>2</sub>O<sub>4</sub> MNP conjugates**

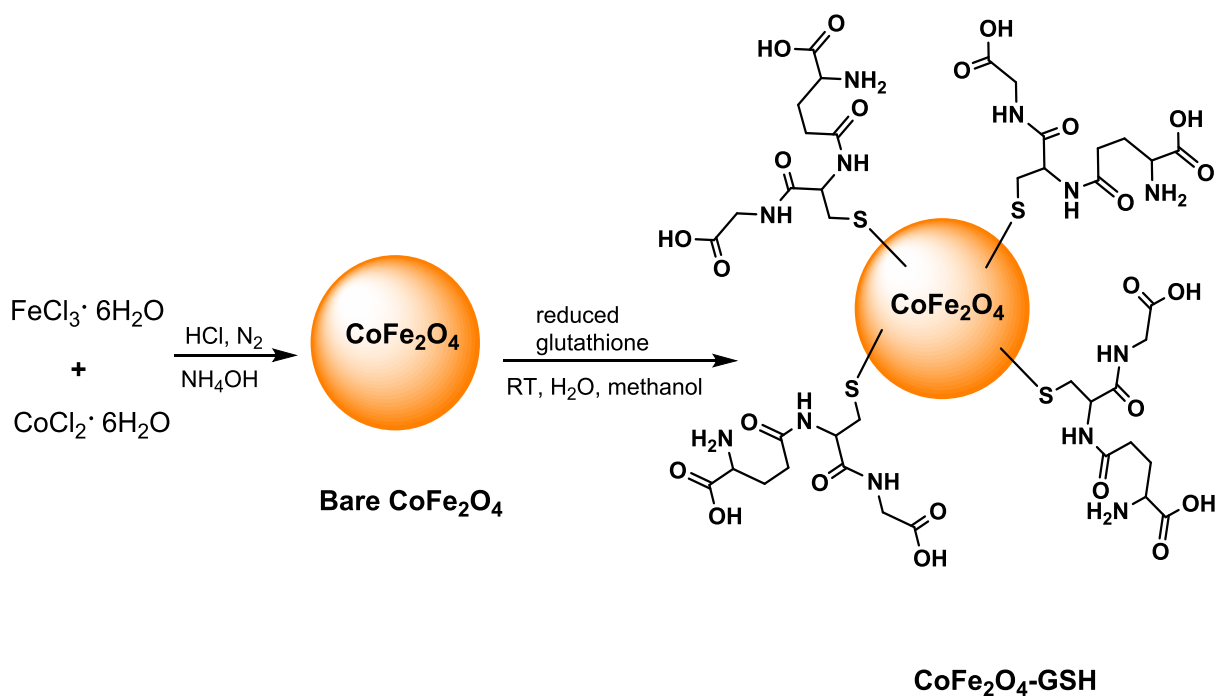
### **3.2.1 Synthesis**

Three differently substituted CoFe<sub>2</sub>O<sub>4</sub> MNPs were synthesised and reported in this work; CoFe<sub>2</sub>O<sub>4</sub>-NH<sub>2</sub> MNPs (**Scheme 3.2**), CoFe<sub>2</sub>O<sub>4</sub>-COOH MNPs (which resulted from functionalising the CoFe<sub>2</sub>O<sub>4</sub>-NH<sub>2</sub> MNPs using succinic anhydride, **Scheme 3.2**) and the CoFe<sub>2</sub>O<sub>4</sub>-GSH MNPs (**Scheme 3.3**) which were functionalised using glutathione (GSH). All three CoFe<sub>2</sub>O<sub>4</sub> MNPs were synthesised using the conventional co-precipitation method, using previously reported procedures [135-138].



**Scheme 3.2:** Synthesis of  $\text{CoFe}_2\text{O}_4\text{-NH}_2$  and  $\text{CoFe}_2\text{O}_4\text{-COOH}$  MNPs.





**Scheme 3.3:** Synthesis of CoFe<sub>2</sub>O<sub>4</sub>-GSH MNPs.

The CoFe<sub>2</sub>O<sub>4</sub>-NH<sub>2</sub> MNPs were linked to the Pc complexes with the carboxylic acid functional groups (complexes **1**, **4** and **6**) following activation of the carboxylic acid groups of the Pcs (**1** and **6**) with DCC/NHS (EDC/NHS for complex **4**) to form the conjugates; **1**-CoFe<sub>2</sub>O<sub>4</sub>, **6**-CoFe<sub>2</sub>O<sub>4</sub> and **4**-CoFe<sub>2</sub>O<sub>4</sub>, respectively (**Scheme 3.4**). The CoFe<sub>2</sub>O<sub>4</sub>-COOH MNPs were activated with DCC followed by formation of the amide bond with complex **2** to form **2**-CoFe<sub>2</sub>O<sub>4</sub>-COOH (**Scheme 3.5**). Lastly the CoFe<sub>2</sub>O<sub>4</sub>-GSH MNPs were activated with DCC followed by formation of the amide bond with complexes **2** and **7** to form **2**-CoFe<sub>2</sub>O<sub>4</sub>-GSH and **7**-CoFe<sub>2</sub>O<sub>4</sub> (**Schemes 3.6**, using complex **2** as an example). In addition composites of the Pc complexes **2** and **7** and the CoFe<sub>2</sub>O<sub>4</sub>-GSH MNPs were prepared where there was no covalent bond between the Pcs and the MNPs resulting in **2**-CoFe<sub>2</sub>O<sub>4</sub>-GSH (mix) and **7**-CoFe<sub>2</sub>O<sub>4</sub> (mix), respectively. Capping ligands are shown in denoting the conjugates of complex **2** for clarity since different ligands were employed.

Based on size considerations {sizes of  $\text{CoFe}_2\text{O}_4\text{-NH}_2$ ,  $\text{CoFe}_2\text{O}_4\text{-COOH}$  and  $\text{CoFe}_2\text{O}_4\text{-GSH}$  MNPs are approximately 9, 12 and 10 nm, respectively (from DLS measurements discussed below) while the Pcs have a size of  $\sim 1$  nm} it is unlikely for more than one MNP to be attached to the Pc, but it is possible for more than one Pc to link to the MNP. The number of Pc molecules bonded to the MNPs were determined following literature methods, but using absorption instead of fluorescence [148]. This involves comparing the Q band absorbance intensity of the Pc in the conjugate with that of the initial Pc before the conjugation. The ratio of Pcs:MNPs in the Pc-MNP conjugates reported in this thesis are listed in **Table 3.2**.

Complexes **1** and **2** were compared based on complex **2** being further away from the  $\text{CoFe}_2\text{O}_4$  centre than complex **1** due to the longer linkage chain. The ratio of Pcs:MNPs in **1**- $\text{CoFe}_2\text{O}_4$  is  $\sim 4:1$  and the ratio for **2**- $\text{CoFe}_2\text{O}_4\text{-COOH}$  is  $\sim 6:1$ . Thus, more complex **2** molecules (linked with a longer chain to the MNPs) can be accommodated onto MNPs than complex **1** with a shorter chain. The reason for this might be that the longer linkage chain in **2**- $\text{CoFe}_2\text{O}_4\text{-COOH}$  possibly prevents crowding of Pcs bonded to the MNPs hence more can be accommodated. In **1**- $\text{CoFe}_2\text{O}_4$  on the other hand there could be steric hinderance due to the Pcs being in closer proximity, preventing more Pcs from binding.

Complexes **3** and **5** have ester functional groups and cannot be conjugated to MNPs hence no loading data is shown for them. Complexes **4** and **6** were compared based on complex **4** having more carboxylic acid groups and hence possibly increased chances of amide bond formation with the  $\text{CoFe}_2\text{O}_4\text{-NH}_2$  MNPs than complex **6**. As shown in **Table 3.2**, the ratio of Pcs:MNPs in **4**- $\text{CoFe}_2\text{O}_4$  is  $\sim 4:1$  and  $\sim 7:1$  for **6**- $\text{CoFe}_2\text{O}_4$ . This is a possibly an indication that complex **4** forms more amide bonds with the  $\text{CoFe}_2\text{O}_4\text{-NH}_2$  MNPs and hence reduces the

number of conjugated Pcs. Comparison of these two conjugates (**4**-CoFe<sub>2</sub>O<sub>4</sub> and **6**-CoFe<sub>2</sub>O<sub>4</sub>) is not conclusive however because their conjugation to the MNPs was done following different procedures due to them being soluble in different solvents.

A similar comparison was made for complexes **2** and **7** where the latter has more amine groups and hence higher chances of increased amide bond formation with the CoFe<sub>2</sub>O<sub>4</sub>-GSH MNPs than the former. As shown in **Table 3.2**, the ratio of Pcs:MNPs in **2**-CoFe<sub>2</sub>O<sub>4</sub>-GSH is ~8:1 and ~5:1 for **7**-CoFe<sub>2</sub>O<sub>4</sub>. The obtained results agree with what was observed for complexes **4** and **6**. Complexes **2** and **7** were also used as examples to check the efficiency of covalently linking Pcs to MNPs compared to just mixing them by preparing composites (**2**-CoFe<sub>2</sub>O<sub>4</sub>-GSH (mix) and **7**-CoFe<sub>2</sub>O<sub>4</sub> (mix)) with no covalent bond. In terms of their Pc:MNP ratio, **2**-CoFe<sub>2</sub>O<sub>4</sub>-GSH (mix) was found to have a Pc:MNP ratio of ~9:1 and ~7:1 for **7**-CoFe<sub>2</sub>O<sub>4</sub> (mix). This is an indication that more Pcs are in the vicinity of the MNPs when there is no covalent interaction between them.

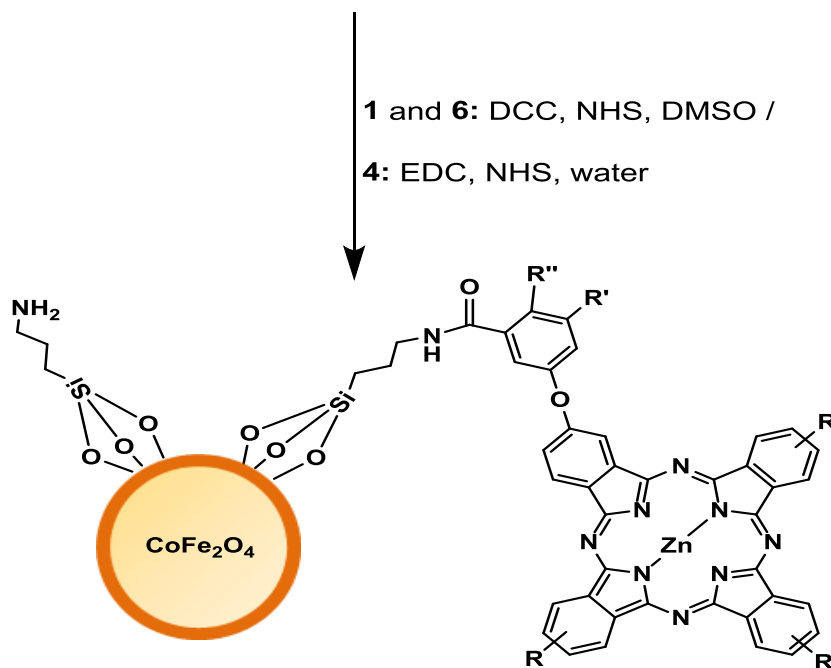
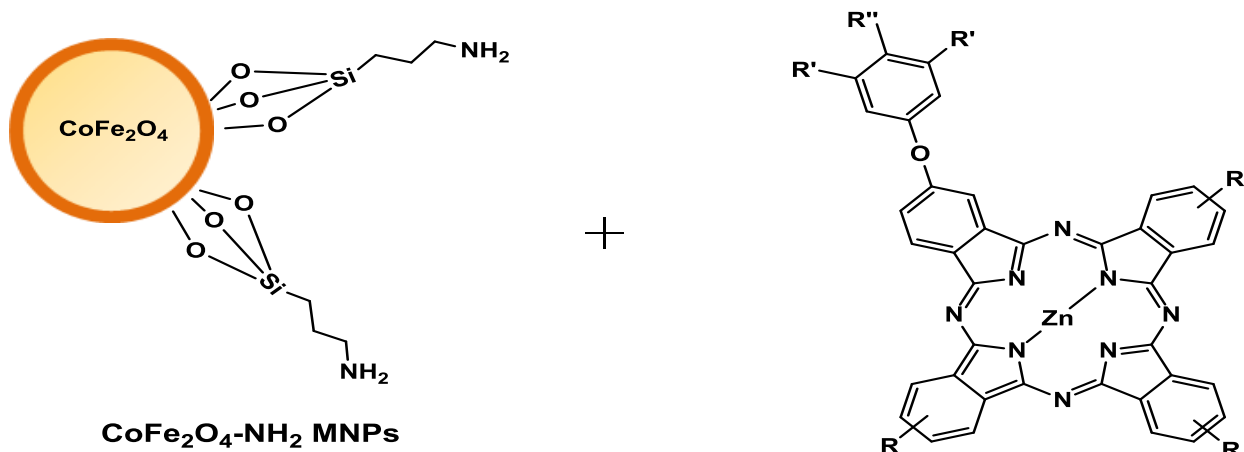
**Table 3.2:** Electronic absorption and other properties of Pc complexes **1-7**, CoFe<sub>2</sub>O<sub>4</sub> MNPs, and their respective Pc-MNP conjugates in DMSO (unless stated otherwise). Capping ligands are shown in denoting the conjugates of complex **2** for clarity since different ligands were employed.

Complex	Size (nm)			Pc Loading (Pc:MNP) <sup>a</sup>	$\lambda_{\text{abs}}$ <sup>b</sup>
	TEM	DLS	XRD		
<b>CoFe<sub>2</sub>O<sub>4</sub>-NH<sub>2</sub></b>	9.90	8.91	8.46	-	-
<b>1-CoFe<sub>2</sub>O<sub>4</sub></b>	14.78	14.11	14.56	4:1	678 (678)
<b>4-CoFe<sub>2</sub>O<sub>4</sub></b>	12.90	13.30	14.10	4:1	683 (683) <sup>c</sup>
<b>6-CoFe<sub>2</sub>O<sub>4</sub></b>	15.10	15.35	16.40	7:1	676 (676)
<b>CoFe<sub>2</sub>O<sub>4</sub>-COOH</b>	11.89	11.58	12.33	-	-
<b>2-CoFe<sub>2</sub>O<sub>4</sub>-COOH</b>	17.02	17.67	16.86	6:1	686 (686)
<b>CoFe<sub>2</sub>O<sub>4</sub>-GSH</b>	10.75	10.08	10.15	-	-
<b>2-CoFe<sub>2</sub>O<sub>4</sub>-GSH</b>	16.10	16.95	17.10	8:1 (9:1)	686 (686) 686
<b>7-CoFe<sub>2</sub>O<sub>4</sub></b>	14.95	14.05	14.78	5:1 (7:1)	689 (689) 689

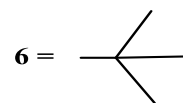
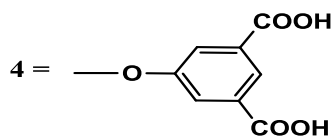
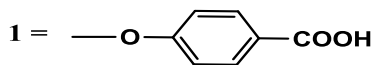
<sup>a</sup> values in brackets are for **2-CoFe<sub>2</sub>O<sub>4</sub>-GSH** (mix) and **7-CoFe<sub>2</sub>O<sub>4</sub>** (mix)

<sup>b</sup>  $\lambda_{\text{abs}}$  = Q band maxima absorption wavelength, values in brackets are for Pcs alone

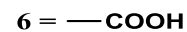
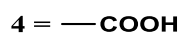
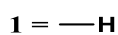
<sup>c</sup> values in water



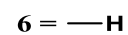
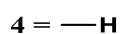
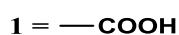
**R :**



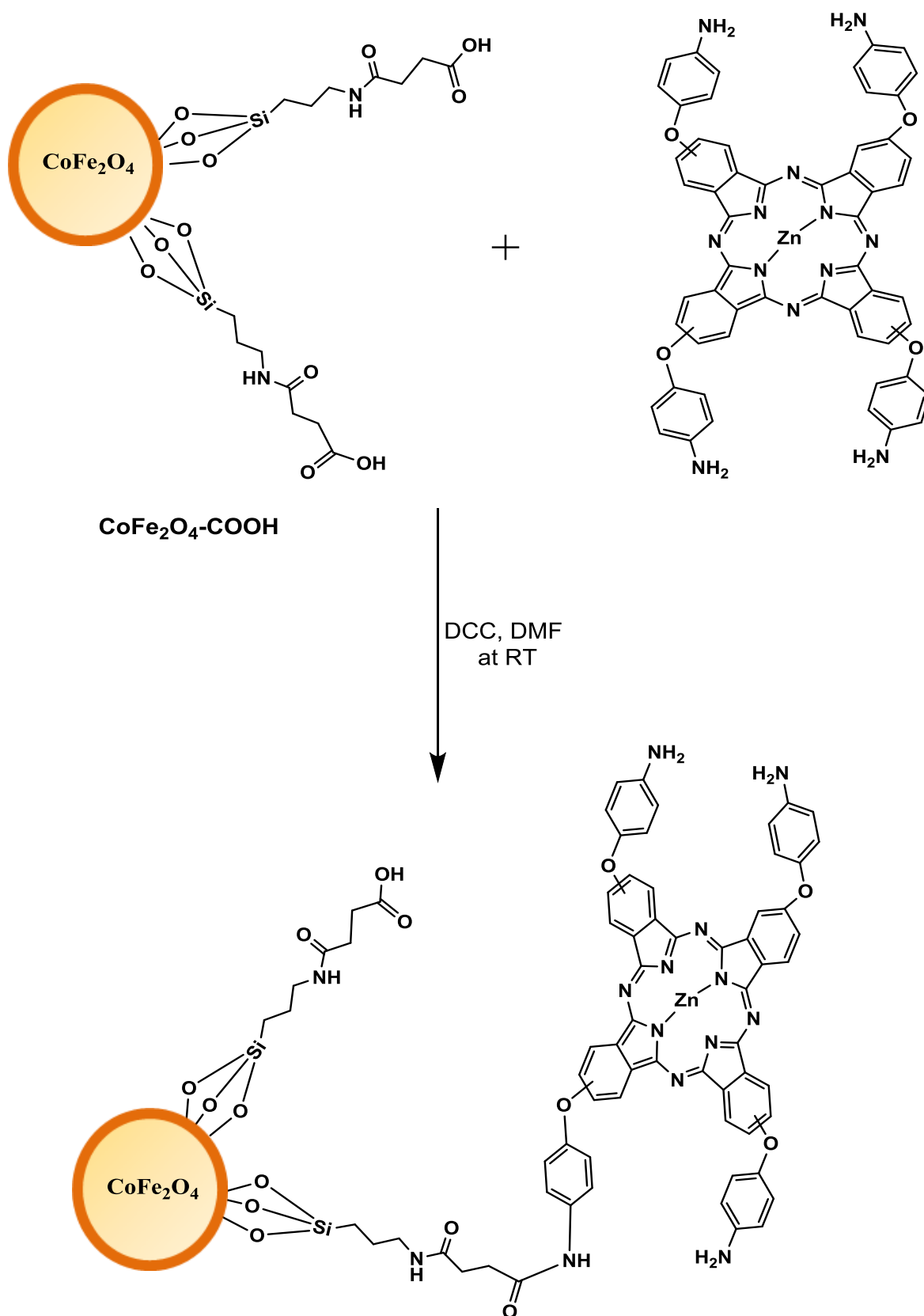
**R' :**



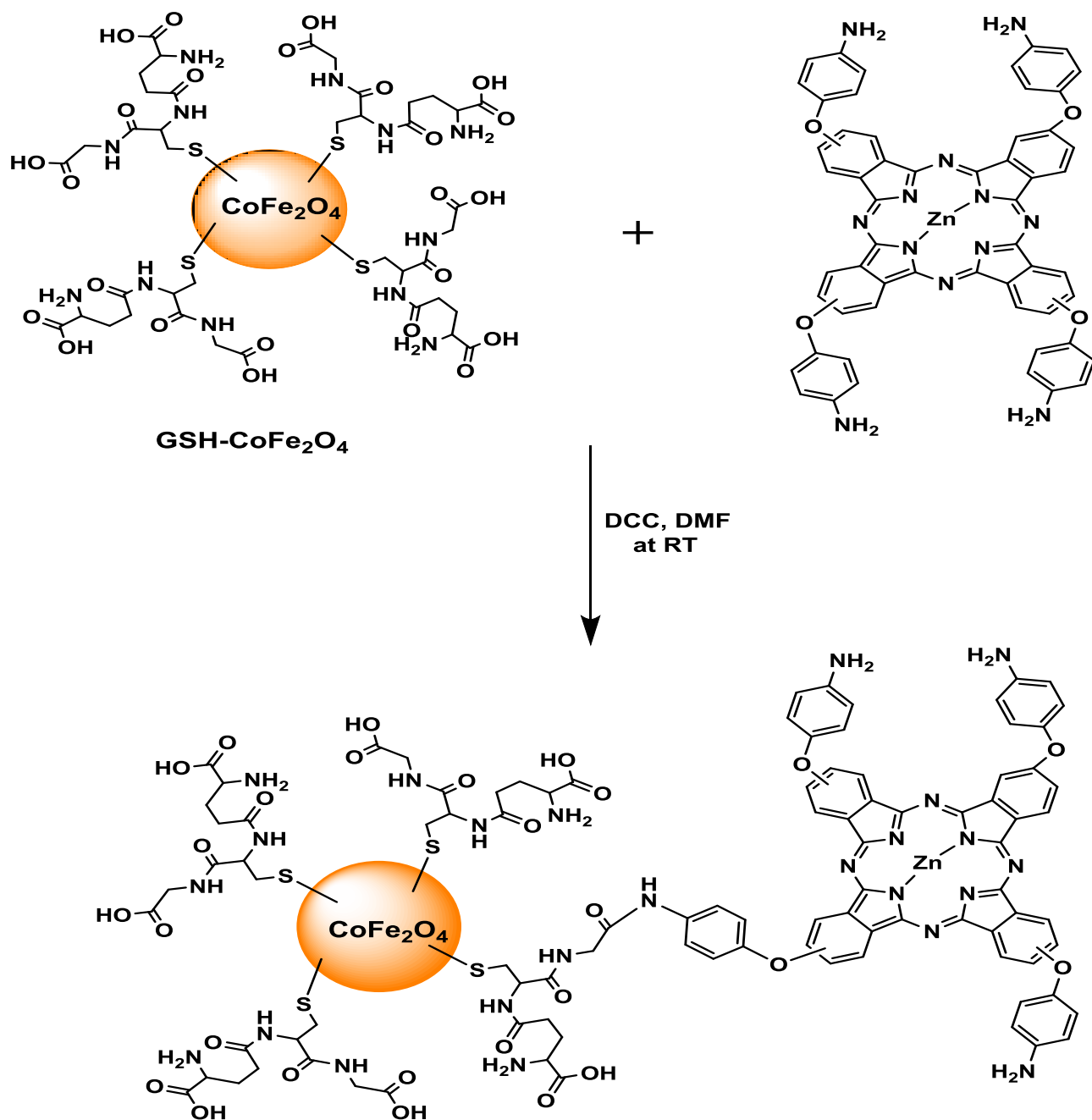
**R'' :**



**Scheme 3.4:** Conjugation of complexes **1**, **4** and **6** to  $\text{CoFe}_2\text{O}_4\text{-NH}_2$  MNPs.



**Scheme 3.5:** Conjugation of complex 2 to CoFe<sub>2</sub>O<sub>4</sub>-COOH MNPs.

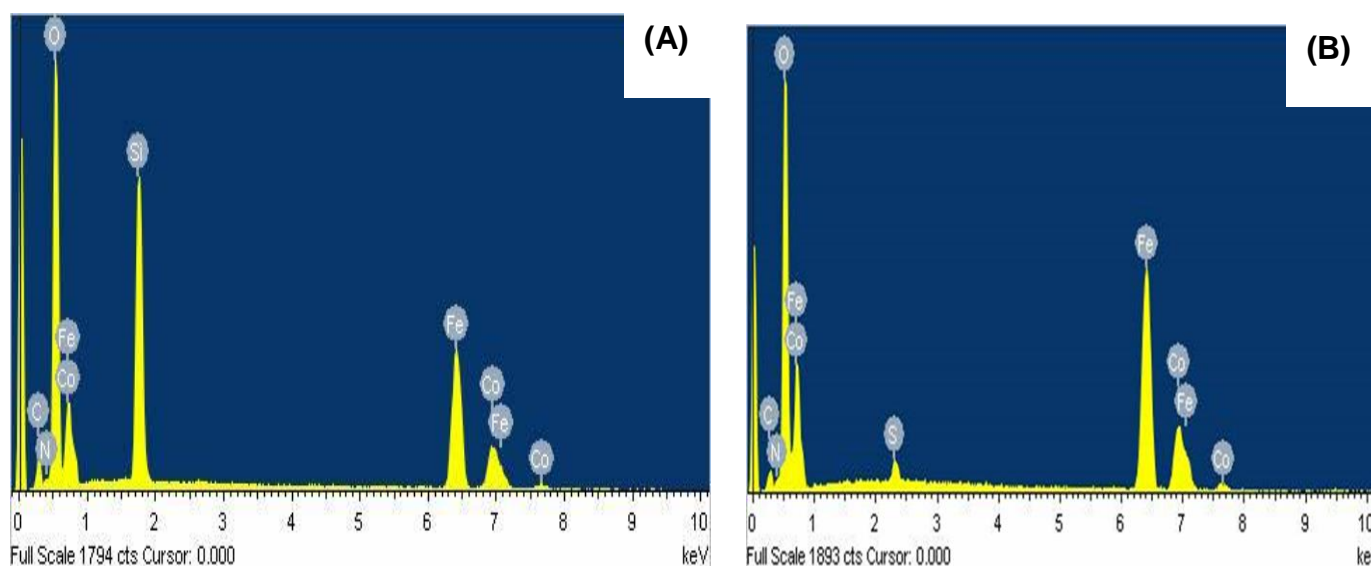


**Scheme 3.6:** Conjugation of complex **2** to  $\text{CoFe}_2\text{O}_4$ -GSH MNPs.

Characterisation techniques including Energy Dispersive X-ray Spectroscopy (EDS), Transmission Electron Microscopy (TEM), Dynamic Light Scattering (DLS), X-ray Diffraction (XRD) and X-ray Photoelectron Spectroscopy (XPS) were employed for confirmation of the synthesised  $\text{CoFe}_2\text{O}_4$  MNPs and  $\text{Pc-CoFe}_2\text{O}_4$  MNP conjugates.

### 3.2.2 Energy Dispersive X-ray Spectroscopy (EDS)

EDS was run so as to confirm the elemental composition of the  $\text{CoFe}_2\text{O}_4$  MNPs as well as their respective Pc-MNP conjugates (using complex **6** and **6-CoFe<sub>2</sub>O<sub>4</sub>** as examples) as shown in **Figure 3.3**. Since  $\text{CoFe}_2\text{O}_4\text{-NH}_2$  MNPs and  $\text{CoFe}_2\text{O}_4\text{-COOH}$  MNPs have the same elemental composition, only the spectrum of the  $\text{CoFe}_2\text{O}_4\text{-NH}_2$  MNPs is shown as an example (**Figure 3.3 (A)**). The EDS spectrum of the  $\text{CoFe}_2\text{O}_4\text{-GSH}$  MNPs on the other hand shows that the MNPs have a S peak from the glutathione and lack a Si peak which is present in the  $\text{CoFe}_2\text{O}_4\text{-NH}_2/\text{CoFe}_2\text{O}_4\text{-COOH}$  MNPs (from TEOS), confirming correct functionalization of each of the MNPs (**Figure 3.3 (B)**). All expected elements were obtained for complex **6** (**Figure 3.3 (C)**) and upon conjugation to the  $\text{CoFe}_2\text{O}_4\text{-NH}_2$  MNPs, there were additional peaks (Co, Fe and Si) which are from the MNPs (**Figure 3.3 (D)**). This is an indication that the conjugates are composites of both the Pcs and  $\text{CoFe}_2\text{O}_4\text{-NH}_2$  MNPs. Similar results were obtained for the other Pcs and their respective conjugates.





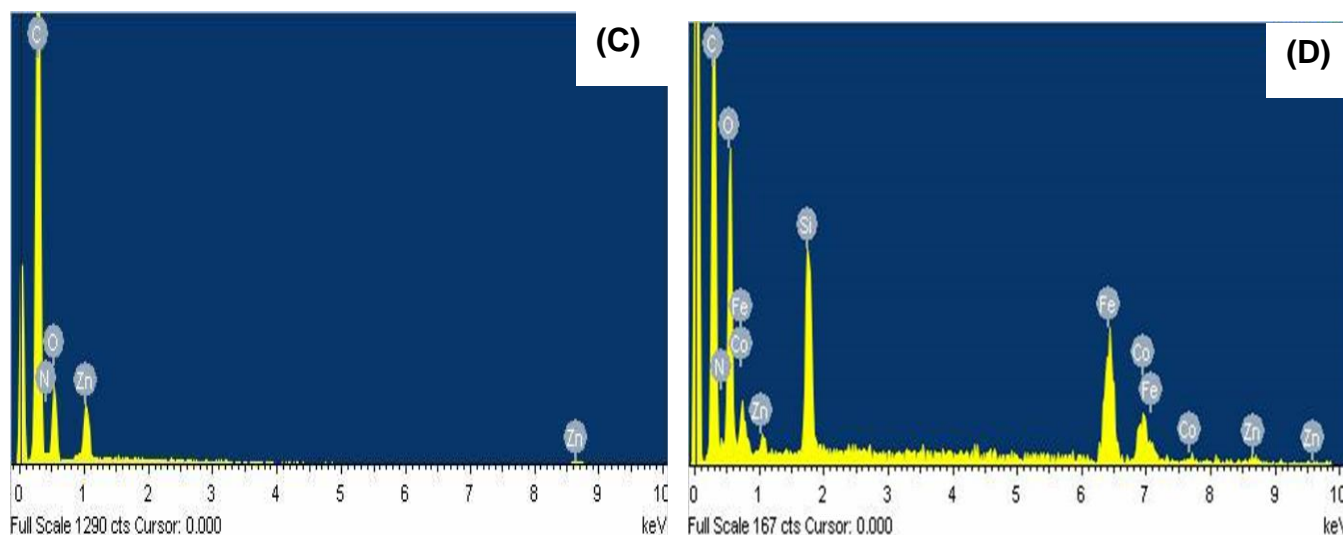


**Figure 3.3:** EDS spectra of: (A)  $\text{CoFe}_2\text{O}_4\text{-NH}_2$  MNPs and (B)  $\text{CoFe}_2\text{O}_4\text{-GSH}$  MNPs, (C) complex **6** and (D) **6**- $\text{CoFe}_2\text{O}_4$ .

### 3.2.3 Transmission Electron Microscopy (TEM)

TEM analyses were conducted for the  $\text{CoFe}_2\text{O}_4$  MNPs and their Pc-MNP conjugates (using  $\text{CoFe}_2\text{O}_4\text{-NH}_2$  and **1**- $\text{CoFe}_2\text{O}_4$  as examples) so to determine their sizes, morphology and dispersion. As shown in **Figure 3.4**, the TEM images show that the MNPs are aggregated, possibly due to their superparamagnetic nature and hence their strong magnetic attraction. In the case of **1**- $\text{CoFe}_2\text{O}_4$ , aggregation is not just attributed to magnetic attractions between the MNPs but also possible  $\pi\text{-}\pi$  interactions between Pcs on neighbouring MNPs. The images revealed that the MNPs and their conjugates are mostly spherical with sizes of 9.90 and 14.78 nm for  $\text{CoFe}_2\text{O}_4\text{-NH}_2$  and **1**- $\text{CoFe}_2\text{O}_4$ , respectively (**Figure 3.4**). The sizes of the MNPs and the Pc-MNP conjugates reported in this thesis are listed in **Table 3.2**. The results show that functionalization of the MNPs as well as their conjugation to Pcs causes increase in their sizes.

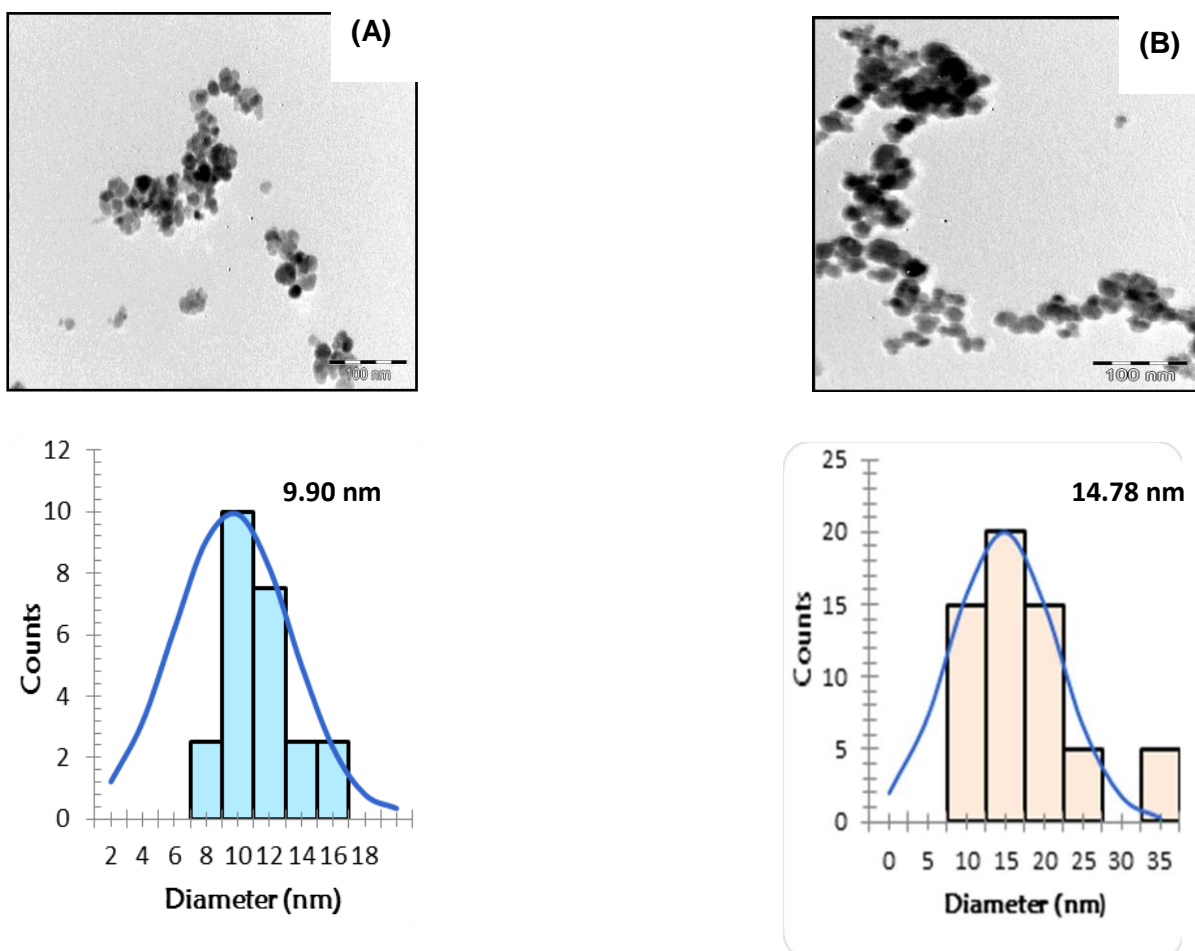


**Figure 3.4:** TEM images of: (A) CoFe<sub>2</sub>O<sub>4</sub>-NH<sub>2</sub> MNPs, (B) 1-CoFe<sub>2</sub>O<sub>4</sub>- their corresponding histograms (showing size distribution).

### 3.2.4 Dynamic Light Scattering (DLS)

Due to the aggregation on the TEM images of the CoFe<sub>2</sub>O<sub>4</sub> MNPs, size distribution of the MNPs and their conjugates was confirmed using DLS techniques. The sizes obtained for the CoFe<sub>2</sub>O<sub>4</sub>-NH<sub>2</sub> MNPs and 1-CoFe<sub>2</sub>O<sub>4</sub> are 8.91 and 14.11 nm, respectively (**Figure 3.5**). The sizes of the other MNPs and conjugates obtained from DLS measurements are listed in **Table 3.2**. Just as with TEM, there was an observed increase in sizes of the MNPs upon conjugation

to Pcs and as shown in **Table 3.2**, the DLS graphs of all the MNPs and their conjugates show sizes comparable to those obtained from TEM.

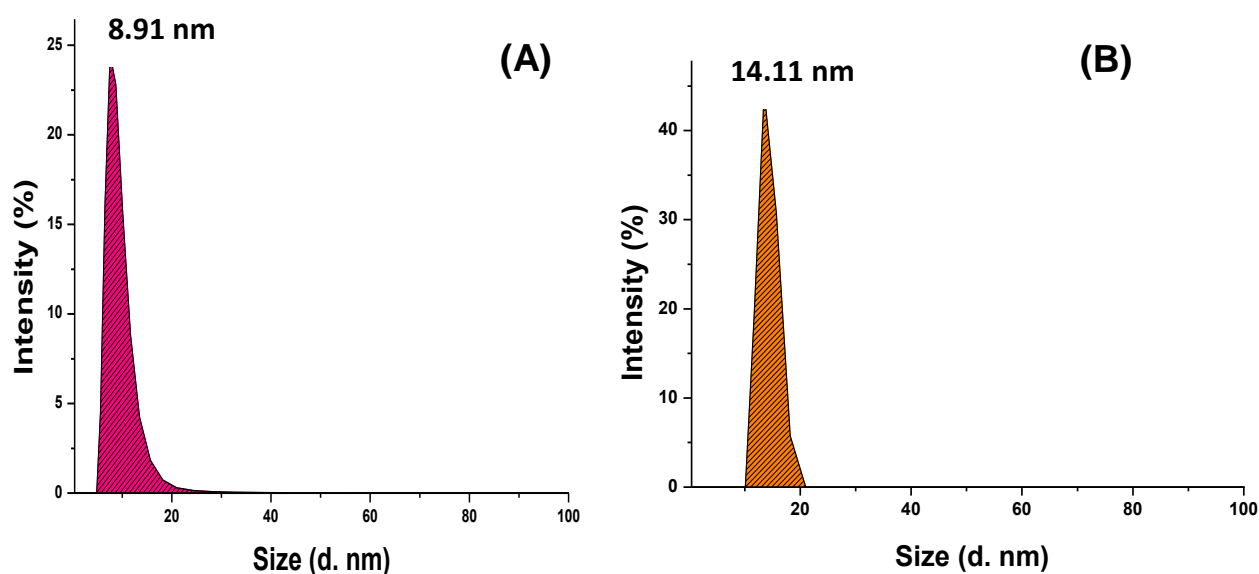


**Figure 3.5:** DLS graphs of (A) CoFe<sub>2</sub>O<sub>4</sub>-NH<sub>2</sub> MNPs, (B) 1-CoFe<sub>2</sub>O<sub>4</sub>.

### 3.2.5 X-ray Diffraction (XRD)

The XRD patterns of the Pcs, CoFe<sub>2</sub>O<sub>4</sub> MNPs and their respective conjugates were analysed and compared as shown in **Figure 3.6** (using CoFe<sub>2</sub>O<sub>4</sub>-NH<sub>2</sub> MNPs, 1-CoFe<sub>2</sub>O<sub>4</sub> and complex **1** as examples). The CoFe<sub>2</sub>O<sub>4</sub>-NH<sub>2</sub> MNPs show characteristic peaks attributed to a cubic spinel structure with peaks at  $2\theta = 30^\circ, 35^\circ, 37^\circ, 43^\circ, 54^\circ, 57^\circ$  and  $63^\circ$  corresponding to hkl Miller indices of (220), (311), (222), (400), (422), (511) and (440), respectively. These characteristic peaks agree with the values which have been reported in literature before [135]. Complex **1** on the other hand has a broadened peak at  $\sim 2\theta=26^\circ$  which is typical for Pcs [149] while 1-CoFe<sub>2</sub>O<sub>4</sub> has peaks corresponding to both complex **1** and CoFe<sub>2</sub>O<sub>4</sub>-NH<sub>2</sub> MNPs. This is an indication that the conjugate is indeed a composite of the two photocatalysts and that the

CoFe<sub>2</sub>O<sub>4</sub>-NH<sub>2</sub> MNPs retain their crystallinity when conjugated to Pcs which also retain their amorphous nature in the conjugate. Similar diffraction patterns were obtained for the rest of the Pcs and their respective Pc-MNP conjugates.

XRD was also used to again determine the sizes of the MNPs and Pc-MNP conjugates for comparison using the Debye–Scherrer equation (**Equation 3.1**) [150]:

$$d = \frac{k\lambda}{\beta \cos \theta} \quad (3.1)$$

where  $\lambda$  is the wavelength of the X-ray source (1.5405 Å),  $k$  is an empirical constant equal to 0.9,  $\beta$  is the full width at half maximum of the diffraction peak and  $\theta$  is the angular position.

The calculated crystal sizes were found focusing on the (311) peak wherein the CoFe<sub>2</sub>O<sub>4</sub>-NH<sub>2</sub> MNPs and **1**-CoFe<sub>2</sub>O<sub>4</sub> were found have sizes of 8.46 and 14.65 nm, respectively. The sizes of the rest of the MNs and conjugates are listed in **Table 3.2** and were found to be close to those obtained in TEM and DLS.

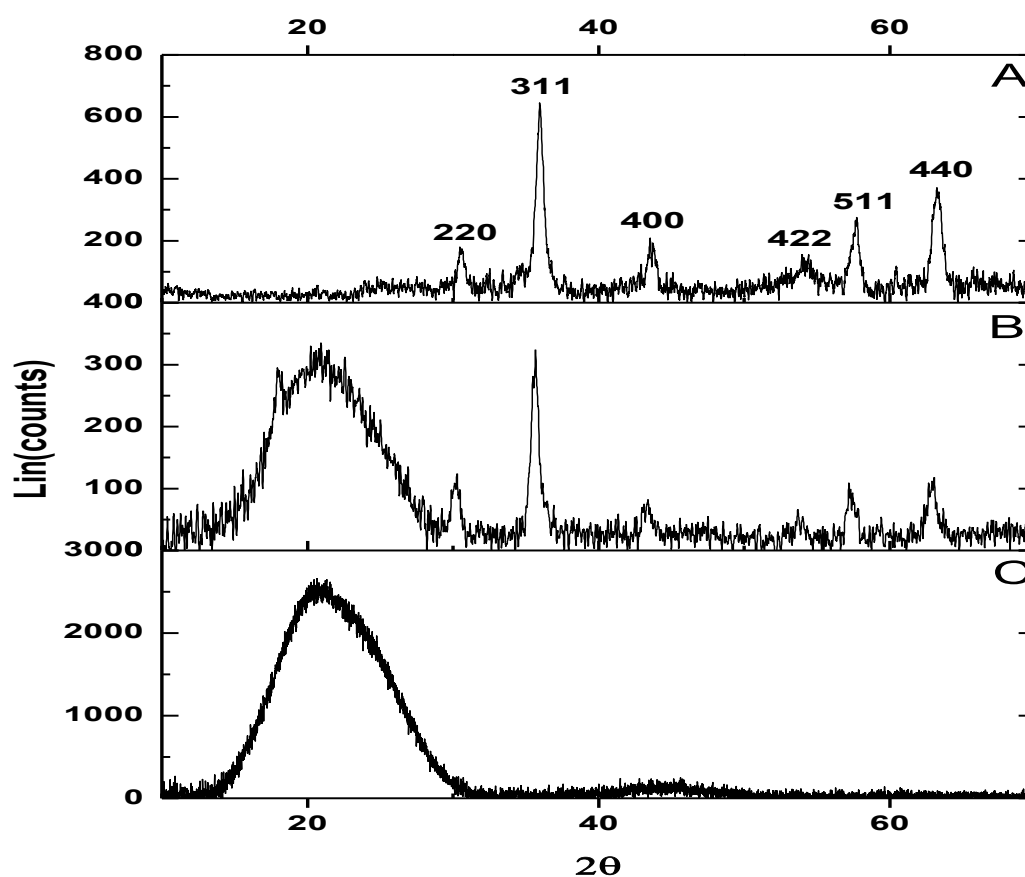


**Figure 3.6:** XRD diffraction pattern of (A)  $\text{CoFe}_2\text{O}_4\text{-NH}_2$  MNPs, (B) **1**- $\text{CoFe}_2\text{O}_4$  and (C) complex **1**.

### 3.2.6 X-ray Photoelectron Spectroscopy (XPS)

X-ray photoelectron spectroscopy (XPS) was used to analyse the surface chemistry of the  $\text{CoFe}_2\text{O}_4$  MNPs and to confirm their functionalisations. Wide scan XPS analyses were conducted for the Pc complexes,  $\text{CoFe}_2\text{O}_4$  MNPs and Pc-MNP conjugates. Since complexes **1**, **2**, **4** and **6** have the same elemental composition and the MNPs ( $\text{CoFe}_2\text{O}_4\text{-NH}_2$  and  $\text{CoFe}_2\text{O}_4\text{-COOH}$ ) also have the same elemental composition, survey spectra for **1**,  $\text{CoFe}_2\text{O}_4\text{-NH}_2$  and **1**- $\text{CoFe}_2\text{O}_4$  are shown in **Figure 3.7** as examples. The spectra show the expected

elements for all the compounds with **1**-CoFe<sub>2</sub>O<sub>4</sub> showing elements attributed to both the Pc and MNPs, an indication of purity and that it is a composite of the two.

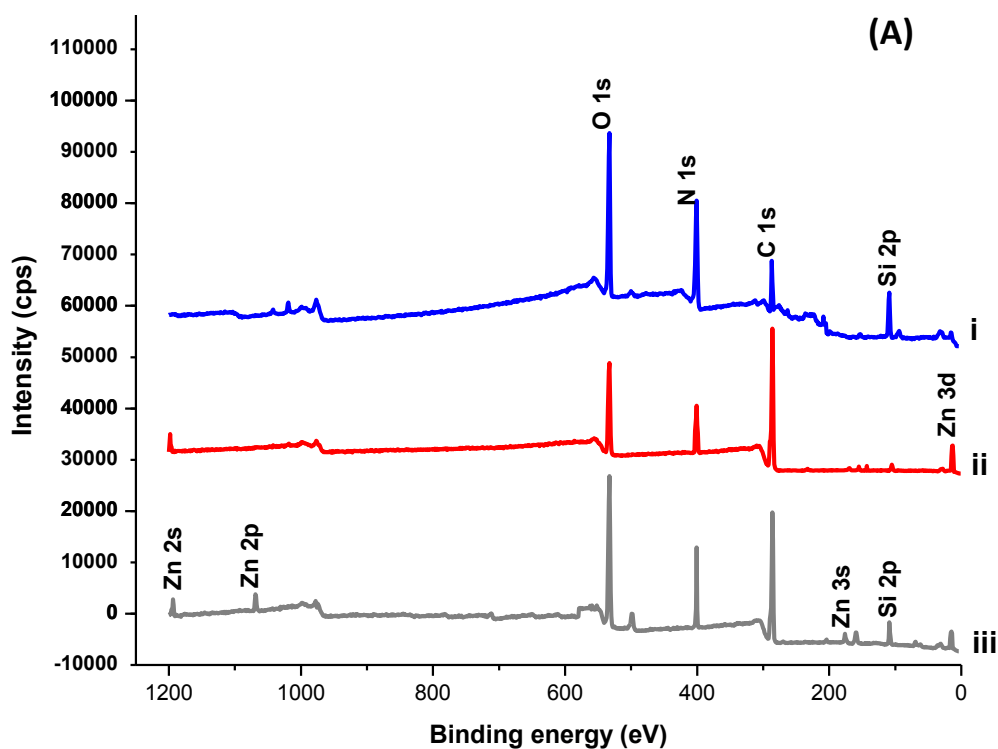
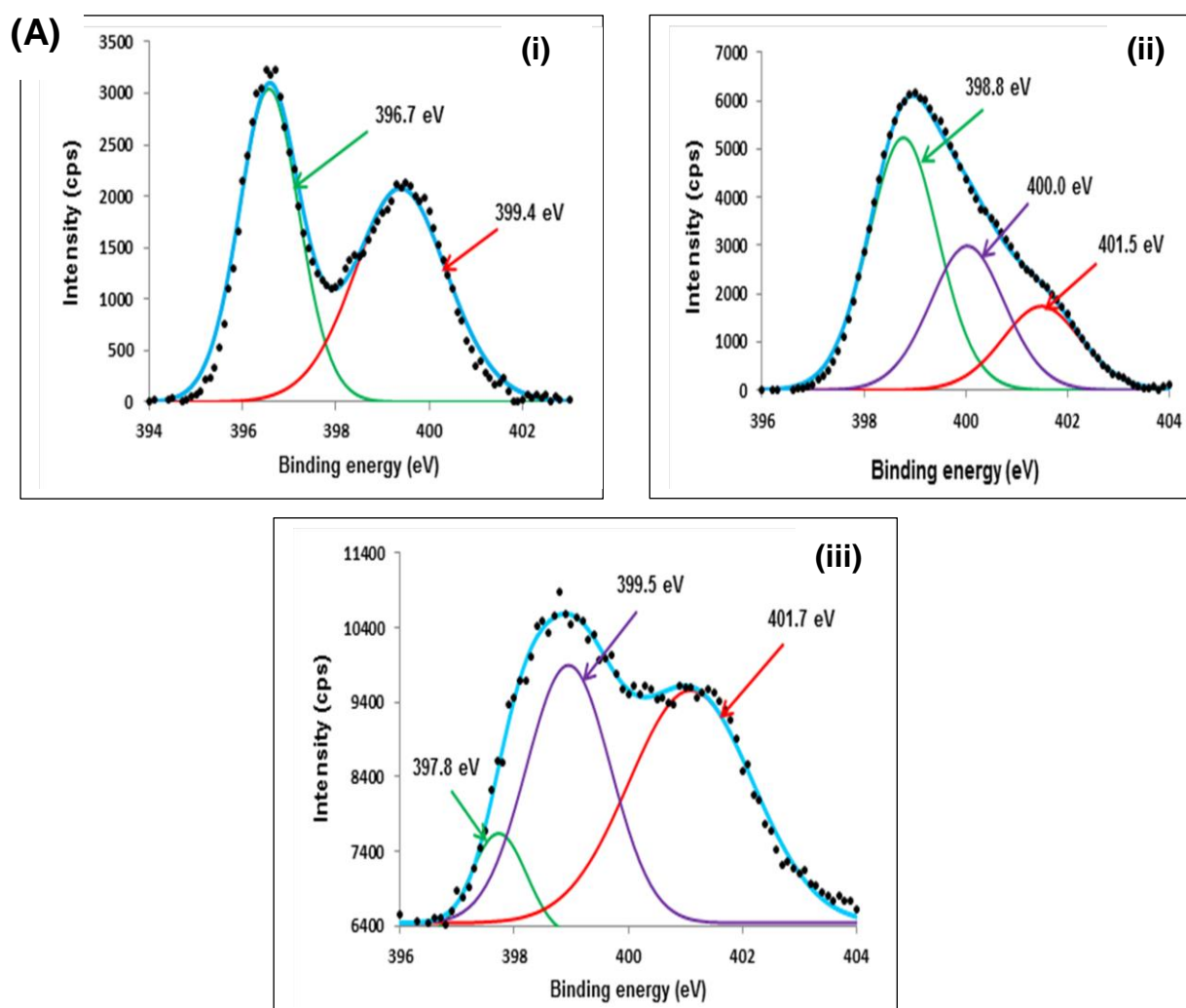


**Figure 3.7:** (A) Wide scan XPS spectra for (i) CoFe<sub>2</sub>O<sub>4</sub>-NH<sub>2</sub>, (ii) complex **1** and (iii) **1**-CoFe<sub>2</sub>O<sub>4</sub>.

High resolution XPS analysis was taken so as to prove efficient functionalization of the MNPs. The N 1s high resolution peak for the CoFe<sub>2</sub>O<sub>4</sub>-NH<sub>2</sub> MNPs was deconvoluted to yield two components at 396.7 eV (N-C) and 399.4 eV (N-H) (**Figure 3.8 A (i)**). The N 1s high resolution peak for the CoFe<sub>2</sub>O<sub>4</sub>-COOH MNPs on the other hand was deconvoluted to three components at 398.8 eV, 400.0 eV, and 401.5 eV corresponding to N-C, N-H and N-C=O respectively (**Figure 3.8 A (ii)**). The component at high binding energy (401.5 eV) is representative of the amide bond formation between the CoFe<sub>2</sub>O<sub>4</sub>-NH<sub>2</sub> MNPs and succinic

anhydride and is not present in the  $\text{CoFe}_2\text{O}_4\text{-NH}_2$  alone. This is an indication of efficient functionalization of the  $\text{CoFe}_2\text{O}_4\text{-NH}_2$  to form  $\text{CoFe}_2\text{O}_4\text{-COOH}$  MNPs.

The N 1s high resolution peak for the  $\text{CoFe}_2\text{O}_4\text{-GSH}$  MNPs was deconvoluted to yield three components at 397.8 eV, 399.5 eV, and 401.7 eV corresponding to N-C, N-H and N-C=O, respectively (**Figure 3.8 A (iii)**). The component at high binding energy (401.7 eV) is representative of the amide bonds present in the glutathione backbone. The obtained results are therefore an indication of efficient functionalization of all three MNPs.



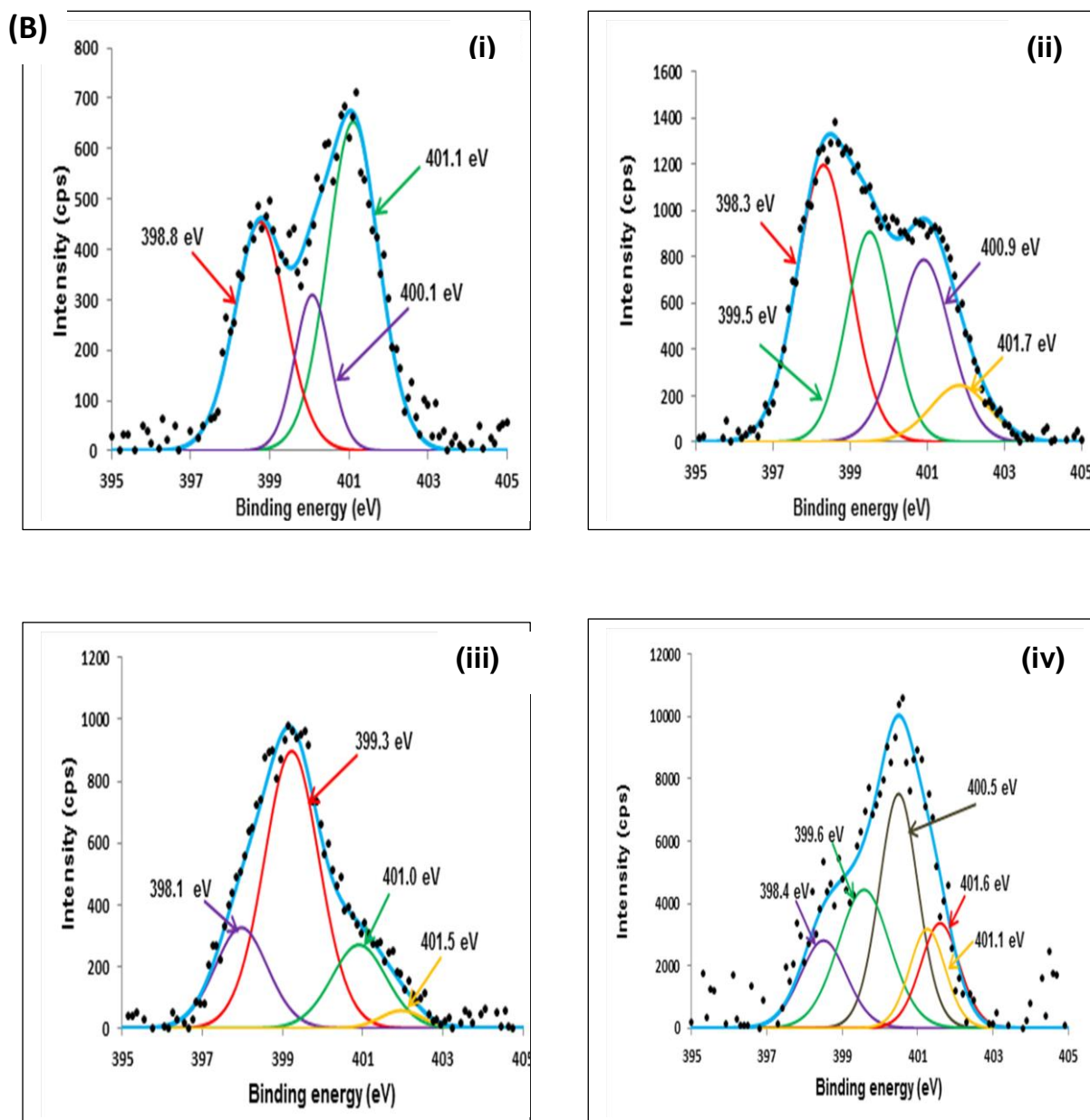


**Figure 3.8:** High resolution XPS (N 1s) spectra for (A) (i)  $\text{CoFe}_2\text{O}_4\text{-NH}_2$  MNPs, (ii)  $\text{CoFe}_2\text{O}_4\text{-COOH}$ , (iii)  $\text{CoFe}_2\text{O}_4\text{-GSH}$  and (B) (i) complex **1**, (ii) **1**- $\text{CoFe}_2\text{O}_4$ , (iii) complex **2** and (iv) **2**- $\text{CoFe}_2\text{O}_4\text{-COOH}$ .

High resolution XPS analysis was also taken so as to prove amide bond linkage between the MNPs and Pcs. The XPS results obtained for the linkage of complex **1** and the  $\text{CoFe}_2\text{O}_4\text{-NH}_2$  MNPs to form **1**- $\text{CoFe}_2\text{O}_4$  as well as between complex **2** and the  $\text{CoFe}_2\text{O}_4\text{-COOH}$  MNPs



resulting in **2-CoFe<sub>2</sub>O<sub>4</sub>-COOH** are shown as examples. The high resolution N 1s for complex **1** was deconvoluted to three components: 398.8 eV (N=C), 400.1 eV (N) and 401.1 eV (N-C) (**Figure 3.8 B(i)**) while that of **1-CoFe<sub>2</sub>O<sub>4</sub>** was deconvoluted to four components at 398.3 eV (N=C), 399.5 eV (N), 400.9 eV (N-C) and 401.7 eV (N-C=O) (**Figure 3.8 B (ii)**). The presence of the high binding energy component (401.7 eV) in **1-CoFe<sub>2</sub>O<sub>4</sub>** is in indication that there was bond formation between complex **1** and **CoFe<sub>2</sub>O<sub>4</sub>-NH<sub>2</sub>**, since it is absent in **CoFe<sub>2</sub>O<sub>4</sub>-NH<sub>2</sub>** (**Fig. 3.8 A (i)**) and in complex **1** (**Figure 3.8 B(i)**).

The high resolution N 1s for complex **2** on the other hand was deconvoluted to show four components at 398.1 eV (N=C), 399.3 eV (N), 401.0 eV (N-C) and 401.5 eV (N-H) (**Figure 3.8 B (iii)**). The high resolution N 1s for **2-CoFe<sub>2</sub>O<sub>4</sub>-COOH** was deconvoluted and showed five components at 398.4 eV (N=C), 399.6 eV (N), 400.5 eV (N-C), 401.1 eV (N-H) and 401.6 eV (N-C=O), **Figure 3.8 B (iv)**. The intensity of the higher binding energy component (401.6 eV) is higher at 3373 cps for the conjugate compared to **CoFe<sub>2</sub>O<sub>4</sub>-COOH** (**Figure 3.8 (B)**) alone at 1746 cps. This may be an indication of an increase in amide bonds in **2-CoFe<sub>2</sub>O<sub>4</sub>** compared to the **CoFe<sub>2</sub>O<sub>4</sub>-COOH** MNPs which also have amide bonds. The increase in amide bonds within the conjugate therefore suggests that complex **2** and **CoFe<sub>2</sub>O<sub>4</sub>-COOH** were covalently linked through amide bond formation.

Similar results were obtained for complexes **4**, **6** and **7** and their respective conjugates. In addition to confirming amide bond formation, estimates on which Pc-MNP conjugates had more amide bonds were performed. In the case of complexes **4** and **6** for instance (which differ based on the former having 8 carboxylic groups and the latter having 2), comparison of the intensities of their high binding component (representative of the amide bond) shows that **6-CoFe<sub>2</sub>O<sub>4</sub>** has lower intensity of 146 cps compared to **4-CoFe<sub>2</sub>O<sub>4</sub>** with an intensity of 1603 cps. This could therefore be an indication that there are more amide bonds between complex **4** and the **CoFe<sub>2</sub>O<sub>4</sub>-NH<sub>2</sub>** MNPs than those between complex **6** and the **CoFe<sub>2</sub>O<sub>4</sub>-NH<sub>2</sub>** MNPs,

possibly due to the presence of more COOH groups in complex **4**. A similar comparison was made between complexes **2** and **7** which differ based on the former having 4 amine groups and the latter having 8. The intensities of the higher binding energy components (401.2 eV) were found to be 14620 and 11730 cps for **2**-CoFe<sub>2</sub>O<sub>4</sub>-GSH and **7**-CoFe<sub>2</sub>O<sub>4</sub> respectively. The results in this case show that even though complex **7** has 8 terminal amine groups, it forms less covalent bonds (less intensity of the amide bond peak) than complex **2**. This could be attributed to factors such steric hinderance due to the multiple sites of attachment and hence various ways that the complex **7** and GSH-CoFe<sub>2</sub>O<sub>4</sub> MNPs can bond.

### 3.2.7 Thermal Analyses

Thermal analyses of the Pcs, CoFe<sub>2</sub>O<sub>4</sub> MNPs and their respective conjugates were conducted (**Figure 3.9**) and similar results were obtained hence just complex **1**, CoFe<sub>2</sub>O<sub>4</sub>-NH<sub>2</sub> MNPs and their conjugate; **1**-CoFe<sub>2</sub>O<sub>4</sub> are shown as examples. Complex **1** was observed to exhibit the highest thermal stability and the CoFe<sub>2</sub>O<sub>4</sub>-NH<sub>2</sub> MNPs showed the least stability. The conjugate (**1**-CoFe<sub>2</sub>O<sub>4</sub>) showed thermal stability between that of the Pc and MNP, an indication that it is a composite of both compounds and has inherent propertied from both photocatalysts.

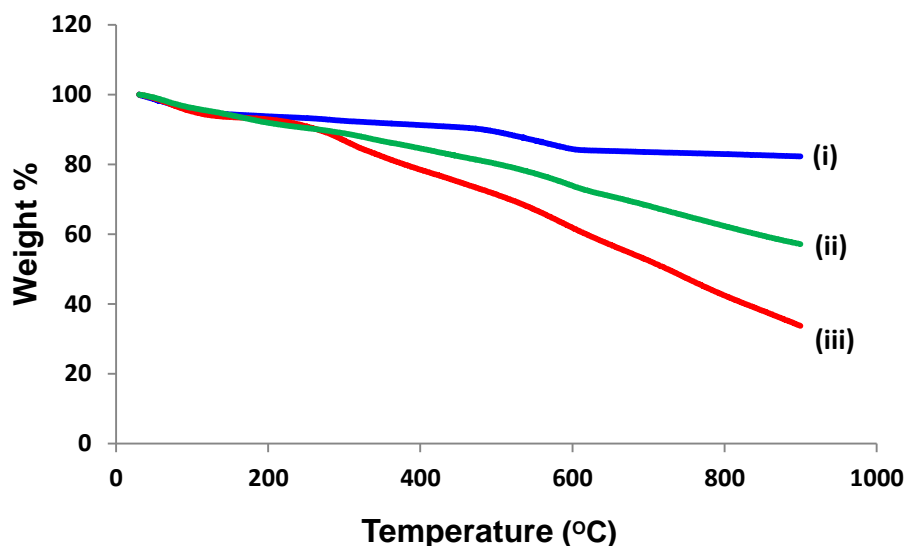


**Figure 3.9:** TGA thermograms of (i) complex **1**, (ii) **1**-CoFe<sub>2</sub>O<sub>4</sub> and (iii) CoFe<sub>2</sub>O<sub>4</sub>-NH<sub>2</sub> MNPs.

### 3.2.8 UV-vis spectroscopy

Comparison of the UV-Vis spectra of the Pcs and their respective Pc-MNP conjugates are shown in **Figure 3.10** (using complexes **4** and **6** as well as their respective conjugates as examples). The spectra reveal that there are no observed shifts in the Q bands of both Pcs after conjugation (**Table 3.2**). There is increase in the absorption of the B band (ultraviolet region) of the Pcs after conjugation. This is not surprising as that is the region in which the CoFe<sub>2</sub>O<sub>4</sub>-NH<sub>2</sub> MNPs absorb (**Figure 3.10 (B)** (insert)). The lack of shift in the Q band shows that the Pc complexes remain intact following conjugation to MNPs. In the case of complex **4**, the broadening and split of the Pc Q band even after conjugation to the MNPs suggests that its aggregation is maintained even when conjugated to CoFe<sub>2</sub>O<sub>4</sub>-NH<sub>2</sub> MNPs. Similar spectra were observed for the other Pc and their respective conjugates.

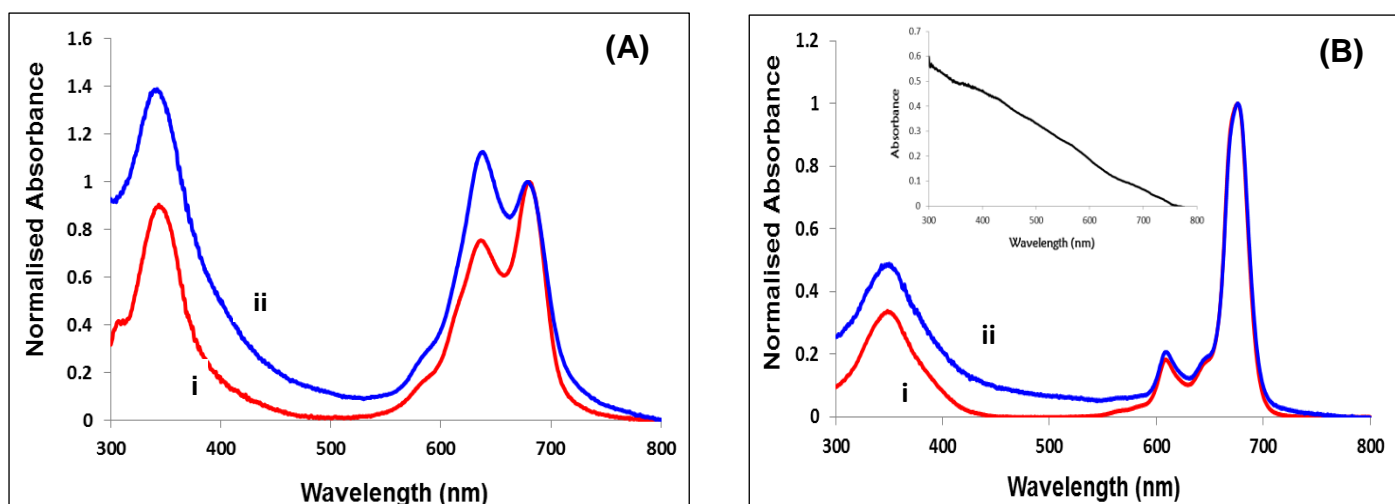


**Figure 3.10:** UV-vis absorption spectra of: (A) i. complex **4**, ii. **4**-CoFe<sub>2</sub>O<sub>4</sub> and (B) i. complex **6**, (ii) **6**-CoFe<sub>2</sub>O<sub>4</sub> in DMSO. Insert= Spectrum of CoFe<sub>2</sub>O<sub>4</sub>-NH<sub>2</sub> MNPs.

The emission, excitation and absorption spectra of the novel Pc's conjugate (**6**-CoFe<sub>2</sub>O<sub>4</sub>) are shown in **Figure 3.11** (as an example). The emission spectra were observed to be mirror images of the excitation spectra while the latter are similar to the absorption spectra, an indication of non-aggregation of the Pc complexes in solution.

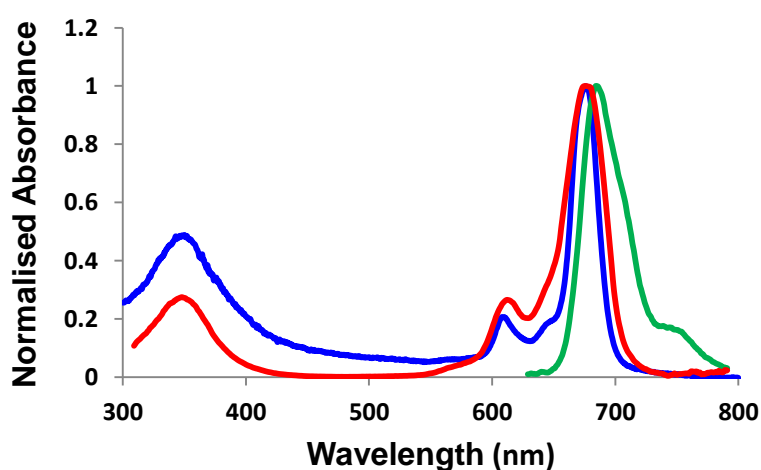


**Figure 3.11:** Normalized absorbance (blue), excitation (red) and emission (green) spectra of **6**-CoFe<sub>2</sub>O<sub>4</sub> in DMSO.

### **3.3 Closing Remarks**

Zinc Pcs, various  $\text{CoFe}_2\text{O}_4$  MNPs and their respective Pc-MNP conjugates were successfully synthesized and characterized by various microscopic and spectroscopic techniques. All the compounds and composites gave data indicating high purity and in accordance with the predicted structures. Successful conjugation between the Pcs and MNPs was achieved and the effect of the interaction on their photochemical and photophysical properties is discussed next.

# CHAPTER 4

## Results and Discussion

## 4. Photophysicochemical properties of phthalocyanines and Pc-MNP conjugates

This chapter reports on the photophysicochemical properties of Pcs and how these properties are affected when they are conjugated to CoFe<sub>2</sub>O<sub>4</sub> MNPs.

### 4.1 Fluorescence Quantum Yields ( $\Phi_F$ ) and Lifetimes ( $\tau_F$ )

Fluorescence quantum yields were determined for the Pcs and their respective Pc-MNP conjugates using the comparative method. Upon conjugation of Pcs to MNPs, the heavy atom effect introduced by the MNPs enhances intersystem crossing (ISC) of the Pc and minimises chances of fluorescence occurring. Lower fluorescence quantum yields are therefore expected for Pc-MNP conjugates compared to their respective Pcs.

Complexes **1** and **2** (which were compared based on enhancement of their photophysics due to them having different linkage chain lengths and hence separation from the MNP centre) have been reported to have fluorescence quantum yields of 0.1 [58] and 0.06 [60], respectively. Upon the conjugation of the Pcs (**1** and **2**) to CoFe<sub>2</sub>O<sub>4</sub>-NH<sub>2</sub> and CoFe<sub>2</sub>O<sub>4</sub>-COOH MNPs respectively, to form **1**-CoFe<sub>2</sub>O<sub>4</sub> and **2**-CoFe<sub>2</sub>O<sub>4</sub>-COOH, fluorescence quantum yields below 0.01 were obtained (**Table 4.1**). The fluorescence decay curves of the photocatalysts are shown in **Figure 4.1** (using complex **1** and **1**-CoFe<sub>2</sub>O<sub>4</sub> as examples) and they show biexponential decays. This type of decay may occur for Pcs due to the formation of aggregates which are non-fluorescent, but which can quench the monomer [151]. For the Pc-MNP conjugates, the bi-exponential fluorescence lifetimes could be due to the orientation of the Pcs around the MNPs [152]. Fluorescence lifetimes for Pcs are generally short and highly dependent on the nature of the central metal ion and substituents on the Pc. The

obtained fluorescence lifetimes for complex **1** and **1-CoFe<sub>2</sub>O<sub>4</sub>** are 3.00 [58] and 2.89 ns, respectively while those for complex **2** and **2-CoFe<sub>2</sub>O<sub>4</sub>-COOH** are 2.79 [60] and 2.60 ns, respectively. The shortening in fluorescence lifetimes corresponds to the decrease in fluorescence quantum yields.

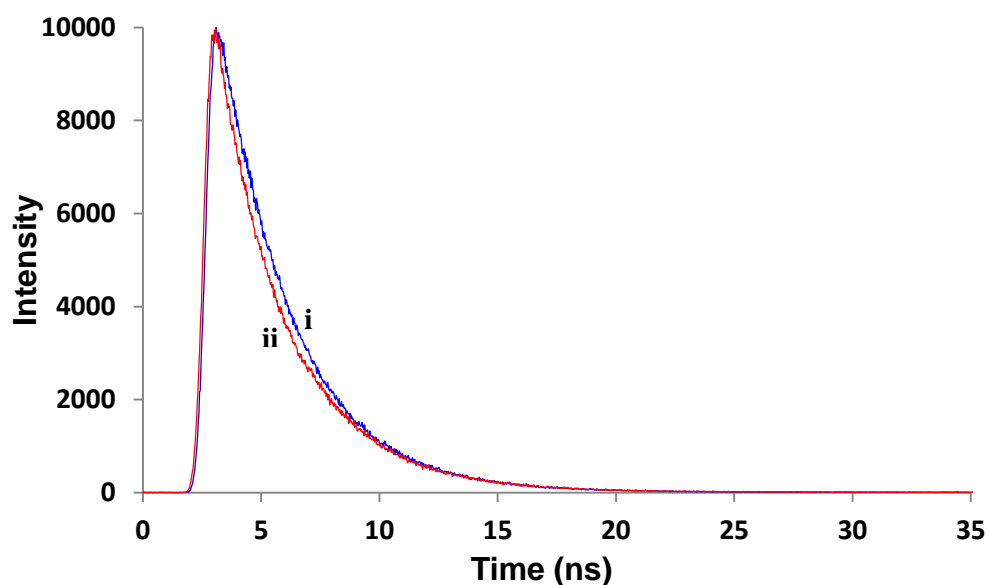


**Figure 4.1:** Fluorescence lifetime decay curve of (i) **1** and (ii) **1-CoFe<sub>2</sub>O<sub>4</sub>** conjugate in DMSO where  $\lambda_{exc} = 619$  nm.

The fluorescence quantum yields of Pc complexes **3** and **5** are reported herein for the first time wherein the Pcs are compared based on the former being symmetrical and the latter being unsymmetrical. Complexes **3** and **5** were found to have fluorescence quantum yields of 0.067 and 0.055, respectively and fluorescence lifetimes of 9.07 and 6.16 ns, respectively (**Table 4.1**).

Complexes **4** and **6** were also compared based on the former being symmetrical and the latter being unsymmetrical and them having different number of carboxylic acid groups for amide bond formation with the **CoFe<sub>2</sub>O<sub>4</sub>-NH<sub>2</sub>** MNPs. Complex **6** and its conjugate (**6-CoFe<sub>2</sub>O<sub>4</sub>**)



were found to have fluorescence quantum yields of 0.14 and 0.078 respectively and fluorescence lifetimes of 7.60 and 3.14 ns respectively. However, there were no fluorescence values for complex **4** and its conjugate (**4**-CoFe<sub>2</sub>O<sub>4</sub>) due to their aggregation in water. The presence of aggregates has been reported to decrease quantum yields through the conversion of electronic excitation energy of fluorophores to vibrational energy [153].

Complexes **2** and **7** were compared based on them having different number of amine groups available for amide bond formation. The effect of amide bond formation or just mixing Pcs to MNPs (no covalent bond) on the photophysical properties of Pcs was also evaluated. As mentioned above, complex **2** has a fluorescence quantum yield of 0.06 [60] and that of complex **7** is 0.11 [63]. Upon amide bond linkage of the Pc complexes with CoFe<sub>2</sub>O<sub>4</sub>-GSH MNPs, the conjugates (**2**-CoFe<sub>2</sub>O<sub>4</sub>-GSH and **7**-CoFe<sub>2</sub>O<sub>4</sub>) were found to have fluorescence quantum yields of <0.01 and 0.058, respectively and lifetimes of 2.20 and 2.29, respectively. Fluorescence quantum yields of 0.02 and 0.062 were found for **2**-CoFe<sub>2</sub>O<sub>4</sub>-GSH (mix) and **7**-CoFe<sub>2</sub>O<sub>4</sub> (mix), respectively as well as fluorescence lifetimes of 2.60 and 2.46 ns respectively.

A decrease in both the fluorescence quantum yields and lifetimes was observed for all the conjugates compared to the Pcs alone. These results therefore show that in the presence of MNPs, most of the energy of the excited photosensitizer is transferred through intersystem crossing (ISC) and very little is given off through fluorescence.

**Table 4.1:** Photophysical properties of zinc Pcs and their respective Pc-MNP conjugates. Capping ligands are shown in denoting the conjugates of complex **2** for clarity since different ligands were employed.

Catalyst	Solvent	$\lambda_{\text{abs}}$ (nm)	Log $\epsilon$ at Q band maxima	$\Phi_{\text{F}}$	$\tau_{\text{F}}$ (ns)	$\Phi_{\text{T}}$	$\tau_{\text{T}}$ ( $\mu\text{s}$ )	$\Phi_{\Delta}$
<b>1</b>	DMSO	678 <sup>a</sup>	678 (5.27) <sup>a</sup>	0.1 <sup>a</sup>	3.00 <sup>a</sup>	0.49 <sup>a</sup>	238 <sup>a</sup>	0.17 <sup>a</sup>
<b>1-CoFe<sub>2</sub>O<sub>4</sub></b>	DMSO	678	-	<0.01	2.89	0.63	278	0.59
<b>2</b>	DMSO	686 <sup>b</sup>	686 (5.30) <sup>b</sup>	0.06 <sup>b</sup>	2.79 <sup>b</sup>	0.51 <sup>b</sup>	315 <sup>b</sup>	0.38 <sup>b</sup>
<b>2-CoFe<sub>2</sub>O<sub>4</sub>-COOH</b>	DMSO	686	-	<0.01	2.60	0.76	317	0.65
<b>2-CoFe<sub>2</sub>O<sub>4</sub>-GSH</b>	DMSO	686	-	<0.01	2.20	0.85	256	0.62
				0.02 <sup>d</sup>	2.60 <sup>d</sup>	0.70 <sup>d</sup>	270 <sup>d</sup>	0.58 <sup>d</sup>
<b>3</b>	Toluene	680	680 (5.06)	0.067	9.07	0.71	69.0	0.39
<b>4</b>	Water	683	-	-	-	-	-	0.24
<b>4-CoFe<sub>2</sub>O<sub>4</sub></b>	Water	683	-	-	-	-	-	0.42
<b>5</b>	Toluene	676	676 (5.20)	0.055	6.16	0.76	37.7	0.47
<b>6</b>	DMSO	676	676 (5.21)	0.14	7.60	0.82	129	0.57
<b>6-CoFe<sub>2</sub>O<sub>4</sub></b>	DMSO	676	-	0.078	3.14	0.88	96.4	0.62
<b>7</b>	DMSO	689 <sup>c</sup>	689 (5.21) <sup>c</sup>	0.11 <sup>c</sup>	2.53 <sup>c</sup>	0.83 <sup>c</sup>	351 <sup>c</sup>	0.30 <sup>c</sup>
<b>7-CoFe<sub>2</sub>O<sub>4</sub></b>	DMSO	689	-	0.058	2.29	0.88	355	0.65
				0.062 <sup>d</sup>	2.46 <sup>d</sup>	0.85 <sup>d</sup>	342 <sup>d</sup>	0.50 <sup>d</sup>

<sup>a</sup>values from Reference [58]

<sup>b</sup>values from Reference [60]

<sup>c</sup>values from Reference [63]

<sup>d</sup>values for the mixed composites; **2-CoFe<sub>2</sub>O<sub>4</sub>-GSH (mix)** and **7-CoFe<sub>2</sub>O<sub>4</sub> (mix)** respectively

## 4.2 Triplet Quantum Yields ( $\Phi_T$ ) and Lifetimes ( $\tau_T$ )

The triplet decay curves of the complexes showed first order kinetics as shown in **Figure 4.2** (using **1**-CoFe<sub>2</sub>O<sub>4</sub> as an example) and the triplet state parameters ( $\Phi_F$ ,  $\tau_F$ ) were then determined experimentally using laser flash photolysis. The essence of conjugating the Pcs to the MNP was to enhance ISC thereby further populating the triplet state of the excited Pc so as to enhance the singlet oxygen production which facilitates photocatalysis. As shown in **Table 4.1**, triplet quantum yields of complexes **1** and **2** are 0.49 [58] and 0.51 [60] respectively while those of **1**-CoFe<sub>2</sub>O<sub>4</sub> and **2**-CoFe<sub>2</sub>O<sub>4</sub>-COOH were found to be 0.63 and 0.76, respectively. Although there is an observed enhancement in the triplet quantum yields of both the Pc complexes after conjugation to MNPs, the results however show a greater enhancement for complex **2** in **2**-CoFe<sub>2</sub>O<sub>4</sub>-COOH, with a larger loading of Pc than **1**-CoFe<sub>2</sub>O<sub>4</sub> (**Table 3.2**). The increase in triplet quantum yields for both Pcs after conjugation to MNPs is due to the heavy atom effect of the CoFe<sub>2</sub>O<sub>4</sub> MNPs which enhances ISC of the excited Pcs. The triplet lifetimes for complexes **1** and **2** are shown in **Table 4.1** wherein they increased with increase in the triplet quantum yield. The triplet lifetimes for complexes **1** and **2** are 238 [58] and 315  $\mu$ s [60], respectively and increased upon conjugation to 278 and 317  $\mu$ s for **1**-CoFe<sub>2</sub>O<sub>4</sub> and **2**-CoFe<sub>2</sub>O<sub>4</sub>-COOH, respectively (only slightly for the latter). It is expected that when triplet quantum yields increase that triplet lifetimes will decrease [154]. The lengthening of the triplet lifetimes for complexes **1** and **2** in the presence of MNPs could be due to their shielding by the MNPs which are larger in size.

As stated before complexes **3** and **5** do not have the necessary functional groups for conjugation to MNPs. The obtained triplet quantum yields for the Pcs alone though were found to be 0.71 and 0.76 respectively, showing that the unsymmetrical Pc (**5**) has a slightly

higher triplet quantum yield than the symmetrical Pc (**3**). The obtained triplet lifetimes are of 69.0 and 37.7  $\mu\text{s}$  for complexes **3** and **5** respectively in toluene, **Table 4.1**.

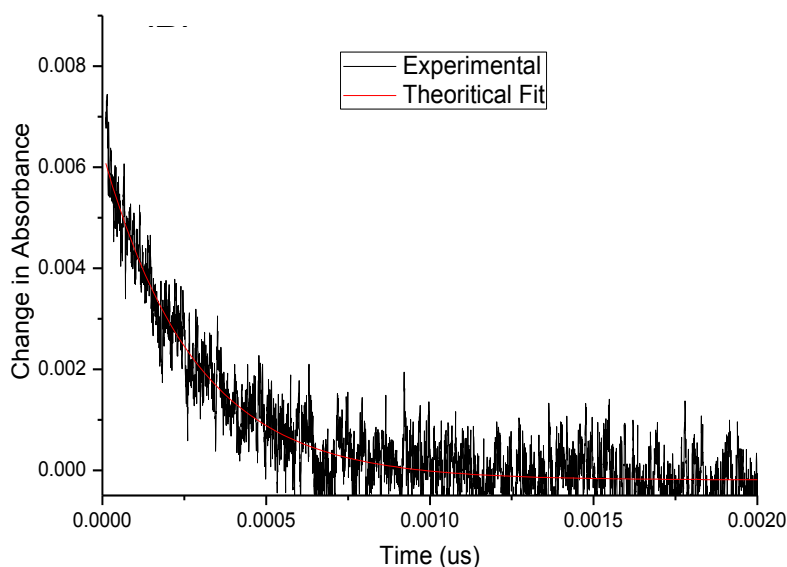


**Figure 4.2:** Monoexponential triplet decay curve of **1-CoFe<sub>2</sub>O<sub>4</sub>** conjugate in DMSO.

Since the quantification of the triplet quantum yield of Pcs in water using the laser flash photolysis reported herein is not possible, the triplet quantum yield of complex **4** and its conjugate (**4-CoFe<sub>2</sub>O<sub>4</sub>**) could not be determined as no signal is observed in water. As shown in **Table 4.1** however, triplet quantum yields of complex **6** and its conjugate (**6-CoFe<sub>2</sub>O<sub>4</sub>**) were found to be 0.82 and 0.88, respectively. The increase is due to the heavy atom effect as explained before. There was an observed decrease in the triplet lifetime with increase in triplet quantum yield wherein the triplet lifetimes of complex **6** and **6-CoFe<sub>2</sub>O<sub>4</sub>** were found to be 129 and 96.4  $\mu\text{s}$  respectively. Thus the increase in the triplet lifetimes that was observed for **1-CoFe<sub>2</sub>O<sub>4</sub>** is not observed for **6-CoFe<sub>2</sub>O<sub>4</sub>** even though they are conjugated to the same of **CoFe<sub>2</sub>O<sub>4</sub>-NH<sub>2</sub>** MNPs. This is possibly because the  $\sigma$  C–H bonds of the *tert*-butyl substituents in complex **6** may exhibit what is known as the “loose bolt” effect which is attributed to the vibration of bonds set off by the parent molecule. The “loose bolt” effect accelerates internal

conversion (IC) since electronic energy “leaks out” through C–H vibrations [140], hence the triplet lifetimes are shortened for **6**-CoFe<sub>2</sub>O<sub>4</sub> and not for **1**-CoFe<sub>2</sub>O<sub>4</sub>.

As mentioned before, the triplet quantum yield of complex **2** is 0.51 [60]. It changed upon covalent linkage with CoFe<sub>2</sub>O<sub>4</sub>-GSH MNPs resulting in **2**-CoFe<sub>2</sub>O<sub>4</sub>-GSH to of 0.85. When the Pc and MNPs were just mixed together (**2**-CoFe<sub>2</sub>O<sub>4</sub>-GSH (mix)), a composite with a triplet quantum yield of 0.70 was obtained. These results show that the heavy atom effect of the CoFe<sub>2</sub>O<sub>4</sub>-GSH MNPs can be greater when there is covalent bond formation between the Pc and MNPs. The triplet quantum yield of complex **7** is 0.83 [63] while those of **7**-CoFe<sub>2</sub>O<sub>4</sub> and **7**-CoFe<sub>2</sub>O<sub>4</sub> (mix) were found to be 0.88 and 0.85, respectively, showing an insignificant increase for **7**-CoFe<sub>2</sub>O<sub>4</sub> (mix). The reported triplet lifetime for complex **2** is 315 μs [60] while **2**-CoFe<sub>2</sub>O<sub>4</sub>-GSH and **2**-CoFe<sub>2</sub>O<sub>4</sub>-GSH (mix) were found to have triplet lifetimes of 256 and 270 μs respectively. The reported triplet lifetime for complex **7** on the other hand is 351 μs [63] while **7**-CoFe<sub>2</sub>O<sub>4</sub> and **7**-CoFe<sub>2</sub>O<sub>4</sub> (mix) were found to have triplet lifetimes of 355 and 342 μs respectively. Based on the increase in the triplet quantum yields for the Pc-MNP conjugates reported in this work, an increased ability to produce singlet oxygen is expected.

### 4.3 Singlet Oxygen Quantum Yield ( $\Phi_{\Delta}$ )

The  $\Phi_{\Delta}$  values were determined using DPBF and ADMA as singlet oxygen quenchers in organic and aqueous solvents respectively. The  $\Phi_{\Delta}$  values were determined using ZnPc in DMSO where  $\Phi_{\Delta}^{\text{Std}} = 0.67$  [143] and toluene where  $\Phi_{\Delta}^{\text{Std}} = 0.58$  [144]. AlPcSmix was employed as a standard ( $\Phi_{\Delta} = 0.42$  [144]) for the water soluble Pc.

With increase in the triplet quantum yield, the singlet oxygen quantum yield is also expected to increase because the more populated the triplet state is, the more singlet oxygen is produced. The decay of DPBF upon irradiation is shown in **Figure 4.3**, wherein complex **6** was used as an example. There were no significant changes in the intensity of the Q band in DMSO or toluene for the period of irradiation time, indicating stability of the Pcs and their conjugates (**Figure 4.3 (A)**). The degradation of DPBF was monitored at 417 nm and was due the production of singlet oxygen. This means that the rate of decay of the DPBF is directly related to the production of singlet oxygen. In the case of the water soluble Pc, complex **4** and its conjugate (**4-CoFe<sub>2</sub>O<sub>4</sub>**), the decay of ADMA was monitored at 380 nm and there were no changes in the intensity of the Q band of the Pc (**Figure 4.3 (B)**).

As shown in **Table 4.1**, the reported singlet oxygen quantum yields for complexes **1** and **2** alone are 0.17 [**58**] and 0.38 [**60**] respectively, while those of **1-CoFe<sub>2</sub>O<sub>4</sub>** and **2-CoFe<sub>2</sub>O<sub>4</sub>-COOH** were found to be 0.59 and 0.65 respectively. Even though **2-CoFe<sub>2</sub>O<sub>4</sub>-COOH** was found to have a higher singlet oxygen quantum yield than **1-CoFe<sub>2</sub>O<sub>4</sub>**, the extent of enhancement of the singlet oxygen production shows that complex **1** improved by 0.42 in **1-CoFe<sub>2</sub>O<sub>4</sub>** while complex **2** improved by 0.27 in **2-CoFe<sub>2</sub>O<sub>4</sub>-COOH**. This is in contrast to what was expected considering that **2-CoFe<sub>2</sub>O<sub>4</sub>** has 6 bound Pcs and **1-CoFe<sub>2</sub>O<sub>4</sub>** has 4 (**Table 3.2**). Therefore the longer linkage chain in **2-CoFe<sub>2</sub>O<sub>4</sub>-COOH** might allow for more Pcs to bind, but it suppresses the enhancement of the singlet oxygen generation of the Pcs, possibly due to increase in the nanoparticles size. The larger nanoparticles possibly reduce the efficient energy transfer between the excited triplet state of the Pc and the ground state molecular oxygen [**155**].

The obtained singlet oxygen quantum yields for complexes **3** and **5** are 0.39 and 0.47 respectively in toluene, **Table 4.1**. The results correlate to the triplet quantum yields wherein the unsymmetrical complex **5** has a higher singlet oxygen quantum yield than the symmetrical complex **3**. The obtained singlet oxygen quantum yield for complex **4** is 0.24 and that of **4-CoFe<sub>2</sub>O<sub>4</sub>** is 0.42 in water while complex **6** and its conjugate (**6-CoFe<sub>2</sub>O<sub>4</sub>**) have singlet oxygen quantum yields of 0.57 and 0.62 respectively in DMSO, **Table 4.1**.

As mentioned, the reported singlet oxygen quantum yield for complex **2** is 0.38 [60] while **2-CoFe<sub>2</sub>O<sub>4</sub>-GSH** and **2-CoFe<sub>2</sub>O<sub>4</sub>-GSH (mix)** have singlet oxygen quantum yields of 0.62 and 0.58, respectively, **Table 4.1**. Complex **7** on the other hand has a singlet oxygen quantum yield of 0.30 [63] while **7-CoFe<sub>2</sub>O<sub>4</sub>** and **7-CoFe<sub>2</sub>O<sub>4</sub> (mix)** were found to have singlet oxygen quantum yields of 0.65 and 0.50, respectively. The results show that the enhancement of singlet oxygen production is greater when there is a covalent linkage between the Pc and MNP and not just a mixture. Results also show that even though complex **7** was found to form less amide bonds with the GSH-CoFe<sub>2</sub>O<sub>4</sub> MNPs (Chapter 3), it still has a greater enhancement of its singlet oxygen quantum yield when conjugated to the GSH-CoFe<sub>2</sub>O<sub>4</sub> MNPs than complex **2**. When conjugated to Fe<sub>3</sub>O<sub>4</sub> MNPs, the singlet oxygen quantum yield of complex **7** was found to be 0.41 [63] compared to the 0.65 found here when GSH-CoFe<sub>2</sub>O<sub>4</sub> MNPs are used. Thus, the conjugation of Pcs to mixed metal MNPs (CoFe<sub>2</sub>O<sub>4</sub>-GSH MNPs in this case) as opposed Fe<sub>3</sub>O<sub>4</sub> MNPs better enhances the singlet oxygen generation of the Pcs.

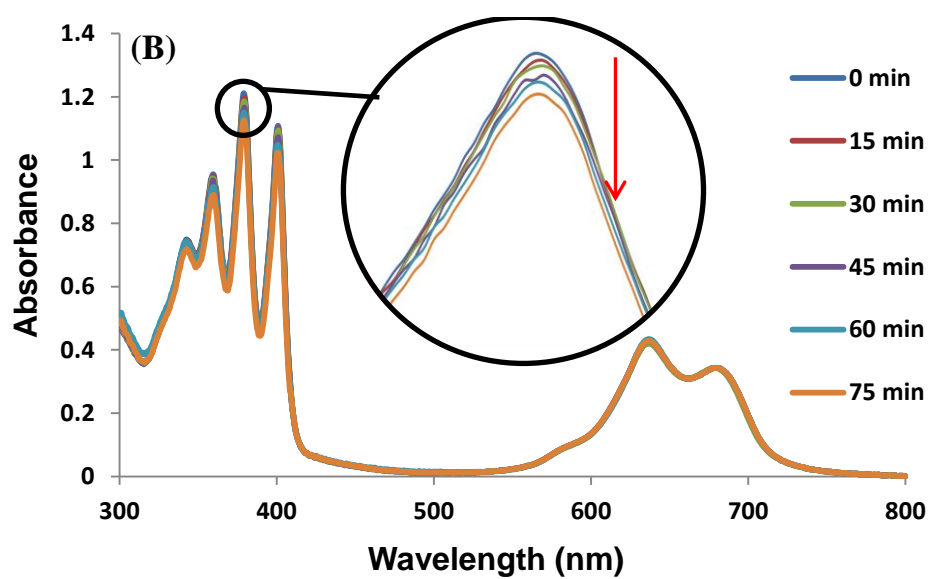
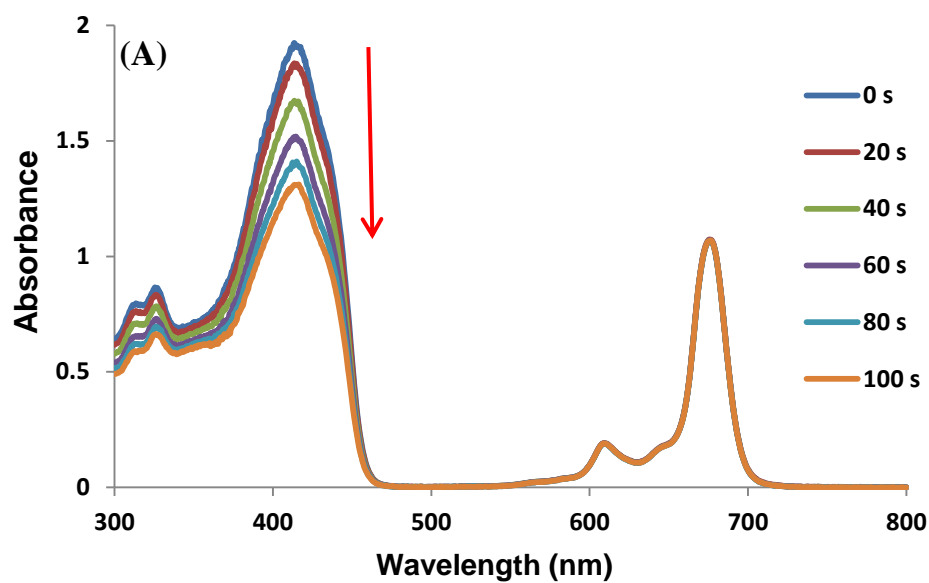


**Figure 4.3:** Absorption spectral changes for the quantification of singlet oxygen quantum yield for (A) complex **6** in  $8.52 \times 10^{-5} \text{ molL}^{-1}$  DPBF at 20 second irradiation intervals in DMSO and (B) complex **4** in  $3.60 \times 10^{-5} \text{ molL}^{-1}$  ADMA at 15 minute irradiation intervals in water.



## **Closing Remarks**

The photophysical and photochemical properties of Pcs and their respective Pc-MNP conjugates were determined. Due to the ability of the Pcs and their respective composites to generate singlet oxygen when dissolved in solution, some of these photoactive molecules were incorporated in electrospun fibers and characterized as discussed in the next chapter.

# CHAPTER 5

## Results and Discussion

## 5. Electrospun polymer fibers

This chapter reports on the microscopic, spectroscopic, and photophysical properties of electrospun fibers that have been functionalised with Pcs, CoFe<sub>2</sub>O<sub>4</sub> MNPs and Pc-CoFe<sub>2</sub>O<sub>4</sub> conjugates.

### 5.1 Characterisation of functionalised electrospun fibers

Polystyrene (PS) was used to embed Pc complexes **1** and **2**, CoFe<sub>2</sub>O<sub>4</sub>-NH<sub>2</sub> MNPs, CoFe<sub>2</sub>O<sub>4</sub>-COOH and their respective conjugates (**1**-CoFe<sub>2</sub>O<sub>4</sub> and **2**-CoFe<sub>2</sub>O<sub>4</sub>-COOH) to get CoFe<sub>2</sub>O<sub>4</sub>-NH<sub>2</sub>/PS, CoFe<sub>2</sub>O<sub>4</sub>-COOH/PS, **1**/PS, **2**/PS, **1**-CoFe<sub>2</sub>O<sub>4</sub>/PS and **2**-CoFe<sub>2</sub>O<sub>4</sub>/PS (please note that **2**-CoFe<sub>2</sub>O<sub>4</sub>-COOH is represented without -COOH when electrospun for simplicity and is denoted **2**-CoFe<sub>2</sub>O<sub>4</sub>/PS). As mentioned before however, there was observed leaching when a water soluble (complex **4**) was electrospun in PS. Polyamide-6 (PA-6) was then employed as a substitute to prevent loss of the photocatalyst and hence additional pollution. PA-6 was chosen as it has been successfully used in electrospinning a water soluble Pc before with no observed leaching upon application [76]. Pc complexes **4** and **6**, CoFe<sub>2</sub>O<sub>4</sub>-NH<sub>2</sub> MNPs and their respective conjugates (**4**-CoFe<sub>2</sub>O<sub>4</sub> and **6**-CoFe<sub>2</sub>O<sub>4</sub>) were therefore embedded in PA-6 to get CoFe<sub>2</sub>O<sub>4</sub>-NH<sub>2</sub>/PA-6, **4**/PA-6, **6**/PA-6, **4**-CoFe<sub>2</sub>O<sub>4</sub>/PA-6 and **6**-CoFe<sub>2</sub>O<sub>4</sub>/PA-6. As mentioned before, complexes **3** and **5** were not electrospun as their conjugation to CoFe<sub>2</sub>O<sub>4</sub> MNPs was not possible (ester functional groups) hence enhancement of their singlet oxygen quantum yields and photocatalytic behaviour was not possible either. Pc complex **7** and its respective conjugate (**7**-CoFe<sub>2</sub>O<sub>4</sub>) were not electrospun due to time constraints. The characterisation of the functionalised PS and PA-6 fibers is reported below.

### 5.1.1 Scanning Electron Microscopy (SEM)

SEM analyses were conducted for the electrospun fibers before and after embedding them with the compounds so as to obtain their topography and size distribution. The images of PS alone, **1**/PS and **1**-CoFe<sub>2</sub>O<sub>4</sub>/PS (as examples) are shown in **Figure 5.1**. The images reveal that there is an even distribution of fibers and an increase in fiber diameter with modification with the extent of increase being greater for incorporation of Pc-MNP conjugates than the Pc alone. The values for the diameters of all the functionalised PS fibers are shown on **Table 5.1**. The SEM images also reveal that the fibers are cylindrical and unbranched with relatively smooth surfaces even after incorporation of the Pcs, MNPs and Pc-MNP conjugates. Similar behaviour was observed for **2**/PS and **2**-CoFe<sub>2</sub>O<sub>4</sub>/PS (figures not shown but diameters listed in **Table 5.1**). Thus, the larger sized **2**-CoFe<sub>2</sub>O<sub>4</sub>-COOH (17.67 nm by DLS) resulted in a larger fiber diameter than the smaller **1**-CoFe<sub>2</sub>O<sub>4</sub> (14.11 nm by DLS), suggesting that the size of the nanoparticles affects their electrospun fiber diameter.

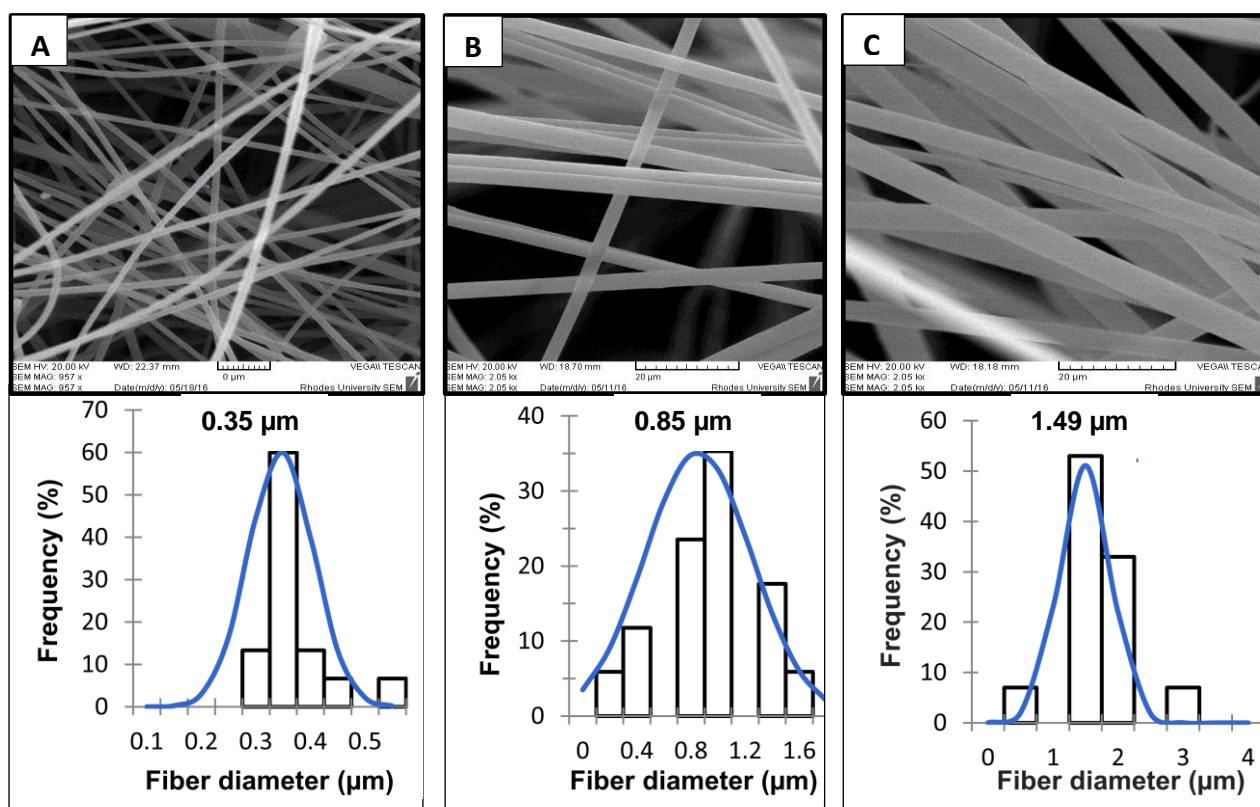


**Figure 5.1:** SEM images of (A) PS only, (B) **1**/PS and (C) **1**-CoFe<sub>2</sub>O<sub>4</sub>/PS, and their corresponding histograms (showing size distribution of the fibers).

The images of PA-6 alone, **4**/PA-6 and **4**-CoFe<sub>2</sub>O<sub>4</sub>/PA-6 (as examples) are shown in **Figure 5.2**. The images reveal fibers with cylindrical, unbranched and have smooth surfaces. Just as with PS, there is an observed increase in the PA-6 fiber diameter with modification with the extent of increase being greater for incorporation of Pc-MNP conjugates compared to the Pc alone. The PA-6 fiber diameters were observed to be a lot smaller than PS fibers, even after functionalisation, this could be possibly due to the fact that 120 mg of the photocatalysts were electrospun in PS compared to the 40 mg that was used in the PA-6 fibers. Different amounts of the photocatalysts were used due to low synthetic yields obtained for the unsymmetrical Pc (complex **6**) than the symmetrical complexes. In the case of complex **4**, 40 mg was used because a comparative study on the photocatalytic efficiencies of **4**/PA-6 and **6**/PA-6 was conducted hence their preparation was the same.

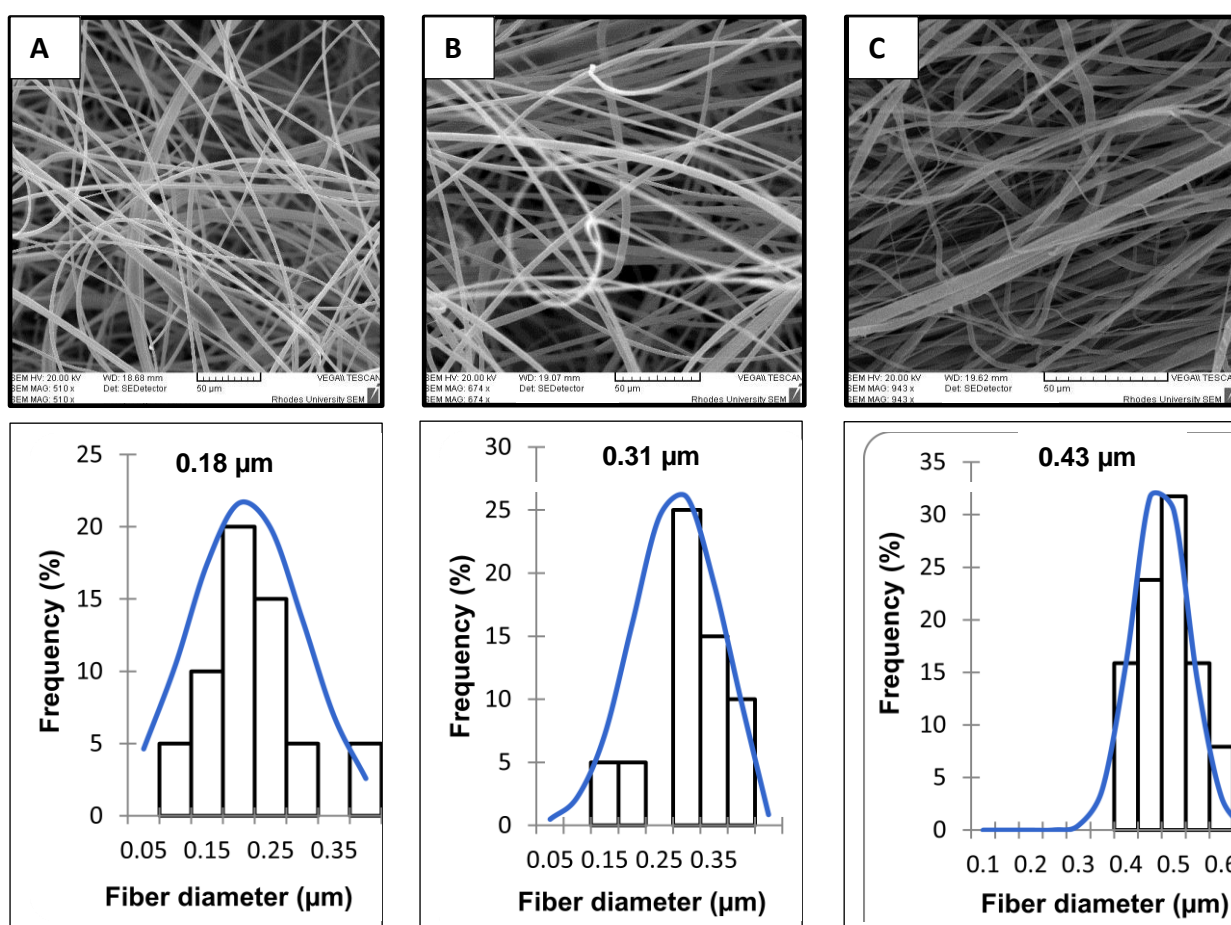


**Figure 5.2:** SEM images of (A) PA-6 only, (B) **4**/PA-6 and (C) **4**-CoFe<sub>2</sub>O<sub>4</sub>/PA-6, and their corresponding histograms (showing size distribution of the fibers).

## 5.1.2 Surface area and Porosity analyses

### 5.1.2 Surface area and Porosity analyses

The nitrogen adsorption-desorption isotherms for the electrospun PS fibers are shown in **Figure 5.3** (using PS alone, **1**/PS and **1**-CoFe<sub>2</sub>O<sub>4</sub>/PS as examples) and in **Figure 5.4** for electrospun PA-6 fibers (using PA-6 alone, **4**/PA-6 and **4**-CoFe<sub>2</sub>O<sub>4</sub>/PA-6 as examples). The isotherms describe the partitioning between gas phase and adsorbed species as a function of applied pressure. The BET characterization reveals that all the electrospun fibers show type IV sorption isotherms. This is an indication that the fibers have a wide distribution of pore sizes wherein there is an indefinite multi-layer formation after completion of the monolayer [156]. This suggests that at high pressures there is an increased uptake of adsorbates and as pores become filled, an inflection point is reached near the completion of the first adsorbed monolayer. The obtained surface areas and pore volumes for the electrospun fibers are listed in **Table 5.1**. The results show that the unfunctionalised fibers; PS and PA-6 have the smallest surface areas of 16.15 and 39.33 m<sup>2</sup>/g respectively compared to when they are functionalised. The results also show that the fibers functionalised with the Pc-MNP conjugates have greater surface areas than those functionalised with the Pcs alone (except for **4**-CoFe<sub>2</sub>O<sub>4</sub>). It has been reported before that reducing fiber diameter increases the surface area to volume ratio and vice versa [157]. As shown in **Table 5.1**, results obtained in this work do not necessarily follow this phenomenon.

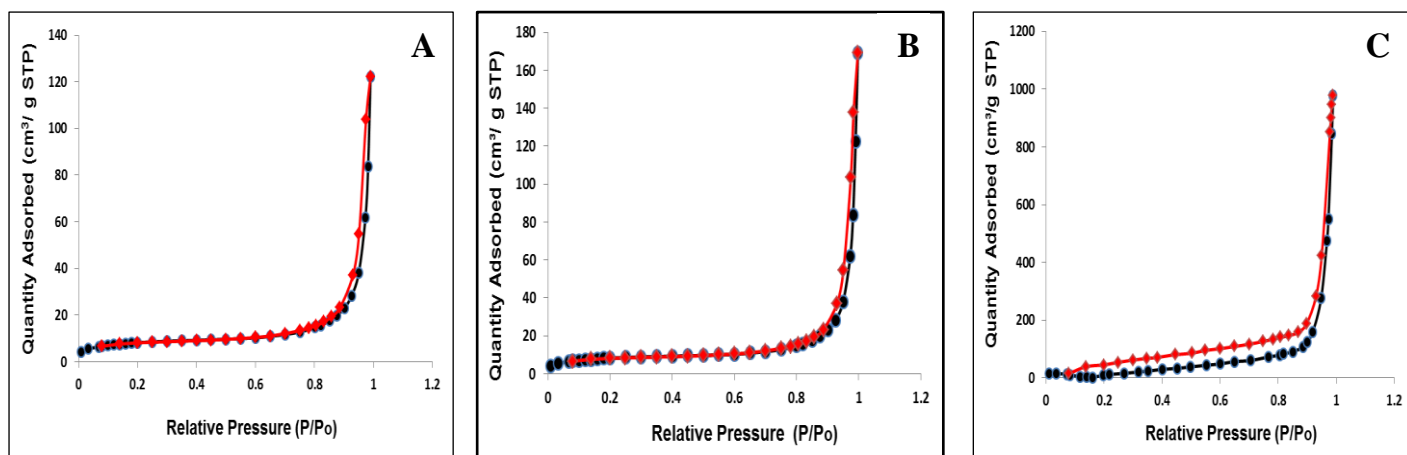


**Figure 5.3:** Nitrogen adsorption-desorption BET isotherms of: A; PS alone, B; **1**/PS and C; **1**-CoFe<sub>2</sub>O<sub>4</sub>/PS. The black line denotes the absorption while the red lines are desorption of the complexes respectively.

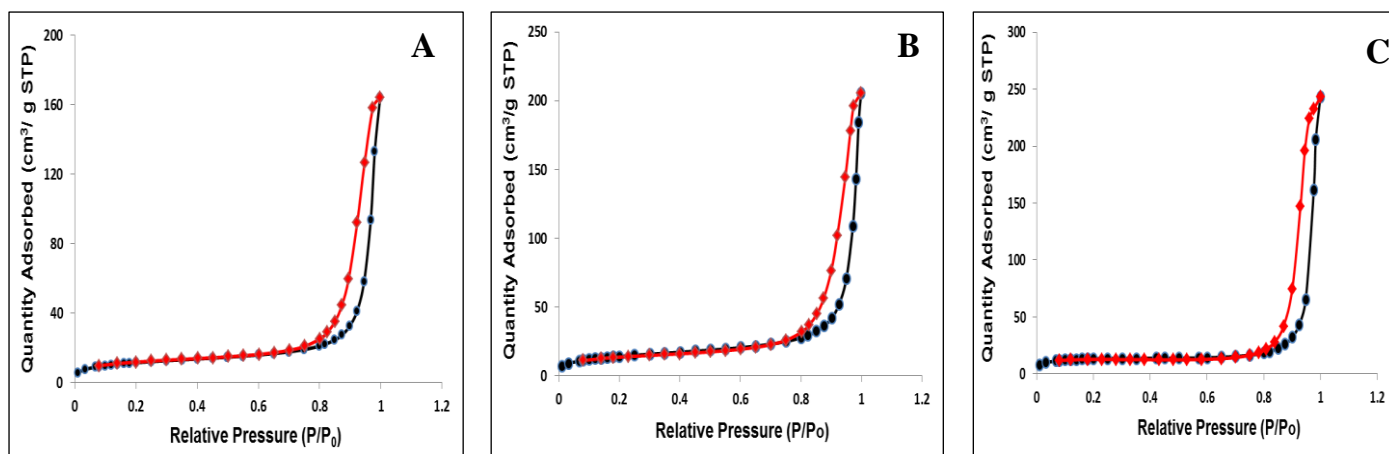


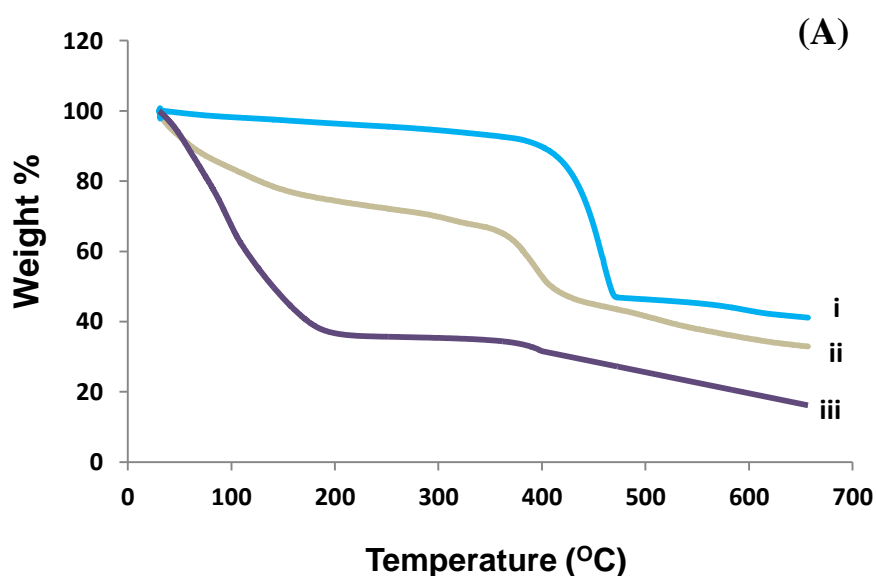
**Figure 5.4:** Nitrogen adsorption-desorption BET isotherms of: A; PA-6 alone, B; **4**/PA-6 and C; **4**-CoFe<sub>2</sub>O<sub>4</sub>/PA-6. The black line denotes the absorption while the red lines are desorption of the complexes respectively.

### 5.1.3 Thermal Stability

The thermal stability of the PS and PA-6 fibers before and after embedding them with the photocatalysts was tested. Thermograms comparing the thermal decay profiles of the PS fibers using PS only, **1**/PS and **1**-CoFe<sub>2</sub>O<sub>4</sub>/PS as examples are shown on **Figure 5.5 (A)**. The

thermograms reveal that PS alone possesses the lowest thermal stability. This could be due to the mobility and disintegration of the polymer chains upon exposure to heat. The thermograms also reveal that upon incorporation of complex **1** and **1-CoFe<sub>2</sub>O<sub>4</sub>** into the polymer, its thermal stability increased with greater stability being for the **1/PS**. The increased stability after incorporation of compounds is possibly a result of hindrance effect on the movement of the polymer chains.

Similar behaviour was observed for the PA-6 fibers wherein the fiber on its own was found to exhibit the lowest thermal stability. Increased thermal stability was observed upon incorporation of the complex **4** and **4-CoFe<sub>2</sub>O<sub>4</sub>** into the fibers, for the same reasons explained above for PS. However in this case, **4-CoFe<sub>2</sub>O<sub>4</sub>/PA-6** possessed the greatest thermal stability, **Figure 5.5 (B)**. Comparison of the PS and PA-6 fibers before and after incorporation of the photocatalysts shows that the PS fibers possess greater thermal stability than the PA-6 fibers. This is possibly because larger amounts of the photocatalysts (120 mg) were electrospun in PS that hinders the polymer chain movement better than in PA-6 with less amount of photocatalysts (40 mg).





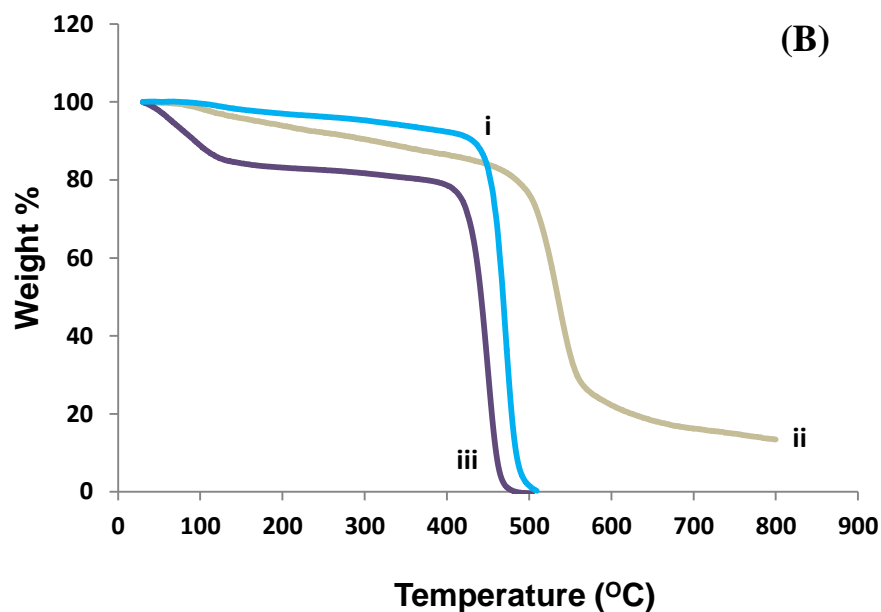


**Figure 5.5:** TGA thermograms of (A) i. **1**/PS, ii. **1**-CoFe<sub>2</sub>O<sub>4</sub>/PS, iii. PS only and (B) i. **4**/PA-6, ii. **4**-CoFe<sub>2</sub>O<sub>4</sub>/PA-6, iii. PA-6 only.

#### 5.1.4 UV-visible spectroscopy

Solid state spectroscopy of the functionalised fibers was conducted so as to prove that the photocatalysts and their respective conjugates were embedded in the fibers. As shown in **Figure 5.6 (A)** where the spectra of **1**/PS, **2**/PS, **1**-CoFe<sub>2</sub>O<sub>4</sub>/PS and **2**-CoFe<sub>2</sub>O<sub>4</sub>/PS are shown and **Figure 5.6 (B)** where the spectra of **4**/PA-6, **6**/PA-6, **4**-CoFe<sub>2</sub>O<sub>4</sub>/PA-6 and **6**-CoFe<sub>2</sub>O<sub>4</sub>/PA-6 are shown, there is broadening of the spectra due to aggregation, typical for Pcs in solid state [158]. There is also an observed red shift of the monomer (low energy band) components of the Q band for the complexes compared to when in solution (**Table 5.1**), which is common for Pcs in the solid state [159]. The fact that the Q band is observed for the Pc within the PS and PA-6 fibers also confirms that it and its respective conjugates are embedded in the fiber and remain intact within the fiber following the electrospinning process.

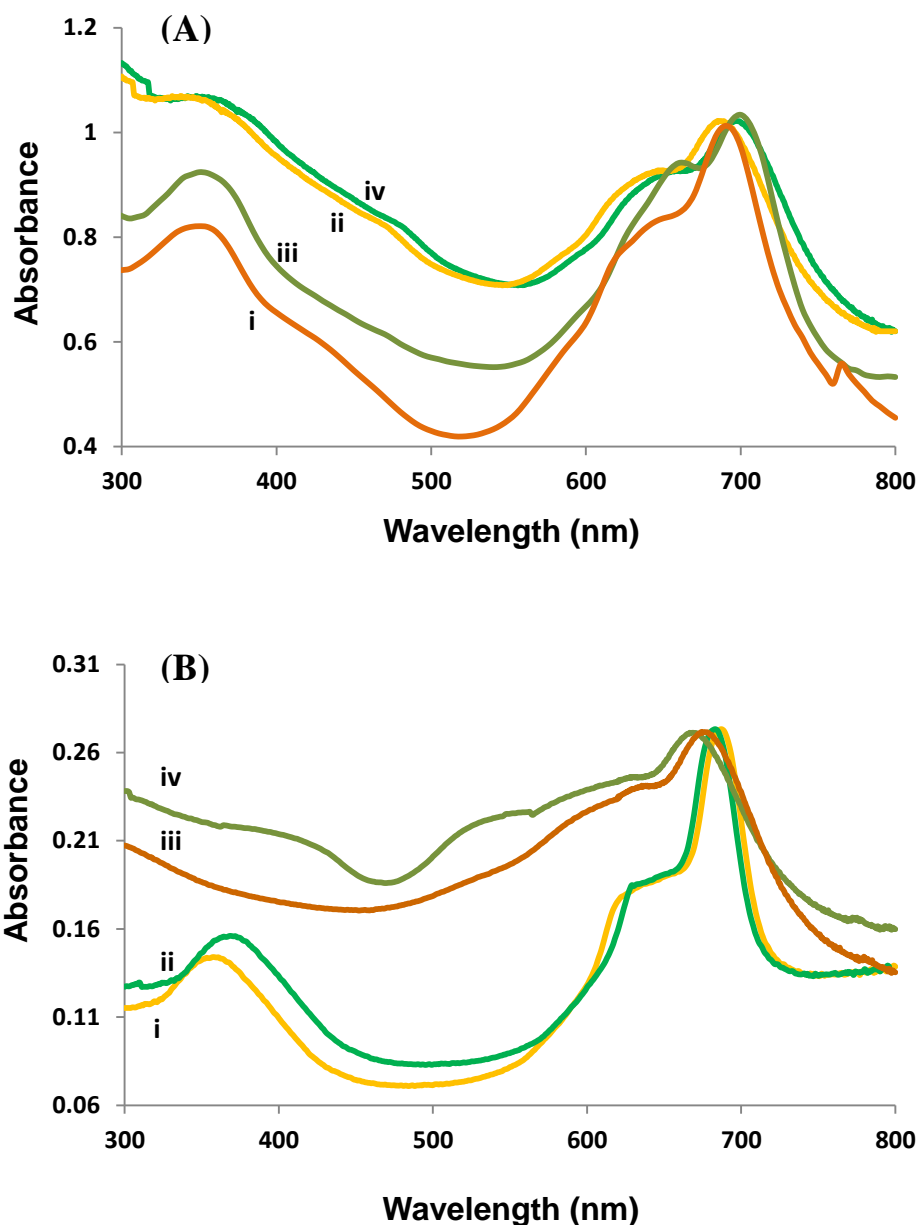


**Figure 5.6:** Solid state UV-vis spectra of (A) i. **1**/PS, ii. **1**-CoFe<sub>2</sub>O<sub>4</sub>/PS, iii. **2**/PS, iv. **2**-CoFe<sub>2</sub>O<sub>4</sub>/PS and (B) i. **4**/PA-6, ii. **4**-CoFe<sub>2</sub>O<sub>4</sub>/PA-6, iii. **6**/PA-6 and iv. **6**-CoFe<sub>2</sub>O<sub>4</sub>/PA-6 wherein 120 mg and 40 mg of each of the photocatalysts were embedded in PS and PA-6 respectively.

## 5.2 Singlet oxygen generating ability of the functionalised fibers

The photochemical properties of phthalocyanine-functionalised polymer fibers have been reported to be maintained within the solid polymeric matrix [160]. In this work, the singlet

oxygen generating abilities of the functionalised polystyrene and polyamide-6 fibers were evaluated and reported with the aim of fabricating photocatalytically active fibers.

As shown in **Table 5.1**, the Pc and Pc-MNP conjugates reported herein produced singlet oxygen which was quantified using DPBF and ADMA as singlet oxygen quenchers in organic solvents and water respectively. The singlet oxygen generation of the Pcs and their respective conjugates when embedded in fibers was also determined and reported here, where ADMA was used as the singlet oxygen quencher in water. ADMA degradation was monitored at 380 nm in aqueous solution submerged with 20 mg of the functionalised fibers (**Figure 5.7** insert). The obtained degradation spectra are shown in **Figure 5.7** (using **4**/PA-6 as an example for the ADMA degradation). The lack of the Pc Q band in **Figure 5.7** is an indication that no leaching of the Pc from the PA-6 fiber occurs even though complex **4** is itself water soluble. The singlet oxygen quantum yield values of **1**/PS and **2**/PS in water were found to be 0.20 and 0.40 respectively while those of **1**-CoFe<sub>2</sub>O<sub>4</sub>/PS and **2**-CoFe<sub>2</sub>O<sub>4</sub>/PS were found to be 0.60 and 0.63 respectively in water (**Table 5.1**). The singlet oxygen quantum yield values of **4**/PA-6 and **6**/PA-6 in water were found to be 0.15 and 0.21 respectively while those of **4**-CoFe<sub>2</sub>O<sub>4</sub>/PA-6 and **6**-CoFe<sub>2</sub>O<sub>4</sub>/PA-6 were found to be 0.32 and 0.45, respectively (**Table 5.1**). The obtained results show that the Pcs and their respective conjugates maintain their photophysical properties in the fibers i.e. the Pc-MNP conjugates have greater  $\Phi_{\Delta}$  than their respective Pcs due to the presence of the CoFe<sub>2</sub>O<sub>4</sub> magnetic nanoparticles. Since 120 mg of the photocatalysts were electrospun in the PS fibers compared to the 40 mg that was electrospun in the PA-6 fibers, comparison of the singlet oxygen quantum yield values obtained in each of the fibers cannot be made.

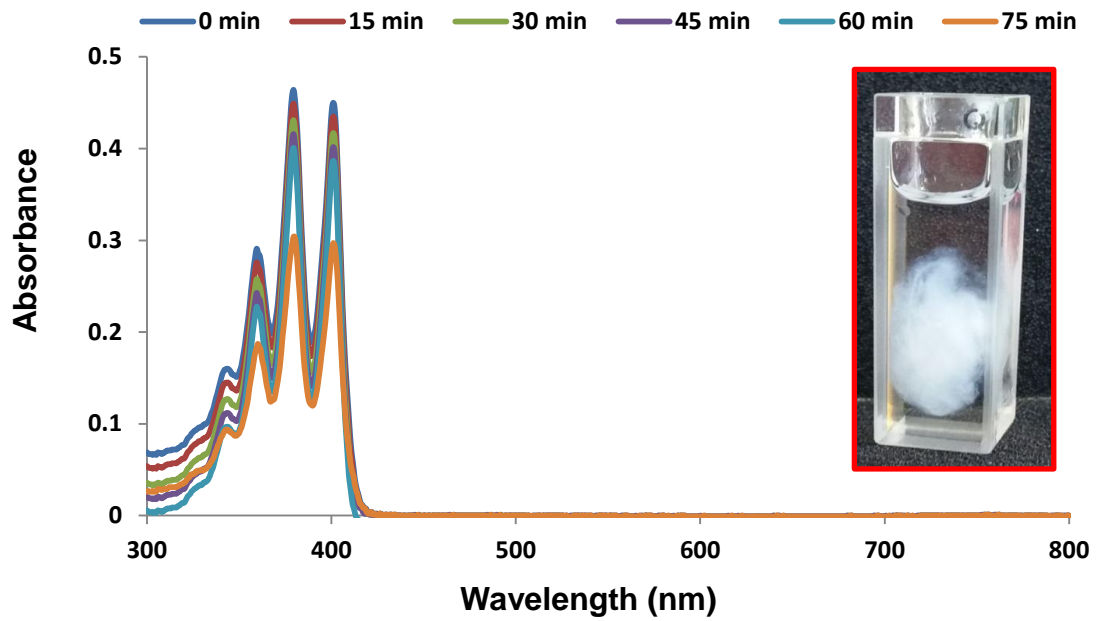


**Figure 5.7:** Photodegradation of  $1.38 \times 10^{-5} \text{ molL}^{-1}$  ADMA in the presence of 4/PA-6 in water at 15 minute irradiation intervals. Insert = picture of the fiber in the ADMA solution.

**Table 5.1:** Singlet oxygen quantum yields (in water) and other properties of the electrospun polystyrene and polyamide-6 fibers.

Functionalised fibers	Fiber Diameter ( $\mu\text{m}$ )	BET Analysis			$\lambda_{\text{abs}}^{\text{a}}$ (nm)	$\Phi_{\Delta}^{\text{a}}$
		Surface Area ( $\text{m}^2/\text{g}$ )	Pore Volume ( $\text{cm}^3/\text{g}$ )	Surface area: Volume ratio ( $1 \times 10^6 \text{ m}^{-1}$ )		
PS only	0.35	16.15	0.20	80.75	-	-
1/PS	0.85	27.70	0.19	145.8	689 (678)	0.20 (0.17)
1-CoFe <sub>2</sub> O <sub>4</sub> /PS	1.49	108.6	1.31	82.90	689 (678)	0.60 (0.59)
2/PS	0.87	37.83	0.31	122.0	695 (686)	0.40 (0.38)
2-CoFe <sub>2</sub> O <sub>4</sub> /PS	1.65	41.87	0.32	130.8	695 (686)	0.63 (0.65)
PA-6 only	0.18	39.33	0.25	157.3	-	-
4/PA-6	0.31	49.58	0.28	177.1	687 (683)	0.15 (0.24)
4-CoFe <sub>2</sub> O <sub>4</sub> /PA-6	0.43	47.97	0.28	171.3	687 (683)	0.32 (0.42)

<b>6/PA-6</b>	0.30	41.62	0.38	109.5	683 (676)	0.21 (0.57)
<b>6-CoFe<sub>2</sub>O<sub>4</sub>/PA-6</b>	0.42	51.82	0.26	199.3	685 (676)	0.45 (0.62)

<sup>a</sup>Values in brackets are for the photocatalysts in solution before electrospinning (in DMSO)

except for complex **4** and its conjugate (**4-CoFe<sub>2</sub>O<sub>4</sub>**) which are in water.

### 5.3 Closing remarks

The incorporation of photocatalysts in electrospun fibers was achieved and the photochemical properties of these functionalised fibers were then studied. The singlet oxygen generating abilities of the Pcs and Pc-CoFe<sub>2</sub>O<sub>4</sub> MNP conjugates were maintained in the solid fibers, thus these functionalised polymeric fiber materials could be promising for the photodegradation of water pollutants, a subject of the next chapter.

# CHAPTER 6

## Results and Discussion

## 6. Photocatalytic treatment of organic and inorganic pollutants

**This chapter reports on the application of Pcs, CoFe<sub>2</sub>O<sub>4</sub> MNPs and Pc-CoFe<sub>2</sub>O<sub>4</sub> MNP conjugates as photocatalysts in solution as well as their photocatalytic ability when electrospun in polymer fibers.**

Phthalocyanines can be employed as photocatalysts either in solution, in their solid state or when embedded in solid support systems [161]. In this work, Pcs are used in conjugation with MNPs and embedded in electrospun fibers and they are also used as colloids in solution. Since Pcs and their respective conjugates were found to generate adequate singlet oxygen even when incorporated into electrospun fibers, the functionalised fibers were applied in the photooxidation of OG and MO while the colloids were applied in the photooxidation of MO and photoreduction of Cr(VI).

### 6.1 Photooxidation of Orange G (OG)

#### 6.1.1 Application of Polystyrene (PS) fibers

Complexes **1** and **2** were conjugated to CoFe<sub>2</sub>O<sub>4</sub>-NH<sub>2</sub> MNPs and CoFe<sub>2</sub>O<sub>4</sub>-COOH MNPs to generate **1**-CoFe<sub>2</sub>O<sub>4</sub>, **2**-CoFe<sub>2</sub>O<sub>4</sub>-COOH, all of which were electrospun in PS producing photocatalytic nanofibers: **1**/PS, **2**/PS, CoFe<sub>2</sub>O<sub>4</sub>-NH<sub>2</sub>/PS, CoFe<sub>2</sub>O<sub>4</sub>-COOH/PS, **1**-CoFe<sub>2</sub>O<sub>4</sub>/PS and **2**-CoFe<sub>2</sub>O<sub>4</sub>/PS. As explained before, complexes **1** and **2** differ in the terminal groups that they have for amide bond formation so the effect of the length of the spacer between the Pcs and CoFe<sub>2</sub>O<sub>4</sub> MNPs on their photocatalytic activity is studied.



### 6.1.1.1 UV-vis spectra

The photocatalytic efficiencies of modified PS fibers (1/PS, 2/PS, CoFe<sub>2</sub>O<sub>4</sub>-NH<sub>2</sub>/PS, CoFe<sub>2</sub>O<sub>4</sub>-COOH/PS, 1-CoFe<sub>2</sub>O<sub>4</sub>/PS, 2-CoFe<sub>2</sub>O<sub>4</sub>/PS) were evaluated spectroscopically by monitoring the photodegradation of OG after exposure to the functionalised fibers and laser irradiations at two minute intervals (**Figure 6.1**). There was an observed decrease of intensity of the absorption peak at 476 nm after laser irradiations as seen in **Figure 6.1** (using 1-CoFe<sub>2</sub>O<sub>4</sub>/PS as an example). A pH of 7.4 was used as Pc based photocatalysts have successfully degraded OG at similar pH values before [70,72,76]. It has been reported before that amongst others, reactions that occur during OG photolysis include: aryl group hydroxylation and desulphonation [162]. There was also observed fading of the color of the dye solution (**Figure 6.1 (Insert)**), this was not surprising as it has been reported that the double bond in azo dyes determines the colour of the dyes and is very reactive usually undergoing oxidative cleavage during photodegradation, leading to fading of their colour [55]. Upon application of an unmodified fiber for the photodegradation of the dye, no spectral changes were observed. This was therefore an indication that the fiber has no catalytic contribution in the degradation process and merely acts a support system for the photocatalysts.

### 6.1.1.2 Kinetics Studies

Kinetic studies for the degradation of OG were performed and the data is listed in **Table 6.1**. The concentrations of OG used are:  $1.80 \times 10^{-5}$ ,  $3.30 \times 10^{-5}$ ,  $4.80 \times 10^{-5}$ ,  $9.10 \times 10^{-5}$  and  $2.65 \times 10^{-4}$  mol L<sup>-1</sup>. Linear plots were obtained for ln(C<sub>0</sub>/C) versus irradiation time as shown in **Figure 6.2** (using 1-CoFe<sub>2</sub>O<sub>4</sub>/PS as an example), that being an indication that all the reactions using each of the modified fibers follow pseudo first order reaction kinetics.

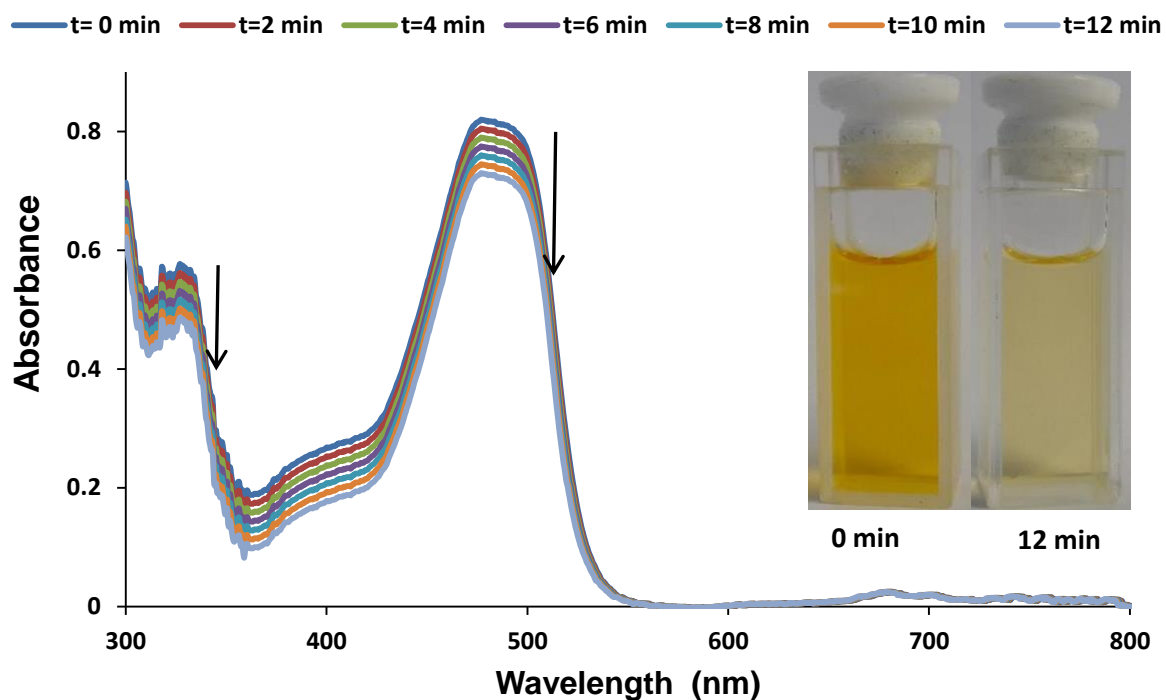


**Figure 6.1:** Absorption spectral changes of  $4.80 \times 10^{-5} \text{ molL}^{-1}$  OG solution during visible light photocatalysis using **1**-CoFe<sub>2</sub>O<sub>4</sub>/PS in water with pH 7.4 after 2 minute irradiation intervals. Insert = change in colour of OG solution after fiber has been removed.

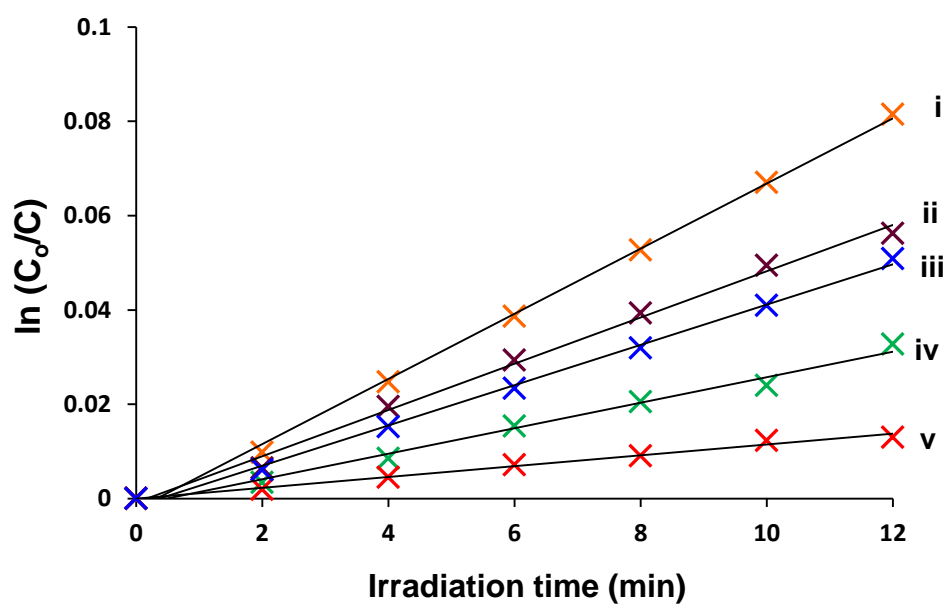


**Figure 6.2:** Pseudo first order kinetics plots for degradation of OG; i.  $1.80 \times 10^{-5}$ , ii.  $3.30 \times 10^{-5}$ , iii.  $4.60 \times 10^{-5}$ , iv.  $9.10 \times 10^{-5}$  and v.  $2.65 \times 10^{-4} \text{ molL}^{-1}$  using **1**-CoFe<sub>2</sub>O<sub>4</sub>/PS at pH7.4.

The initial rates of photodegradation of OG increased, while  $k_{\text{obs}}$  decreased, with an increase in the OG concentration, **Table 6.1**. Similar results have been observed before [70,76]. The increase in rates of reaction with increase in its concentration can be attributed to there being better collision between the reactant molecules and hence better degradation reactions. The initial rates were found to be greater for the conjugates compared to their respective Pcs while the  $\text{CoFe}_2\text{O}_4$  nanoparticles showed the least photocatalytic activity. This is not surprising because although ferrites have been reported to possess photocatalytic activity, the addition of oxidants such as  $\text{H}_2\text{O}_2$  is often required to enhance their ability to produce ROS and thus photocatalytic ability. This is because as explained above, the  $e^-/h^+$  pairs tend to recombine quickly, reducing the photocatalytic ability of the ferrites [9]. In this work, enhancement of the photocatalytic abilities of ferrites is attempted by conjugation of the MNPs to Pcs thereby promoting their synergistic interaction. It has also been reported that the size of the nanoparticle, optimising its loading relative to the pollutant (OG in this case), mechanical and heat treatment also enhance their photocatalytic efficiencies [9,163]. In this work the larger (12 nm from DLS)  $\text{CoFe}_2\text{O}_4\text{-COOH}$ , showed slightly better rates of degradation than the smaller (9 nm from DLS)  $\text{CoFe}_2\text{O}_4\text{-NH}_2$  (**Table 3.2**). It was also observed that **2/PS** and **2- $\text{CoFe}_2\text{O}_4$ /PS** have greater degradation rates compared to **1/PS** and **1- $\text{CoFe}_2\text{O}_4$ /PS** respectively, **Table 6.1**. This is therefore an indication that the  $\Phi_{\Delta}$  is directly related to the photocatalytic ability of the complexes as **2/PS** has a higher  $\Phi_{\Delta}$  than **1/PS** (0.40 and 0.20 respectively) and **2- $\text{CoFe}_2\text{O}_4$ /PS** has a higher  $\Phi_{\Delta}$  than **1- $\text{CoFe}_2\text{O}_4$ /PS** (0.63 and 0.60 respectively, **Table 5.1**).

The Langmuir–Hinshelwood kinetic model has been successfully applied in solid-liquid reactions, and was employed in the degradation of OG using the modified fibers as that also

models heterogeneous photocatalytic reactions. The Langmuir-Hinshelwood model was used to describe the relationship between the initial rate of degradation of OG and the corresponding initial concentration and is expressed as shown in **Equation 6.1**:

$$\frac{1}{r_0} = \frac{1}{kK_A} \frac{1}{C_0} + \frac{1}{k} \quad (6.1)$$

where  $r_0$  is the initial photocatalytic degradation rate ( $\text{mol L}^{-1} \text{min}^{-1}$ ),  $C_0$  is the initial concentration of OG,  $k$  is the apparent reaction rate constant ( $\text{mol L}^{-1} \text{min}^{-1}$ ) and  $K_A$  is the adsorption coefficient. Using data from the degradation,  $1/r_0$  was plotted against  $1/C_0$ . Linear fits with non-zero intercepts were obtained showing that the photodegradation of OG using the modified PS fibers obeys the Langmuir–Hinshelwood kinetics model, **Figure 6.3** (using **1-CoFe<sub>2</sub>O<sub>4</sub>/PS** and **2-CoFe<sub>2</sub>O<sub>4</sub>/PS** as examples).

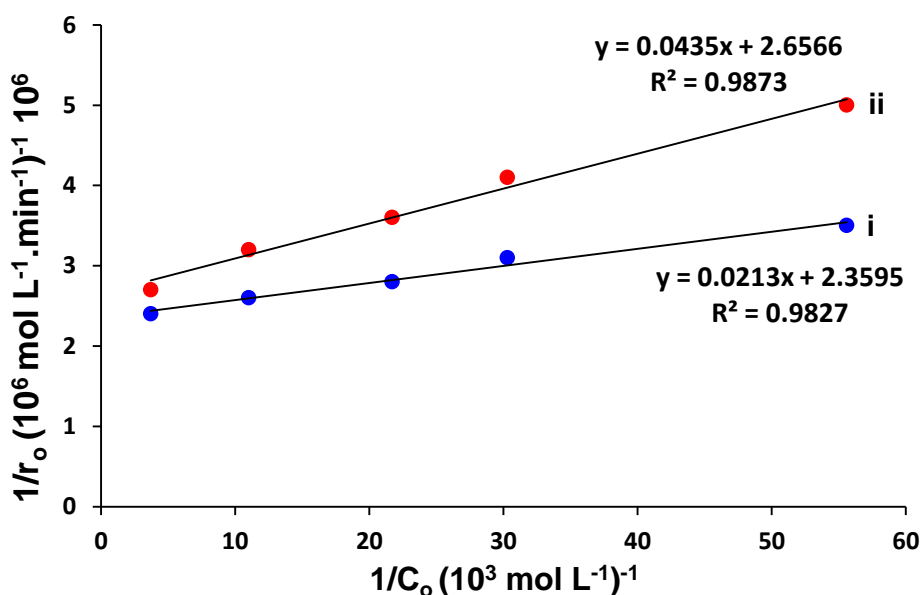


**Figure 6.3:** Plots of the reciprocal of initial reaction rate versus the reciprocal of the initial concentration for photodegradation of OG using; i. **2-CoFe<sub>2</sub>O<sub>4</sub>/PS** and ii. **1-CoFe<sub>2</sub>O<sub>4</sub>/PS** as catalysts at pH 7.4.

The Langmuir–Hinshelwood kinetics data is listed in **Table 6.2**. The value of  $k$  was obtained from the  $y$ -intercept, while  $K_A$  was obtained from the slope of the line. Obtained results show that both  $k$  and  $K_A$  increased for the conjugates relative to their respective Pcs and MNPs. This therefore proves that the catalytic activity and adsorption of OG on the catalysts favours the Pc-MNP conjugates in fibers than just the Pcs or MNP in the fibers, **2-CoFe<sub>2</sub>O<sub>4</sub>/PS** being the best and the MNPs being the worst.

**Table 6.1:** Rates, rate constants ( $k_{\text{obs}}$ ) and half-lives ( $t_{1/2}$ ) of various initial concentrations of OG at pH 7.4. Values in brackets are for the corresponding conjugates: **1**-CoFe<sub>2</sub>O<sub>4</sub>/PS and **2**-CoFe<sub>2</sub>O<sub>4</sub>/PS respectively.

[OG] × 10 <sup>-5</sup> (mol L <sup>-1</sup> )	$k_{\text{obs}}$ (min <sup>-1</sup> )				Initial Rate (10 <sup>-7</sup> mol L <sup>-1</sup> min <sup>-1</sup> )				Half-life (min)			
	1/PS	2/PS	CoFe <sub>2</sub> O <sub>4</sub> - NH <sub>2</sub> /PS	CoFe <sub>2</sub> O <sub>4</sub> - COOH/PS	1/PS	2/PS	CoFe <sub>2</sub> O <sub>4</sub> - NH <sub>2</sub> /PS	CoFe <sub>2</sub> O <sub>4</sub> - COOH/PS	1/PS	2/PS	CoFe <sub>2</sub> O <sub>4</sub> - NH <sub>2</sub> /PS	CoFe <sub>2</sub> O <sub>4</sub> - COOH/PS
<b>1.80</b>	0.0069 (0.0110)	0.0084 (0.0160)	0.0021 (0.110)	0.0027 (0.0160)	1.24 (1.98)	1.51 (2.88)	0.38 (1.98)	0.49 (2.88)	100 (63)	83 (43)	330 (63)	257 (43)
<b>3.30</b>	0.0049 (0.0074)	0.0058 (0.0098)	0.0018 (0.0074)	0.0021 (0.0098)	1.62 (2.44)	1.91 (3.23)	0.59 (2.44)	0.69 (3.23)	141 (94)	119 (71)	385 (94)	330 (71)
<b>4.80</b>	0.0043 (0.0060)	0.0052 (0.0077)	0.0015 (0.0060)	0.0018 (0.0077)	1.98 (2.76)	2.39 (3.54)	0.80 (2.76)	0.95 (3.54)	161 (116)	133 (90)	462 (116)	385 (90)
<b>9.10</b>	0.0027 (0.0034)	0.0032 (0.0042)	0.0010 (0.0034)	0.0013 (0.0042)	2.46 (3.09)	2.91 (3.82)	0.91 (3.09)	1.18 (3.82)	257 (204)	217 (165)	693 (204)	533 (165)
<b>26.5</b>	0.0011 (0.0014)	0.0013 (0.0016)	0.0005 (0.0014)	0.0006 (0.0016)	2.92 (3.71)	3.32 (4.24)	1.35 (3.71)	1.62 (4.24)	630 (495)	533 (433)	1386 (495)	1155 (433)

**Table 6.2:** Langmuir–Hinshelwood parameters for the photodegradation of OG in water (pH 7.4) using **1**/PS, **2**/PS, CoFe<sub>2</sub>O<sub>4</sub>-NH<sub>2</sub>/PS, CoFe<sub>2</sub>O<sub>4</sub>-COOH/PS, **1**-CoFe<sub>2</sub>O<sub>4</sub>/PS and **2**-CoFe<sub>2</sub>O<sub>4</sub>/PS as photocatalysts.

<b>Catalyst</b>	<b>k</b> (mol L <sup>-1</sup> min <sup>-1</sup> )	<b>K<sub>A</sub></b> (mol <sup>-1</sup> L)	<b>R<sup>2</sup></b>
<b>1</b> /PS	3.16 x 10 <sup>-7</sup>	3.64 x 10 <sup>4</sup>	0.9897
<b>2</b> /PS	3.66 x 10 <sup>-7</sup>	3.92 x 10 <sup>4</sup>	0.9854
CoFe <sub>2</sub> O <sub>4</sub> -NH <sub>2</sub> /PS	1.84 x 10 <sup>-7</sup>	2.54 x 10 <sup>4</sup>	0.9879
CoFe <sub>2</sub> O <sub>4</sub> -COOH/PS	1.73 x 10 <sup>-7</sup>	2.16 x 10 <sup>4</sup>	0.9960
<b>1</b> -CoFe <sub>2</sub> O <sub>4</sub> /PS	3.76 x 10 <sup>-7</sup>	6.30 x 10 <sup>4</sup>	0.9873
<b>2</b> -CoFe <sub>2</sub> O <sub>4</sub> /PS	4.24 x 10 <sup>-7</sup>	1.15 x 10 <sup>5</sup>	0.9827

### 6.1.2 Application of Polyamide-6 (PA-6) fibers

Complexes **4** and **6**, CoFe<sub>2</sub>O<sub>4</sub>-NH<sub>2</sub> MNPs as well as their respective conjugates were electrospun in polyamide-6 to generate **4**/PA-6, **6**/PA-6, **4**-CoFe<sub>2</sub>O<sub>4</sub>/PA-6, **6**-CoFe<sub>2</sub>O<sub>4</sub>/PA-6 and CoFe<sub>2</sub>O<sub>4</sub>-NH<sub>2</sub>/PA-6, followed by their application in the photooxidation of OG. Comparison on the photocatalytic efficiencies of the photocatalysts is based on complex **4** being symmetrical and water soluble and complex **6** being usymmetrical and insoluble in water.

### 6.1.2.1 UV-vis spectra

Photodegradation efficiencies of the functionalised fibers (CoFe<sub>2</sub>O<sub>4</sub>-NH<sub>2</sub>/PA-6, **4**/PA-6, **6**/PA-6, **4**-CoFe<sub>2</sub>O<sub>4</sub>/PA-6 and **6**-CoFe<sub>2</sub>O<sub>4</sub>/PA) were evaluated by again spectroscopically monitoring the degradation of OG in the presence of the photocatalysts and laser irradiations of ten minutes. Similar degradation conditions were employed and hence similar spectra were obtained as the one shown in **Figure 6.1**.

### 6.1.2.2 Kinetics Studies

The photocatalysts were applied in the degradation of five concentrations of OG;  $2.95 \times 10^{-5}$  mol L<sup>-1</sup>,  $4.31 \times 10^{-5}$  mol L<sup>-1</sup>,  $5.53 \times 10^{-5}$  mol L<sup>-1</sup>,  $7.53 \times 10^{-5}$  mol L<sup>-1</sup> and  $1.08 \times 10^{-4}$  mol L<sup>-1</sup>. The initial rates of photodegradation of OG increased, while  $k_{obs}$  decreased, with an increase in the OG concentration, with both values being greatest for the conjugates in the fibers (**4**-CoFe<sub>2</sub>O<sub>4</sub>/PA- and **6**-CoFe<sub>2</sub>O<sub>4</sub> /PA-6) compared to their respective Pcs in fibers (**4**/PA-6 and **6**/PA-6, **Table 6.3**).

For the same reasons mentioned before, fibers functionalised with the CoFe<sub>2</sub>O<sub>4</sub>-NH<sub>2</sub> MNPs were found to possess the lowest photocatalytic activity. No conclusive comparison could be made on the rates of degradation of OG using the PS and PA-6 fibers because of different OG concentrations used, different irradiation times (two minutes irradiations for former and ten minutes for latter) and different amounts of incorporated catalysts (120 mg for former and 40 mg for latter) that were used in each of the fibers.



**Table 6.3:** Rates, rate constants ( $k_{\text{obs}}$ ) and half-lives ( $t_{1/2}$ ) of various initial concentrations of OG at pH 7.4. Values in brackets are for the electrospun Pc-MNP conjugates; **4**-CoFe<sub>2</sub>O<sub>4</sub>/PA-6 and **6**-CoFe<sub>2</sub>O<sub>4</sub>/PA-6.

[OG] $\times 10^{-5}$ (mol L <sup>-1</sup> )	$k_{\text{obs}}$ (min <sup>-1</sup> )			Rate (10 <sup>-6</sup> mol L <sup>-1</sup> min <sup>-1</sup> )			$t_{1/2}$ (min)		
	CoFe <sub>2</sub> O <sub>4</sub> -NH <sub>2</sub> /PA-6	4/PA-6	6/PA-6	CoFe <sub>2</sub> O <sub>4</sub> -NH <sub>2</sub> /PA-6	4/PA-6	6/PA-6	CoFe <sub>2</sub> O <sub>4</sub> -NH <sub>2</sub> /PA-6	4/PA-6	6/PA-6
<b>2.95</b>	0.0040	0.0419 (0.0492)	0.0425 (0.0544)	0.118	1.24 (1.45)	1.25 (1.60)	173.3	16.54 (14.09)	16.31 (12.74)
<b>4.31</b>	0.0029	0.0307 (0.0362)	0.0312 (0.0383)	0.125	1.32 (1.56)	1.34 (1.65)	239.0	22.57 (19.14)	22.21 (18.09)
<b>5.53</b>	0.0025	0.0248 (0.0291)	0.0248 (0.0307)	0.135	1.37 (1.61)	1.37 (1.70)	277.2	27.94 (23.81)	27.94 (22.57)
<b>7.53</b>	0.0019	0.0183 (0.0220)	0.0186 (0.0231)	0.143	1.38 (1.66)	1.40 (1.74)	364.7	37.87 (31.50)	37.26 (30.00)
<b>10.8</b>	0.0014	0.0133 (0.0156)	0.0135 (0.0167)	0.151	1.44 (1.68)	1.46 (1.80)	495.0	52.11 (44.42)	51.33 (41.50)

Similar plots as those seen in **Figure 6.2** were obtained when  $\ln (C_0/C)$  versus irradiation time were plotted, this therefore being an indication that photodegradation of OG using the functionalised fibers (**4**/PA-6, **6**/PA-6, **4-CoFe<sub>2</sub>O<sub>4</sub>**/PA-6, **6-CoFe<sub>2</sub>O<sub>4</sub>**/PA-6 and CoFe<sub>2</sub>O<sub>4</sub>-NH<sub>2</sub>/PA-6) follows pseudo first order kinetics.

The Langmuir–Hinshelwood kinetics model (**Equation 6.1**) was applied and plots of  $1/r_0$  against  $1/C_0$  gave linear fits with non-zero intercepts were obtained, similar to those in **Figure 6.3**. The results therefore show that the photodegradation of OG using the functionalised fibers reported herein obeys the Langmuir–Hinshelwood kinetics model. The obtained Langmuir–Hinshelwood kinetics data is listed in **Table 6.4**. The obtained results show that both  $k$  and  $K_A$  were greater for the Pc-MNP conjugates relative to their respective Pcs and MNPs. The obtained results therefore prove that the catalytic activity and adsorption of OG on the catalysts favours the Pc-MNP conjugates in fibers than just the Pcs or MNP in the fibers, **6-CoFe<sub>2</sub>O<sub>4</sub>**/PA-6 (with the highest singlet oxygen) being the best and the CoFe<sub>2</sub>O<sub>4</sub>-NH<sub>2</sub>/PA-6 being the worst.

**Table 6.4:** Langmuir–Hinshelwood parameters for the photodegradation of OG in water (pH 7.4) using  $\text{CoFe}_2\text{O}_4\text{-NH}_2$ , **4**/PA-6, **6**/PA-6, **4-CoFe<sub>2</sub>O<sub>4</sub>**/PA-6 and **6-CoFe<sub>2</sub>O<sub>4</sub>**/PA-6 as photocatalysts.

Catalyst	<b>k</b> ( $\text{mol L}^{-1} \text{min}^{-1}$ ) $10^{-6}$	<b>K<sub>A</sub></b> ( $\text{mol}^{-1} \text{L}$ )	<b>R<sup>2</sup></b>
$\text{CoFe}_2\text{O}_4\text{-NH}_2/\text{PA-6}$	1.67	$8.21 \times 10^4$	0.9673
<b>4</b> /PA-6	1.52	$1.37 \times 10^5$	0.9802
<b>6</b> /PA-6	1.54	$1.45 \times 10^5$	0.9866
<b>4-CoFe<sub>2</sub>O<sub>4</sub></b> /PA-6	1.81	$1.64 \times 10^5$	0.9874
<b>6-CoFe<sub>2</sub>O<sub>4</sub></b> /PA-6	1.87	$2.91 \times 10^5$	0.9647

## 6.2 Photooxidation of Methyl Orange (MO) with PA-6 fibers

### 6.2.1 UV-vis spectra

Using the same degradation conditions, the functionalised fibers (**4**/PA-6, **6**/PA-6, **4-CoFe<sub>2</sub>O<sub>4</sub>**/PA-6, **6-CoFe<sub>2</sub>O<sub>4</sub>**/PA-6 and  $\text{CoFe}_2\text{O}_4\text{-NH}_2/\text{PA-6}$ ) were applied on a different analyte, Methyl Orange (MO) for comparison and specificity purposes. There was an observed decrease in the intensity of the absorption peak at 464 nm for MO with irradiation intervals of ten minutes; **Figure 6.4** (using degradation with **4-CoFe<sub>2</sub>O<sub>4</sub>**/PA-6 as an example). Just as with OG, photodegradation was conducted at room temperature in unbuffered water with pH of 7.4. There was also observed fading in the color due to the oxidation of the azo bond as explained for OG.

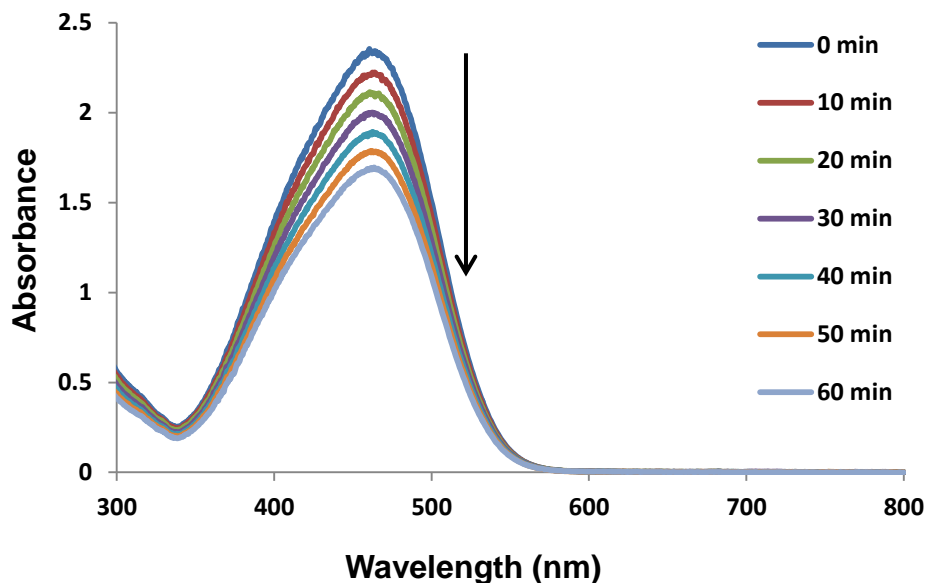


**Figure 6.4:** Absorption spectral changes of  $10.8 \times 10^{-5} \text{ mol L}^{-1}$  MO during visible light photocatalysis using **4**-CoFe<sub>2</sub>O<sub>4</sub>/PA-6 in water with irradiation intervals of 10 min, pH 7.4.

## 6.2.2 Kinetics Studies

The photocatalysts were applied in the degradation of five concentrations of MO;  $2.95 \times 10^{-5} \text{ mol L}^{-1}$ ,  $4.31 \times 10^{-5} \text{ mol L}^{-1}$ ,  $5.53 \times 10^{-5} \text{ mol L}^{-1}$ ,  $7.53 \times 10^{-5} \text{ mol L}^{-1}$  and  $1.08 \times 10^{-4} \text{ mol L}^{-1}$  just as with OG. Similar plots as those shown in **Figure 6.2** were obtained when  $\ln(C_0/C)$  versus irradiation time were plotted, an indication that MO photodegradation using **4**/PA-6, **6**/PA-6, **4**-CoFe<sub>2</sub>O<sub>4</sub>/PA-6, **6**-CoFe<sub>2</sub>O<sub>4</sub>/PA-6 and CoFe<sub>2</sub>O<sub>4</sub>-NH<sub>2</sub>/PA-6 also follows pseudo first order kinetics. However the obtained results show that the degradation of MO is not agreement with the Langmuir–Hinshelwood kinetics model. Unlike OG, the initial rates of photodegradation and rate constants ( $k_{\text{obs}}$ ) were found to decrease, and the half-lives increased with increase in the MO concentration (**Table 6.5**). Similar results have been observed before [69,72] and reasons as to why the different dyes react differently is of interest and will be studied further in future. The rates of photodegradation and  $k_{\text{obs}}$  were

found to be greatest for the conjugates in the fibers; **4**-CoFe<sub>2</sub>O<sub>4</sub>/PA- and **6**-CoFe<sub>2</sub>O<sub>4</sub>/PA-6 than their respective Pcs in fibers; **4**/PA-6 and **6**/PA-6. The results therefore confirm that the  $\Phi_{\Delta}$  is directly related to the photocatalytic efficiencies of the photocatalysts. In the degradation of both dyes, the CoFe<sub>2</sub>O<sub>4</sub>-NH<sub>2</sub>/PA-6 were found to possess the lowest photocatalytic activity for the same reasons explained for CoFe<sub>2</sub>O<sub>4</sub>-NH<sub>2</sub>/PS.

Comparison of the degradation efficiencies of the functionalised fibers in the degradation the same concentrations of both pollutants (OG and MO) at the same degradation conditions shows that all the photocatalysts possessed better activity in the degradation of OG than MO. This can be attributed to parameters such as pH as it has been reported before that the degradation of MO is enhanced at pH values in the range 2-3 [164,165]. However pH 7.4 was used in this study for efficient comparison of degradation efficiencies between OG and MO under the same conditions. Parameters such as catalyst loading relative to dye concentration could have also affected the obtained results.

**Table 6.5:** Rates, rate constants ( $k_{\text{obs}}$ ) and half-lives ( $t_{1/2}$ ) of various initial concentrations of MO using the functionalised fibers;  $\text{CoFe}_2\text{O}_4\text{-NH}_2/\text{PA-6}$ , **4**/ $\text{PA-6}$ , and **6**/ $\text{PA-6}$  at pH 7.4. Values in brackets are for the electrospun Pc-MNP conjugates; **4**- $\text{CoFe}_2\text{O}_4/\text{PA-6}$  and **6**- $\text{CoFe}_2\text{O}_4/\text{PA-6}$ .

[MO] $\times 10^{-5}$ (mol L <sup>-1</sup> )	$k_{\text{obs}}$ (min <sup>-1</sup> )			Rate (10 <sup>-7</sup> mol L <sup>-1</sup> min <sup>-1</sup> )			$t_{1/2}$ (min)		
	$\text{CoFe}_2\text{O}_4\text{-NH}_2/\text{PA-6}$	<b>4</b> / $\text{PA-6}$	<b>6</b> / $\text{PA-6}$	$\text{CoFe}_2\text{O}_4\text{-NH}_2/\text{PA-6}$	<b>4</b> / $\text{PA-6}$	<b>6</b> / $\text{PA-6}$	$\text{CoFe}_2\text{O}_4\text{-NH}_2/\text{PA-6}$	<b>4</b> / $\text{PA-6}$	<b>6</b> / $\text{PA-6}$
<b>2.95</b>	0.0035	0.0113 (0.0155)	0.0115 (0.0198)	1.03	3.33 (4.57)	3.39 (5.84)	198.0	61.33 (44.71)	60.26 (35.00)
<b>4.31</b>	0.0020	0.0075 (0.0104)	0.0075 (0.0133)	0.862	3.23 (4.48)	3.23 (5.73)	346.5	92.40 (66.63)	92.40 (52.11)
<b>5.53</b>	0.0014	0.0054 (0.0075)	0.0056 (0.0096)	0.774	2.98 (4.15)	3.10 (5.31)	495.0	128.3 (92.40)	123.8 (72.19)
<b>7.53</b>	0.0013	0.0031 (0.0042)	0.0033 (0.0054)	0.979	2.33 (3.16)	2.48 (4.07)	533.1	223.5 (165.0)	210.0 (128.3)
<b>10.8</b>	0.0003	0.0014 (0.0019)	0.0013 (0.0024)	0.324	1.51 (2.05)	1.40 (2.59)	2310	495.0 (364.7)	533.1 (288.8)

### 6.2.3 Reusability studies

As explained before, the essence of conjugating the Pcs to the  $\text{CoFe}_2\text{O}_4$  MNPs and electrospinning the composites was to design retrievable and hence reusable photocatalysts. SEM analysis and UV-vis spectroscopy of the fibers after application in photooxidation were run (using **6**- $\text{CoFe}_2\text{O}_4$ -PA-6 as an example). This was to check if the Pc remained within the fiber even after application and to check if the topography of the fibers was not altered with application.

As shown in **Figure 6.5**, the topography of the fiber is maintained while the solid state UV-vis spectrum (**Figure 6.5**) shows a slight decrease in the absorbance of **6**- $\text{CoFe}_2\text{O}_4$ /PA-6 fiber relative to when it was applied initially (**Figure 5.6 (B)**). There is also an observed band between 400-500 nm which could possibly be the adsorbed MO on the surface of the fiber.

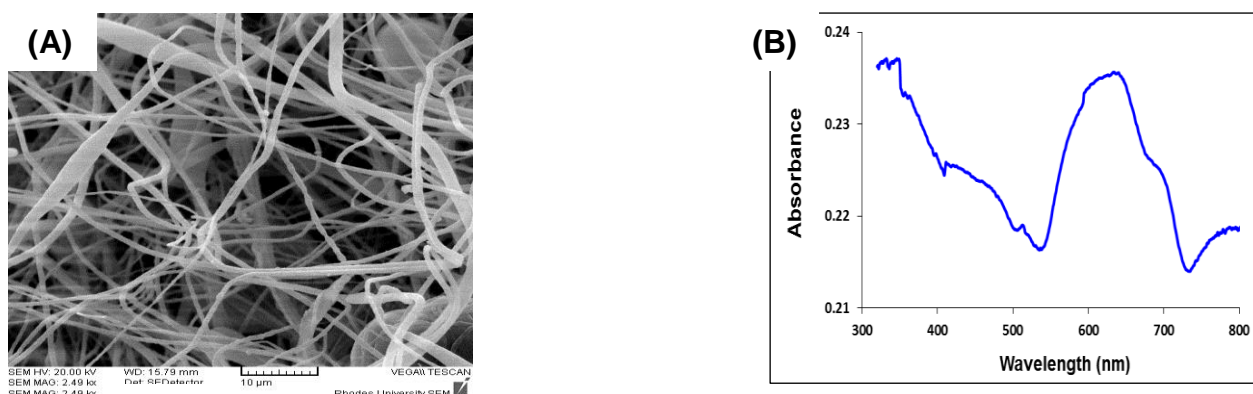


**Figure 6.5:** (A) SEM image of a used **6**- $\text{CoFe}_2\text{O}_4$ /PA-6 fiber and (B) Solid state UV-vis spectrum of **6**- $\text{CoFe}_2\text{O}_4$ /PA-6.

From the results obtained from characterising the used fibers, it can be concluded that since the Pc remains intact in the fiber after use, the fiber can be reused for numerous phototoxidation experiments.

### 6.3 Dual photooxidation of MO and photoreduction of Cr(VI)

Since Pc-MNP based composites were found to exhibit photocatalytic behaviour even when embedded in polymer fibers, their photocatalytic efficiencies when used as colloids in solution were studied too. Pc complexes that are not water soluble (using complexes **2** and **7** as examples) were used so no increased pollution due to the photocatalysts would be observed. Complexes **2** and **7** were conjugated to glutathione capped  $\text{CoFe}_2\text{O}_4$  MNPs ( $\text{CoFe}_2\text{O}_4$ -GSH MNPs) and their photocatalytic efficiencies evaluated. The photooxidation properties of the composites were evaluated using MO as the model compound. Their photoreduction efficiencies were also evaluated, using Cr(VI) as a model compound with the aim of creating bifunctional composites that facilitate simultaneous photooxidation and photoreduction. As mentioned before, the reason the MNPs were capped with glutathione is because in addition to it having the appropriate terminal groups for amide bond formation with the Pc complexes, glutathione has itself been reported to possess photoreduction ability for Cr(VI) before [166, 167]. The effectiveness of the covalent linkage in enhancing the photocatalytic ability of the conjugates is also studied. This is done by preparing a mixture of the GSH- $\text{CoFe}_2\text{O}_4$  MNPs and complexes **2** and **7** respectively with no amide bond formation resulting in **2**- $\text{CoFe}_2\text{O}_4$ -GSH (mix) and **7**- $\text{CoFe}_2\text{O}_4$  (mix), respectively.



### 6.3.1 Photooxidation of Methyl Orange (MO)

#### 6.3.1.1 UV-vis spectra

Photooxidation efficiencies of CoFe<sub>2</sub>O<sub>4</sub>-GSH MNPs, complexes **2** and **7**, **2**-CoFe<sub>2</sub>O<sub>4</sub>-GSH, **7**-CoFe<sub>2</sub>O<sub>4</sub>, **2**-CoFe<sub>2</sub>O<sub>4</sub>-GSH (mix) and **7**-CoFe<sub>2</sub>O<sub>4</sub> (mix) were evaluated. This was done by spectroscopically monitoring the photodegradation of MO upon exposure to the compounds and laser irradiations. Photooxidation was conducted at room temperature with pH of 2.75 because as mentioned before, the photodegradation of MO is enhanced at pH values in the range 2-3 [164,165]. Evidently the electronic absorption of MO is pH dependent as there was an observed decrease of intensity of the absorption peak at 506 nm with laser irradiation at two minute intervals (**Figure 6.6**, using **2**-CoFe<sub>2</sub>O<sub>4</sub>-GSH as an example) unlike the previously observed decrease at 464 nm (**Figure 6.4**, pH 7.4). Irradiation intervals of 10 minutes were used to achieve efficient degradation at pH 7.4 (**Figure 6.4**) as opposed to the 2 minutes irradiations at pH 2.75 (**Figure 6.6**). The peak at 506 nm corresponding to the azo bond decreases in intensity as the sample is irradiated in the presence of the **2**-CoFe<sub>2</sub>O<sub>4</sub>-GSH while the bands below 330 nm on the other hand increased in intensity. The latter bands are due to the benzene rings [168,169]. The obtained spectra therefore suggest that the benzene rings remain intact and are not degraded during the photooxidation process unlike in **Figure 6.6**. There was also observed fading of the solution colour for the same reasons mentioned before for OG. Since the Pc complexes used for the study are not water soluble, there is no observed Pc Q band in the degradation spectra (**Figure 6.6**).

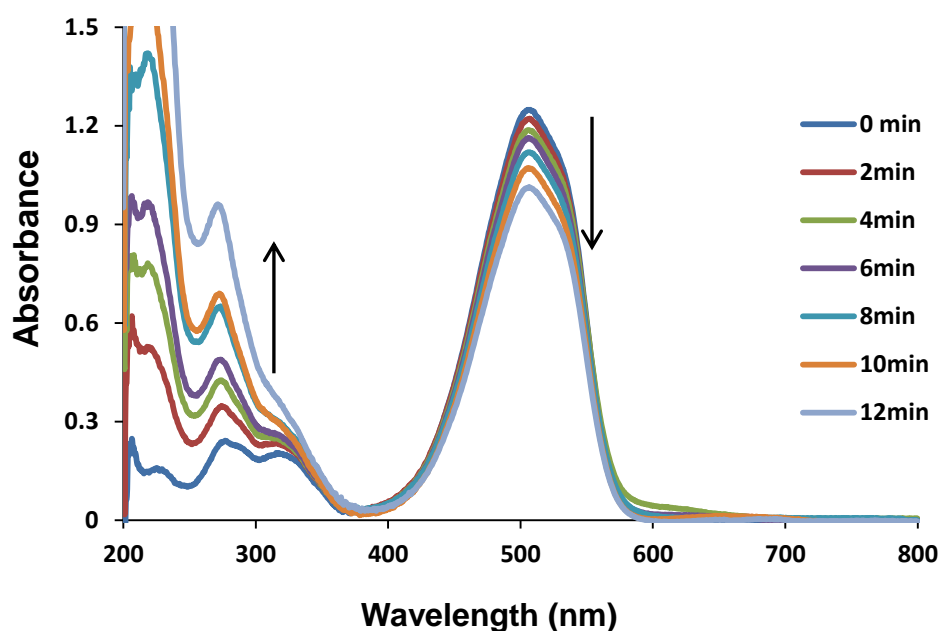


**Figure 6.6:** Electronic absorption spectral changes of  $2.67 \times 10^{-5} \text{ mol L}^{-1}$  MO solution during visible light photocatalysis using **2**-CoFe<sub>2</sub>O<sub>4</sub>-GSH in water with irradiation intervals of 2 min, pH 2.75.

### 6.3.1.2 Kinetics studies

The photocatalysts were applied in the degradation of five concentrations of MO;  $1.36 \times 10^{-5} \text{ mol L}^{-1}$ ,  $1.85 \times 10^{-5} \text{ mol L}^{-1}$ ,  $2.13 \times 10^{-5} \text{ mol L}^{-1}$ ,  $2.67 \times 10^{-5} \text{ mol L}^{-1}$  and  $3.40 \times 10^{-5} \text{ mol L}^{-1}$  with a catalyst loading of 1.5 mg/mL solution. Similar plots as those shown in **Figure 6.2** were obtained when  $\ln(C_0/C)$  versus irradiation time were plotted, an indication that MO photodegradation using complexes **2** and **7**, **2**-CoFe<sub>2</sub>O<sub>4</sub>-GSH, **2**-CoFe<sub>2</sub>O<sub>4</sub>-GSH (mix), **7**-CoFe<sub>2</sub>O<sub>4</sub> and **7**-CoFe<sub>2</sub>O<sub>4</sub> (mix) also follow pseudo first order kinetics. The initial rates and rate constants ( $k_{\text{obs}}$ ) for the photodegradation of MO decreased (while the half-lives increased) with an increase in the MO concentration, **Table 6.6**. Both values were found to be approximately similar for **2**-CoFe<sub>2</sub>O<sub>4</sub>-GSH and **7**-CoFe<sub>2</sub>O<sub>4</sub>, with both conjugates showing larger values than for complexes **2** and **7** and the mixed composites (**2**-CoFe<sub>2</sub>O<sub>4</sub>-GSH (mix)

and **7**-CoFe<sub>2</sub>O<sub>4</sub> (mix)). The conjugates with amide bond linkage (**2**-CoFe<sub>2</sub>O<sub>4</sub>-GSH and **7**-CoFe<sub>2</sub>O<sub>4</sub>) showed better photocatalytic activity in the degradation of MO than **2**-CoFe<sub>2</sub>O<sub>4</sub>-GSH (mix) and **7**-CoFe<sub>2</sub>O<sub>4</sub> (mix) (no amide bond). This could be due to **2**-CoFe<sub>2</sub>O<sub>4</sub>-GSH and **7**-CoFe<sub>2</sub>O<sub>4</sub> having higher singlet oxygen quantum yields (0.62 and 0.65 respectively) than **2**-CoFe<sub>2</sub>O<sub>4</sub>-GSH (mix) and **7**-CoFe<sub>2</sub>O<sub>4</sub> (mix) (0.58 and 0.50 respectively, **Table 4.1**) even though in DMSO and not as colloids in water.

The CoFe<sub>2</sub>O<sub>4</sub>-GSH MNPs on the other hand were found to have negligible photocatalytic activity unlike the CoFe<sub>2</sub>O<sub>4</sub>-NH<sub>2</sub> and CoFe<sub>2</sub>O<sub>4</sub>-COOH MNPs. This could possibly be an indication that the functionalization on the MNPs does affect the recombination of the e<sup>-</sup>/h<sup>+</sup> pairs, possibly enhancing or reducing their photocatalytic ability. When the photocatalysts were employed in the absence of irradiation and absence of oxygen (i.e. nitrogen purged solutions), no UV-vis spectral changes were observed, an indication that light and molecular oxygen are prerequisites in the degradation process.

**Table 6.6:** Rate, rate constant ( $k_{\text{obs}}$ ) and half-lives ( $t_{1/2}$ ) of various initial concentrations of MO using complexes **2** and **7**, **2-CoFe<sub>2</sub>O<sub>4</sub>-GSH** and **7-CoFe<sub>2</sub>O<sub>4</sub>** at pH 2.75. Values in brackets are for **2-CoFe<sub>2</sub>O<sub>4</sub>-GSH** (mix) and **7-CoFe<sub>2</sub>O<sub>4</sub>** (mix) respectively.

[MO] × 10 <sup>-5</sup> (mol L <sup>-1</sup> )	$k_{\text{obs}}$ (min <sup>-1</sup> )				Rate (10 <sup>-7</sup> mol L <sup>-1</sup> min <sup>-1</sup> )				$t_{1/2}$ (min)			
	<b>2</b>	<b>2-CoFe<sub>2</sub>O<sub>4</sub>- GSH</b>	<b>7</b>	<b>7-CoFe<sub>2</sub>O<sub>4</sub></b>	<b>2</b>	<b>2-CoFe<sub>2</sub>O<sub>4</sub>- GSH</b>	<b>7</b>	<b>7-CoFe<sub>2</sub>O<sub>4</sub></b>	<b>2</b>	<b>2-CoFe<sub>2</sub>O<sub>4</sub>- GSH</b>	<b>7</b>	<b>7-CoFe<sub>2</sub>O<sub>4</sub></b>
<b>1.36</b>	0.132	0.221 (0.148)	0.136	0.221 (0.149)	17.9	30.1 (20.1)	18.6	30.1 (20.2)	5.25	3.13 (4.70)	5.08	3.14 (4.67)
<b>1.85</b>	0.0606	0.106 (0.0700)	0.0610	0.105 (0.0715)	11.2	19.6 (13.0)	11.2	19.5 (13.2)	11.4	6.56 (9.84)	11.4	6.57 (9.69)
<b>2.13</b>	0.0360	0.0629 (0.0419)	0.0380	0.0625 (0.0422)	7.67	13.4 (8.92)	8.09	13.3 (8.98)	19.3	11.0 (16.5)	18.2	11.1 (16.4)
<b>2.67</b>	0.0100	0.0254 (0.0169)	0.0103	0.0250 (0.0169)	2.67	6.78 (4.51)	2.75	6.68 (4.51)	69.3	27.3 (41.0)	67.3	27.7 (41.0)
<b>3.40</b>	0.0042	0.0093 (0.0062)	0.0042	0.0094 (0.0065)	1.43	3.16 (2.11)	1.43	3.20 (2.21)	165	74.5 (111)	165	73.7 (106)

## 6.3.2 Photoreduction of Hexavalent Chromium (Cr(VI))

### 6.3.2.1 UV-vis spectra

Photoreduction efficiencies of CoFe<sub>2</sub>O<sub>4</sub>-GSH MNPs, complexes **2** and **7**, **2**-CoFe<sub>2</sub>O<sub>4</sub>-GSH, **7**-CoFe<sub>2</sub>O<sub>4</sub>, **2**-CoFe<sub>2</sub>O<sub>4</sub>-GSH (mix) and **7**-CoFe<sub>2</sub>O<sub>4</sub> (mix) were evaluated. This was achieved by spectroscopically monitoring the behaviour of Cr(VI) in the presence of light and the photocatalysts, **Figure 6.7** (using **2**-CoFe<sub>2</sub>O<sub>4</sub>-GSH as an example). There was an observed decrease in two absorption peaks at 252 nm and 349 nm while there was an increase in the absorption peak at 450 nm. The spectral changes are typical of the reduction of Cr(VI) to Cr(III) (**170**), with the latter being less toxic. The absorbance of Cr(III) was taken (**Figure 6.7** (Insert)) so as to confirm that its spectrum matched that of the 450 nm peak observed in the photoreduction of Cr(VI). Photoreduction studies were conducted at a pH of 2.75 as it has been reported that the reduction of Cr(VI) has been enhanced at acidic pH ranges due to the fact that the net reaction in the photoreduction process consumes H<sup>+</sup> (**122,170,171**).

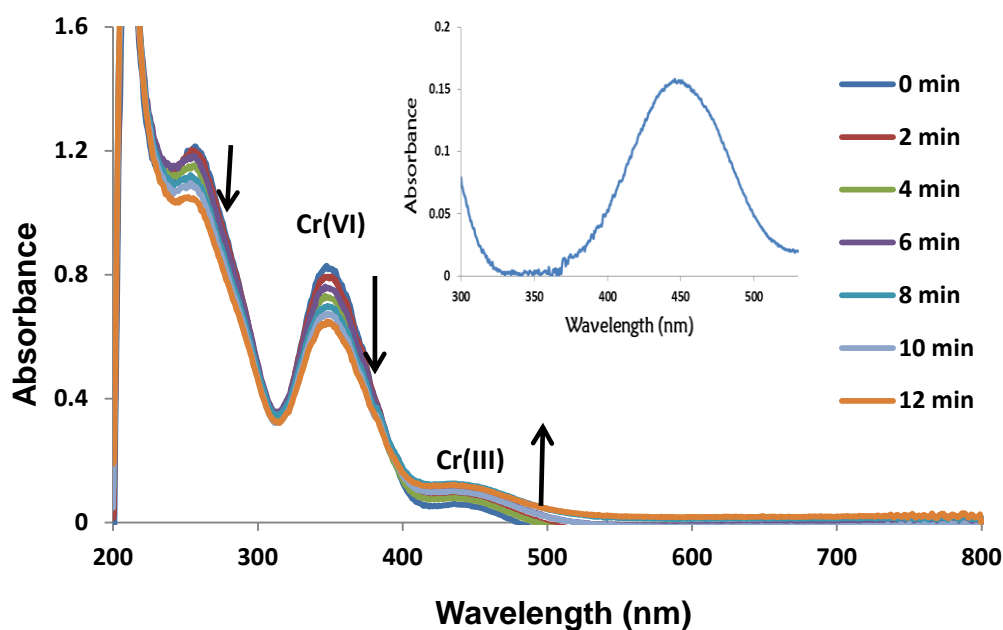


**Figure 6.7:** Absorption spectral changes of  $7.08 \times 10^{-4} \text{ mol L}^{-1}$  Cr(VI) solution using 2-CoFe<sub>2</sub>O<sub>4</sub>-GSH in water of pH 2.75 with irradiation intervals of 2 min.

With increased irradiation time and as well as in the concentration of Cr(VI), it was observed that the photoreduction was reversed as the Cr(III) peak decreased while the Cr(VI) peak increased, suggesting oxidation of Cr(III) back to Cr(VI). This was expected because the various ROS generated by the photocatalysts during the photolysis, may oxidize Cr(III) back to Cr(VI) [172] hence in this study MO was then used as a sacrificial molecule. MO suppresses the Cr(III) to Cr(VI) oxidation and reacts preferentially with the ROS and also prevents the possible degradation of complexes **2** and **7**. Spectral changes observed for Cr(VI) photoreduction in the presence of MO are shown in **Figure 6.8**. There was an observed decrease of spectral peaks corresponding to both Cr(VI) (349 nm) and MO (506 nm). The decrease in the Cr(VI) was more stable with photolysis time, unlike in the absence of MO. Due to the observed overlap between the Cr(III) and MO bands, increase in the

spectral peak for Cr(III) could not be monitored so photoreduction was monitored based on decrease of the Cr(VI) peak.

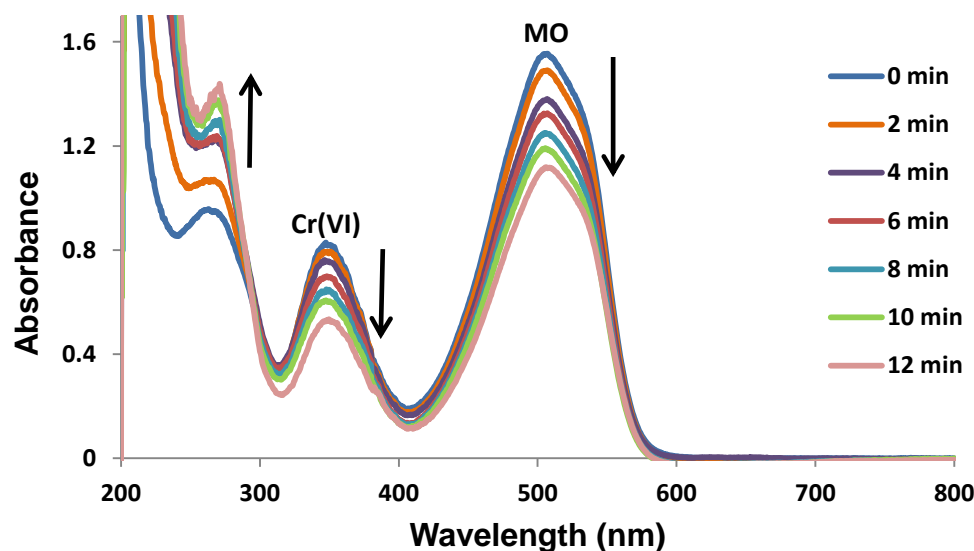


**Figure 6.8:** Absorption spectral changes of  $7.08 \times 10^{-4} \text{ mol L}^{-1}$  Cr(VI) solution in the presence of  $3.40 \times 10^{-5} \text{ mol L}^{-1}$  MO using 2-CoFe<sub>2</sub>O<sub>4</sub>-GSH in water of pH 2.75 with irradiation intervals of 2 min.

### 6.3.2.2 Kinetics studies

Photoreduction was conducted at room temperature at a pH = 2.75 with catalyst loading of 1.5 mg/mL and MO concentration of  $3.40 \times 10^{-5} \text{ mol L}^{-1}$ . The photoreduction was attempted for five concentrations of Cr(VI);  $7.08 \times 10^{-4}$ ,  $7.85 \times 10^{-4}$ ,  $8.54 \times 10^{-4}$ ,  $9.03 \times 10^{-4}$  and  $9.54 \times 10^{-4} \text{ mol L}^{-1}$ . When GSH-CoFe<sub>2</sub>O<sub>4</sub> MNPs were applied in the photoreduction of Cr(VI), no catalytic activity was observed as above for MO and for the same reasons. For reasons provided above, kinetic studies for the photoreduction of Cr(VI) were conducted in the presence of  $3.40 \times 10^{-5} \text{ mol L}^{-1}$  MO for each concentration of Cr(VI). The decrease of the peak at 349 was monitored. The photocatalysts showed a decrease in their rates of photoreduction with increase in the concentration of Cr(VI); **Table 6.7**. Simultaneous

photooxidation and photoreduction processes facilitated by Pc-MNP composites also follow pseudo first order kinetics with plots of  $\ln(C_0/C)$  versus irradiation time being linear such as in **Figure 6.2**.

Complexes **2** and **7** showed lower photocatalytic activity for the reduction of Cr(VI) when compared to when mixed or linked to MNPs. Interestingly the mixed composites showed marginally better photocatalytic activity (higher  $k_{obs}$  and rate) for the reduction of Cr(VI) compared to the linked conjugates, even though the latter had higher singlet oxygen quantum yields. The same amount sacrificial MO (which preferentially react with the hydroxide radicals, hence preventing the re-oxidation of Cr(III) to Cr(VI)) was used for both the mixed and linked composites in **Table 6.7**. It is also possible that if the amount of singlet oxygen is too high, it may also facilitate the photooxidation of Cr(III) back to Cr(VI) (provided that all the MO has been consumed) hence composites with high singlet oxygen might not be the best as observed in this study.

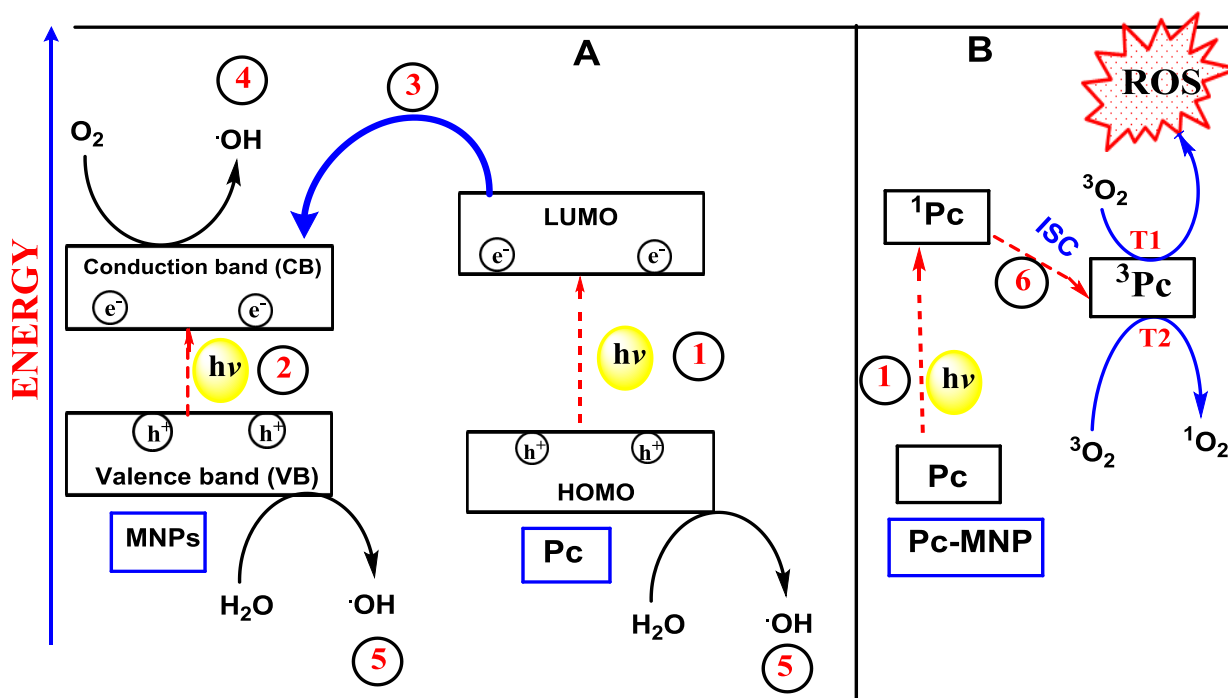


**Table 6.7:** Rates, rate constants ( $k_{\text{obs}}$ ) and half-lives ( $t_{1/2}$ ) of various initial concentrations of Cr(VI) (in the presence of  $3.40 \times 10^{-5} \text{ mol L}^{-1}$  MO using complexes **2** and **7**, **2-CoFe<sub>2</sub>O<sub>4</sub>-GSH** and **7-CoFe<sub>2</sub>O<sub>4</sub>**. Values in brackets are for **2-CoFe<sub>2</sub>O<sub>4</sub>-GSH** (mix) and **7-CoFe<sub>2</sub>O<sub>4</sub>** (mix) respectively.

[Cr(VI)] $\times 10^{-4}$ (mol L <sup>-1</sup> )	$k_{\text{obs}}$ (min <sup>-1</sup> )				Rate (10 <sup>-7</sup> mol L <sup>-1</sup> min <sup>-1</sup> )				$t_{1/2}$ (min)			
	<b>2</b>	<b>2-CoFe<sub>2</sub>O<sub>4</sub>- GSH</b>	<b>7</b>	<b>7-CoFe<sub>2</sub>O<sub>4</sub></b>	<b>2</b>	<b>2-CoFe<sub>2</sub>O<sub>4</sub>- GSH</b>	<b>7</b>	<b>7-CoFe<sub>2</sub>O<sub>4</sub></b>	<b>2</b>	<b>2-CoFe<sub>2</sub>O<sub>4</sub>- GSH</b>	<b>7</b>	<b>7-CoFe<sub>2</sub>O<sub>4</sub></b>
<b>7.08</b>	0.0309	0.103 (0.124)	0.0305	0.102 (0.103)	21.9	72.9 (87.4)	21.6	72.4 (72.9)	22.4	6.74 (5.61)	22.7	6.78 (6.72)
<b>7.85</b>	0.0156	0.0674 (0.0720)	0.0165	0.0660 (0.0685)	12.3	52.9 (56.5)	13.0	51.8 (53.8)	44.4	10.3 (9.63)	42.0	10.5 (10.1)
<b>8.54</b>	0.0084	0.0450 (0.0495)	0.0079	0.0425 (0.0465)	7.17	38.4 (42.3)	6.75	36.3 (39.7)	82.5	15.4 (14.0)	87.7	16.3 (14.9)
<b>9.03</b>	0.0038	0.0292 (0.033)	0.0035	0.0285 (0.0300)	3.43	26.4 (29.8)	3.16	25.7 (27.1)	182	23.7 (21.0)	198	24.3 (23.1)
<b>9.54</b>	0.0018	0.0097 (0.0099)	0.0019	0.0092 (0.0092)	1.71	9.25 (9.44)	1.81	8.78 (8.78)	385	71.4 (70.0)	365	75.3 (75.3)

## 6.4 Mechanism of photocatalysis of Pc-CoFe<sub>2</sub>O<sub>4</sub> MNP conjugates

It can be elucidated that photocatalysis of Pcs in the presence of CoFe<sub>2</sub>O<sub>4</sub> MNPs may occur in two ways, **Scheme 6.1 A and B**. Upon excitation with visible light, an electron-hole pair is formed in the highest occupied molecular orbital (HOMO) and lowest unoccupied molecular orbital (LUMO) of the Pc (route **1** in **Scheme 6.1 A**) [73,78]. In ferrites, upon exposure to visible light, an electron-hole pair is formed in the conduction band (CB) and valence band (VB) respectively (route **2** in **Scheme 6.1 A**). The electrons in the LUMO of the Pc are then injected into the conduction band of CoFe<sub>2</sub>O<sub>4</sub> MNPs (route **3** in **Scheme 6.1 A**). The photoelectrons can attack molecular oxygen to produce various ROS including hydroxyl radicals ( $\cdot\text{OH}$ ) (route **4** in **Scheme 6.1 A**) [171]. The photoholes possess highly oxidizing ability and can directly participate in oxidative degradation of organics or oxidise water to produce ROS including  $\cdot\text{OH}$  (route **5** in **Scheme 6.1 A**). The resultant ROS from both the photoelectrons and photoholes then facilitate photooxidation of organic dyes (MO and OG in this case). For photoreduction of Cr(VI) on the other hand, only the photoelectrons in the conduction band (CB) of the MNPs and LUMO of the Pc can be acquired by Cr(VI) thereby reducing it to Cr(III).



**Scheme 6.1:** The formation of ROS by photosensitization of  $\text{CoFe}_2\text{O}_4$  MNPs and Pcs upon excitation with visible light. HOMO = highest occupied molecular orbital, LUMO = lowest unoccupied molecular orbital, ISC= intersystem crossing. T1= Type 1 and T2= Type 2

A second possible mechanism (**Scheme 6.1 B**) involves the intersystem crossing (ISC) of the excited dye to the triplet state. The triplet state ( $^3\text{Pc}$ ) has a longer lifetime ( $\mu\text{s}$ ) than that of the excited singlet state ( $^1\text{Pc}$ ) (ns), enabling the Pc in the triplet excited state to react with molecular oxygen in two different ways, denoted T1 (Type 1) and T2 (Type 2) in **Scheme 6.1 B**. In the Type 1 reaction (T1), the Pc in the excited triplet state ( $^3\text{Pc}$ ) transfers an electron to molecular oxygen ( $^3\text{O}_2$ ) generating various ROS including hydroxyl radicals ( $\cdot\text{OH}$ ), peroxides ( $\text{H}_2\text{O}_2$ ) and hydroxide ions ( $\text{OH}^-$ ) [68] which have the ability to readily degrade organic pollutants. The Type 2 reaction (T2) on the other hand entails the transfer of energy from the Pc in triplet excited state ( $^3\text{Pc}$ ) to molecular oxygen ( $^3\text{O}_2$ ) thereby generating singlet oxygen ( $^1\text{O}_2$ ) [68], which is also reactive to organic pollutants. The presence of the  $\text{CoFe}_2\text{O}_4$  MNPs therefore introduces a heavy atom effect which enhances the population of the triplet

state and singlet oxygen production of the Pcs hence Pc-MNP conjugates possess greater photooxidising ability than the Pcs.

#### **6.4 Closing Remarks**

Electrospun polystyrene and polyamide-6 fibers were found to be effective in incorporating phthalocyanines,  $\text{CoFe}_2\text{O}_4$  MNPs and their respective conjugates with their photoactivity maintained. The fibers were successfully applied in the degradation of azo dyes (Methyl Orange and Orange G). The photocatalysts were also successfully applied without the support of the fibers in the treatment of both organic and inorganic water pollutants, making them promising materials for real life water purification applications.

# CHAPTER 7

## Conclusions

## **7. Conclusions and Future prospects**

### **7.1 Conclusions**

This thesis reports for the first time on the enhancement of the photophysicochemical properties of zinc Pcs after conjugation to  $\text{CoFe}_2\text{O}_4$  MNPs. The enhancement of triplet and singlet oxygen quantum yields and hence photocatalytic efficiency was generally observed to be greater when there is an amide bond linking the Pc to the  $\text{CoFe}_2\text{O}_4$  MNPs than when they are just mixed together. There is also greater enhancement with decrease in the spacer or chain length separating the Pc and  $\text{CoFe}_2\text{O}_4$  MNPs. The photocatalytic abilities of the Pc-MNP conjugates were tested using Methyl Orange and Cr(VI) as analytes with successful results.

Incorporation of the Pcs, MNPs and their respective conjugates in electrospun fibers was achieved, with their singlet oxygen generating ability and hence functionality maintained. This was proven with various microscopic and spectroscopic characterisation as well as the ability of the functionalised fibers to degrade common organic water pollutants; Methyl Orange and Orange G.

The photophysical and photocatalytic properties of Pc- $\text{CoFe}_2\text{O}_4$  MNP based photocatalysts make them promising multi-functional nanomaterials in real life water treatment.

### **7.2 Future Prospects**

The Pc- $\text{CoFe}_2\text{O}_4$  MNP based photocatalysts reported herein have been proven to be effective in the degradation of azo dyes. The study will therefore be extended to other types of organic pollutants such as phenols which are also effluents from various industries. Identification and characterisation of the products resulting from the degradation of the dyes will be performed using high precision instruments including high performance liquid chromatography (HPLC).

Due to the photoactivity of the functionalised fibers reported herein, the possibility of their applications as anti-microbial nanofabrics or as materials for the adsorption/reduction of heavy metals will also be explored in future, with the aim of creating multifunctional water purification agents.

## References:

1. M. D. Shultz, S. Calvin, P. P. Fatouros, S. A. Morrison, E. E. Carpenter, *J. Magn. Magn. Mater.* 311 (2007) 464-468.
2. V.J. Sawant, S.R. Bamane, R.V. Shejwal, S.B. Patil, *J. Magn. Magn. Mater.* 417 (2016) 222-229.
3. G.T. Nikolov, V. C. Valchev, *Procedia Earth Planet. Sci.* 1 (2009) 1357-1361.
4. R. Dom, R. Subasri, K. Radha, P.H. Borse, *Solid State Commun.* 151 (2011) 470-473.
5. J. Lou, C. Chang, *Sep. Purif. Technol.* 57 (2007) 513-518.
6. S.H. Al-Heniti, A. Umar, H.M. Zaki, G.N Dar, A.A Al-Ghamdi, S.H Kim, *J. Nanosci. Nanotechnol.* 14 (2014) 3765-3770.
7. P. Benda, A. Kalendová, *Physics Procedia* 44 (2013) 185-194.
8. D. H. Taffa, R. Dillert, A. C. Ulpe, K. C. L. Bauerfeind, T. Bredow, D. W. Bahnemann, M. Wark, *J. Photon. Energy* 7 (2016) 1-25.
9. E. Casbeer, V.K. Sharma, X. Li, *Sep. Purif. Technol.* 87 (2012) 1-14.
10. F. Azhdari, M. M. Ghazi, *Adv. Environ. Tech.* 2 (2016) 77-84.
11. P. Cheng, W. Li, T. Zhou, Y. Jin, M. Gu, *J. Photochem. Photobiol. A* 168 (2004) 97-101.
12. G. Zhang, Y. Sun, D. Gao, Y. Xu, *Mater. Res. Bull.* 45 (2010) 755-760.
13. D. Guin, B. Baruwati, S.V. Manorama, *J. Mol. Catal. A: Chem.* 242 (2005) 26-31.
14. S.K. Pardeshi, R.Y. Pawar, *Mater. Res. Bull.* 45 (2010) 609-615.
15. Y. Matsumoto, M. Obata, J. Hombo, *J. Phys. Chem.* 98 (1994) 2950-2951.
16. X. Chu, S. Liang, T. Chen, Q. Zhang, *Mater. Chem. Phys.* 123 (2010) 396-400.
17. S. Zhang, H. Niu, Y. Cai, X. Zhao, Y. Shi, *Chem. Eng. J. (Amsterdam, Neth.)* 158 (2010) 599-607.



18. D. Mishra, K. KI Senapati, C. Borgohain, A. Perumal, J. Nanotechnol. 2012 (2012) 1-6.
19. D. Greene, R. Serrano-Garcia, J. Govan, Y.K. Gun'ko, Nanomaterials 4 (2014) 331-343.
20. C. Suwanchawalit, V. Somjit, Dig. J. Nanomater. Biostruct. 10 (2015) 769 – 777.
21. A. M. Grumezescu, D. E. Mihaiescu, D. E. Mogoşanu, M. C. Chifiriuc, V. Lazăr, I. Călugărescu, V. Trăistaru, Optoelecton. Adv. Mat. 4 (2010), 1798 – 1801.
22. S. Ma, S. Zhan, Y. Jia, Q. Zhou, ACS Appl. Mater. Interfaces 7 (2015) 10576–10586.
23. Y. O. López, H. M. Vázquez, J. S. Gutiérrez, V. G. Velderrain, A. L. Ortiz, V. C. Martínez, J. Nanomater. 2015 (2015) 1-9.
24. K. Ozawa, K. Ishii, Phys. Chem. Chem. Phys. 11 (2009) 1019–1022.
25. L. Machala, J. Tucek, R. Zboril, Chem. Mater. 23 (2011) 3255–3272.
26. Y. Ao, J. Xu, D. Fu, X. Shen, C. Yuan, Sep. Purif. Technol. 61 (2008) 436–441.
27. Kadish, K.M.; Smith, K.M., Guillard, R., Eds. The Porphyrin Handbook, Vol. 15; Academic Press: San Diego, 2003.
28. N.B. McKeown, Phthalocyanine Materials: Synthesis, Structure and Function, Cambridge University Press, New York, 1998.
29. R.P. Linstead, A.R. Lowe, J. Chem. Soc. (1934) 1022-1027.
30. C. G. Claessens, U. Hahn, T. Torres, Chem. Rec. 8 (2008) 75-97.
31. H. B. Y. Smida, B. Jamoussi, J App. Chem. 2 (2012) 11-17.
32. P. Gregory, J. Porphyrins Phthalocyanines 3 (1999) 468-476.
33. A. Ogunsipe, T. Nyokong, J. Mol. Struct. 689 (2004) 89-97.
34. F.S. Damos, R. de Cassia Silva Luz, A.A. Tanaka, in Electrochemistry of N4 Macrocyclic Metal Complexes (Eds: J. H. Zagal, F. Bedioui), Springer International Publishing; 2016, pp. 201–224.

35. R. Bonnett, In *Chemical Aspects of Photodynamic Therapy*; Gordon and Breach Science, Amsteldijk, The Netherlands, 2000, 199-222.
36. M. Idowu, T. Loewenstein, A. Hastall, T. Nyokong, D. Schlettwein, J. Porphyrin Phthalocyanines, 14 (2010) 142-149.
37. D. Wöhrle, O. Suvorova, R. Gerdes, O. Bartels, L. Lapok, N. Baziakina, S. Makarov, A. Slodek, J. Porphyrins Phthalocyanines 8 (2004) 1020-1041.
38. R. P. Linstead, J. Chem. Soc. (1934) 1016-1017.
39. T. Shen, Z.-l. Yuan, H.-j. Xu, Dyes Pigm. 11 (1989) 77-80.
40. D. Atilla, V. Ahsen, J. Porphyrins Phthalocyanines 6 (2002) 593 -601.
41. W.M. Sharman, J.E. Van Lier, in: K. Kadish, K. Smith, R. Guilard (Eds.), *The Porphyrin Handbook*, Vol. 15, Academic Press, New York, 2003, pp. 1-60.
42. M. Hanack, D. Meng, A. Beck, M. Sommerauer, L.R. Subramanain, J. Chem. Soc. Chem. Commun. 58 (1953)
43. M. Sommerauer, C. Rager, M. Hanack, J. Am. Chem. Soc. 118 (1996) 10085-10093.
44. N. Kobayashi, R. Kondo, S. Nakajima and T. Osa, J. Chem. Soc. 112 (1990) 9640-9641.
45. S. Dabak, A. Gul , O. Bekaroglu, Chem. Ber. 127 (1994) 2009-2012.
46. J. Yang, T.C. Rogers, M.R. Van De Mark, J. Heterocycl. Chem. 30 (1993) 571-573.
47. J.V. Bakboord, M.J. Cook, E.J. Hamuryudan, J. Porphyrins Phthalocyanines 4 (2000) 510-517.
48. V.N Nemykin, S.V. Dudkin, F. Dumoulin, C. Hirel, ARKIVOC 2014 (2014) 142-204.
49. L. Edwards, M. Gouterman, J. Mol. Spectrosc. 33 (1969) 292-310.
50. H. Konami, M. Hatano, A. Tajiri, Chem. Phys. Lett. 166 (1990) 605-608.
51. J. Mack, M.J. Stillman, Coord. Chem. Rev. 219-221 (2001) 993-1032.
52. A. J. McHugh, M. Gouterman, J. C. Weiss, Theor. Chim. Acta 24 (1972) 346-370.

53. A.M Schaffer, M. Gouterman, E.R. Davidson, *Theor. Chim. Acta* 30 (1973) 9-30.
54. J. Mack, M.J. Stillman, *J. Am. Chem. Soc.* 116 (1994) 1292-1304.
55. H. Ali, J.E van Lier, *Chem. Rev.* 99 (1999) 2379-2450.
56. R. Bonnet, *Chem. Soc. Rev.* 24 (1995) 19-33.
57. A.C. Tadesco, J.C.G. Rotta, C.N. Lurnardi, *Curr. Org. Chem.* 7 (2003) 187-196.
58. Y. Li, T.M. Pritchett, J. Huang, M. Ke, P. Shao, W. Sun, *J. Phys. Chem .A*.112 (2008) 7200-7207.
59. O. Tsaryova, A. Semioshkin, D. Wohrle, V.I. Bregadze, *J. Porphyrins Phthalocyanines*, 9 (2005) 268–274.
60. R.O. Ogbodu, T. Nyokong, *J. Photochem. Photobiol. A: Chem.* 274 (2014) 83-90.
61. M.S. Ağırtaş, C. Karataş, S. Özdemir, *Spectrochim. Acta A Mol. Biomol. Spectrosc.* 135 (2015) 20–24.
62. L. Zhou, E. Chen, W. Jin, Y. Wang, J. Zhou, S. Wei, *Dalton Trans.* 45 (2016) 15170-15179.
63. O. L. Osifeko, T. Nyokong, *Dyes and Pigments* 131 (2016) 186-200.
64. O.L. Osifeko, I. Uddin, P.N. Mashazi, T. Nyokong, *New. J. Chem.* 40 (2016) 2710-2721.
65. P.A. Stuzhin, O.G. Khelevina, S. Angeoni, B.D. Berezin, In *Phthalocyanines: Properties and Applications*; C.C. Leznoff, A.B.P Lever, Eds.; VCH: New York, 1996; Vol. 4; pp. 19-77.
66. Gregory, P. J. *Porphyrins Phthalocyanines* 3 (1999) 468-476.
67. J.R. Lakowicz, *Principles of Fluorescence Spectroscopy*, 3<sup>rd</sup> ed., Springer, New York, 2006.
68. S.P. Stratton, D.C. Liebler, *Biochemistry* 36 (1997) 12911-12920.
69. M. Ledwaba, N. Masilela, T. Nyokong, E. Antunes, *J. Nanopart. Res.* 19 (2017) 158.

70. P. Modisha, T. Nyokong, *J. Mol. Catal. A: Chem* 380 (2013) 131-138.
71. X. Tao, W. Ma, T. Zhang, J. Zhao, *Chem. Eur. J.* 8 (2002) 1321-1326.
72. M. Ledwaba, N. Masilela, T. Nyokong, E. Antunes, *J. Mol. Catal. A: Chem.* 403 (2015) 64–76.
73. H. You, Y. Zhao, *J. Phys. Chem. Biophys.* 6 (2016) 1000199.
74. E. Marais, R. Klein, E. Antunes, T. Nyokong, *J. Mol. Catal. A: Chem.* 261 (2007) 36–42.
75. V. Iliev, A. Mihaylova, L. Bilyarska, *J. Mol. Catal. A: Chem.* 184 (2002) 121-130.
76. P. Modisha, T. Nyokong, *J. Mol. Catal. A: Chem.* 381 (2014) 132–137.
77. R. Zugle, E. Antunes, S. Khene, T. Nyokong, *Polyhedron* 33 (2012) 74-81.
78. P. Khoza, T. Nyokong, *J. Coord. Chem.* 68 (2015) 1117–1131.
79. R. Zugle, T. Nyokong, *J. Mol. Catal. A: Chem.* 358 (2012) 49-57.
80. J. M. Meichtry, V. Rivera, Y. D. Iorio, H. B. Rodríguez, E. S. Romàn, M.A. Grela, M. I. Litter, *Photochem. Photobiol. Sci.* 8 (2009) 604–612.
81. C. Albay, M. Koç, İ. Altın, R. Bayrak, İ. Değirmencioğlu, M. Sökmen, *J. Photochem. Photobiol.* 324 (2016) 117-125.
82. R. Bayrak, C. Albay, M. Koç, İ. Altın, İ. Değirmencioğlu, M. Sökmen, *Process Saf. Environ. Prot.* 102 (2016) 294-302.
83. A. Sorokin, B. Meunier, *J. Chem. Soc., Chem. Commun.* 15 (1994) 1799-1800.
84. R. Slota, G. Dydra, K. Szczegot, G. Mele, I. Pio, *Photochem. Photobiol. Sci.* 10 (2011) 361-366.
85. L. Wu, A. Li, G. Gao, Z. Fei, S. X. Q. Zhang, *J. Mol. Catal. A: Chem.* 269 (2007) 183-189.
86. A. Fashina, E. Amuhaya, T. Nyokong, *Spectrochim. Acta Mol. Biomol. Spectrosc.* 137 (2015) 294–299.

87. A. Formhals, Process and Apparatus for Preparing Artificial Threads, U.S. Patent 1,975,504 (1934).
88. J. Huang, T. You. Electrospun Nanofibers: From Rational Design, Fabrication to Electrochemical Sensing Applications, Advances in Nanofibers, (Ed.: Russel Maguire) 2013.
89. S. Maghsoodlou, B. Noroozi, A. K. Hagh, Nano. 12 (2017) 1750028-1- 1750028-12.
90. Z.M. Huang, Y.Z. Zhang, M. Kotaki, S. Ramakrishna. Compos. Sci. Technol. 63 (2003) 2223-2253.
91. T.J. Sill, H.A. von Recum, Biomaterials 29 (2008) 1989-2006.
92. D. Li, Y.N. Xia. Adv. Mater. 16 (2004) 1151-1170.
93. S. Lee, S. K. Obendorf, Text. Res. J. 77 (2007) 696-702.
94. X. Qin, S. Wang, J. Appl. Polym. Sci. 102 (2006) 1285–1290.
95. A. C. Patel, S. Li, C. Wang, W. Zhang, Y. Wei, Chem. Mater. 19 (2007) 1231–1238.
96. S. V. Rao, P.T. Anusha, L. Giribabu, S.P. Tewari, Pramana. 75 (2010) 1017–1023.
97. Y. Sha, I. Mathew, Q. Cui , M. Clay, F. Gao, X. J. Zhang, Z. Gu, Chemosphere 144 (2016) 1530-1535.
98. S. Mahmood, A. Khalid, T. Mahmood, M. Arshad, J. C. Loyola-Licea, D. E. Crowley, RSC Adv. 5 (2015) 106272–106279.
99. F. Rafii, J.D. Hall, C.E. Cerniglia, Food Chem. Toxicol. 35 (1997) 897-901.
100. H. Zollinger, Colour Chemistry - Synthesis, Properties and Applications of Organic Dyes and Pigments. VCH, New York, 1987, pp. 92-102.
101. A. Pandey, P. Singh, L. Iyengar, Int. Biodeterior. Biodegradation 59 (2007) 73–84.
102. C. Zhu, L. Wang, L. Kong, X. Yang, L. Wang, S. Zheng, F. Chen, F. Maizhi, H. Zong, Chemosphere 41 (2000) 303-309.

103. X. Lu, R. Liu (2010) Treatment of Azo Dye-Containing Wastewater Using Integrated Processes. In: Atacag Erkurt H. (eds) Biodegradation of Azo Dyes. The Handbook of Environmental Chemistry, vol 9. Springer, Berlin, Heidelberg
104. L. Young, J. Yu, *Wat. Res.* 31 (1997) 1187-1193.
105. N. Puvaneswari, J. Muthukrishnan, P. Gunasekaran, *Indian J. Exp. Biol.* 44 (2006) 618-626.
106. P. Cui, Y. Chen, G. Chen, *Ind. Eng. Chem. Res.* 50 (2011) 3947–3954.
107. A. Szyguła, E. Guibal, M. Ruiz, A.M. Sastre, *Colloids Surf. A Physicochem. Eng. Asp.* 330 (2008) 219-226.
108. B. Armağan, M. Turan, M. S. Şelik, *Desalination* 170 (2004) 33-39.
109. D. Kaušpėdienė, A. Gefenienė, E. Kazlauskienė, *Water Air Soil Pollut.* 224 (2013) 1769.
110. C. Galindo, P. Jacques, A. Kalt, *Chemosphere* 48 (2002) 1047-1060.
111. T. Ohashi, A.M.T. Jara, A.C.L. Batista, L. O. Franco, M.A.B. Lima, M. Benachour, C. A. A. da Silva, G.M. Campos-Takaki, *Molecules* 17 (2012) 14219-14229.
112. S. Chakrabarti, B. Chaudhuri, S. Bhattacharjee, A. K. Ray, B. K. Dutta, *Chem. Eng. J.* 153 (2009) 86–93.
113. S. S. Banerjee, M. V. Joshi, and R. V. Jayaram, *Sep. Sci. Technol.* 39 (2004) 1611–1629.
114. R. A. Sabty-Daily, K. K. Luk, J. R. Froines, *Analyst* 127 (2002) 852–858.
115. R. Shrivastava, R.K Upreti, P.K Seth, U.C Chaturvedi, *Pathogens and Disease* 34 (2002) 1–7.
116. G. F. Nordberg, B. A. Fowler, M. Nordberg, *Handbook on the Toxicology of Metals*, Academic Press, 4th ed. 2014.
117. T.J. O'Brien, S. Ceryak, S.R. Patierno, *Mutat. Res.* 533 (2003) 3-36.

118. B. Xie, C. Shan, Z. Xu, X. Li, X. Zhang, J. Chen, B. Pan, *Chem. Eng. J.* 308 (2017) 791-797.
119. K. Anbalagan, P. S. Kumar, R. Karthikeyan, *Desalin. Water Treat.* (2015) 1-23.
120. E. Menéndez-Alonso, S. J. Hill, M. E. Foulkes, J. S. Crighton, *J. Anal. At. Spectrom.* 14 (1999) 187-192.
121. L. Deng, Z. Shi, X. Peng, *RSC Adv.* 5 (2015) 49791–49801.
122. A. Idris, N. Hassan, N. S. M. Ismail, E. Misran, N. M. Yusof, A.-F. Ngomsik, A. Bee, *Wat. Res.* 44 (2010) 1683–1688.
123. S. Fery-Forgues, D.J. Lavabre, *J. Chem. Educ.* 76 (1999) 1260-1264.
124. S.E. Maree, D. Phillips, T. Nyokong, *J. Porphyrins Phthalocyanines* 6 (2002) 17-25
125. X.F. Wang, T. Uchida, S. Minami, *Appl. Spectrosc.* 45 (1991) 560-565.
126. H.C. Gerritse, R. Sanders, A. Draaijer, *Proc SPIE* 2329 (1994) 260-267.
127. S. M. Bachilo, R. B. Weisman, *J. Phys. Chem. A* 104 (2000) 7711-7714.
128. J.H. Brannon and D. Magde, *J. Am. Chem. Soc.* 102 (1980) 62-65.
129. M. Niedre, M.S. Patterson, B.C. Wilson, *Photochem. Photobiol.* 75 (2003) 382-391.
130. F. Wilkinson, W.P.P Helman, A.B. Ross, *J. Phys. Chem. Ref. Data* 22 (1993) 113-262.
131. C.S. Foote, in: C.J. Gomer (Ed.), *Futur. Dir. Appl. Photodyn. Ther.* SPIE Institutes Adv. Opt. Technol. Vol. IS6, Volume 6, SPIE Optical Engineering Press, 1990.
132. W. Spiller, H. Kliesch, D. Wöhrle, S. Hackbarth, B. Röder, G. Schnurpfeil, *J. Porphyrins Phthalocyanines* 2 (1998) 145-158.
133. M. Ambroz, A. Beeby, A. J. McRobert, M. S. C. Simpson, R. K. Svensen, D. Phillips, *J. Photochem. Photobiol. B: Biol.* 9 (1991) 87-95.
134. A. Fashina, E. Antunes and T. Nyokong, *Polyhedron* 53 (2013) 278–285.

135. K. Maaz, Ihsan A, Fatima I, Masood F, S. Karim., *Int. J. Nano. Stud. Technol.* 03 (2014) 55-58.
136. G. Aygar, M. Kaya, N. Ozkan, S. Kocabiyik, M. Volkan, *J. Phys. Chem. Solids.* 87 (2015) 64-71.
137. D. Biswal, B.N. Peeples, C. Peeples, A.K. Pradhan, *J. Magn. Magn. Mater.* 345 (2013) 1–6.
138. R. B. N. Baig, R. S. Varma, *Green Chem.* 14 (2012) 625-632.
139. K. Sanusi, J.M Stone, T. Nyokong, *New J. Chem.* (2014)1-13.
140. A. Ogunsipe, J.Y. Chen, T. Nyokong, *New. J. Chem.* 7 (2004) 822-827.
141. T.H. Tran-Thi, C. Desforge, C. Thiec, *J. Phys. Chem.* 93 (1989) 1226-1233.
142. S.M. Bishop, A. Beeby, A.W. Parker, M.S.C. Foley and D. Phillips, *J. Photochem. Photobiol., A. Chem.* 90 (1995) 39-44.
143. N.A. Kusnetsova, N.S. Gretsova, E.A. Kalmykova, E.A.; Makarova, S.N. Dashkevich, V.M. Negrimovsky, O.L. Kaliya, E.A. Lukyanets, *Russ. J. Chem.* 70 (2000) 133-140.
144. T. Nyokong, E. Antunes, In Chapter title: Photochemical and photophysical properties of metallophthalocyanines: *The Handbook of Porphyrin Science.* 17 Eds. Kadish, K. M.; Smith, K. M.; Guillard, R. Vol.7, chapt. 34 pp 247-349, World Scientific, Singapore, (2010).
145. A. Ogunsipe, T. Nyokong, *J. Photochem. Photobiol. A Chem.* 173 (2005) 211-220.
146. M.J. Stillman, T. Nyokong, .; in.; C.. Leznoff, A.B.. Level (Eds.), *Phthalocyanines Prop. Appl.*, VCH Publisher Inc, New York, 1989, 133–289.
147. M.O. Liu, C.H. Tai, A.T. Hu, T.H. Wei, *J. Organomet. Chem.* 689 (2004) 2138-2143.
148. L. Li, J. Zhao, N. Won, N.; H. Jin, S. Kim, J.Y. Chen, *Nanoscale Res. Lett.* 7 (2012) 386-396.



149. B.N. Achar, K.S. Lokesh, *J. Organomet. Chem.* 689 (2004) 2601–2605.
150. R. Jenkins, R.L. Snyder, *Introduction to X-ray Diffractometry*, Wiley & Sons, New York, 1996.
151. J.A. Lacey, D. Philips, *Photochem. Photobiol. Sci.* 1 (2002) 378-383.
152. S. Vukovic, S. Corni, B. Mennucci, *J. Phys. Chem. C* 113 (2009) 121–133.
153. J.A. Lacey, D. Philips, *Photochem. Photobiol. Sci.* 1 (2002) 378-383.
154. J.R. Darwent, P. Douglas, A. Harriman, G. Porter, M.C. Richoux, *Coord. Chem. Rev.* 44 (1982) 83-126.
155. E.I. Sagun, E.I. Zenkevich, V.N. Knyukshuto, A.M. Shulga, D.A. Starukhin, C. von Borczyskowski, *Chem. Phys.* 275 (2002) 211-230.
156. S. Brunauer, L. S. Deming, W. E. Deming, and E. Teller, *J. Am. Chem. Soc.* 62 (1940), 1723-1732.
157. S.J. Eichhorn, W.W. Sampson, *J. R. Soc. Interface.* 7 (2010) 641–649.
158. L. Alagna, A. Capobianchi, M.P. Casaletto, G. Mattogno, A.M. Paoletti, G. Pennesi, G. Rossi, *J. Mater. Chem.* 11 (2001) 1928–1935.
159. A. Auger, P.M. Burnham, I. Chambrier, M.J. Cook, D.L. Hughes, *J. Mat. Chem.* 15 (2005) 168-176.
160. K. Lang, J. Mosinger, D.M. Wagnerova, *Coord. Chem. Rev.* 248 (2004) 321-350.
161. M.C. Palumbo, N.A. Garcia, *Toxicol. Environ. Chem.* 17 (1988) 103-116.
162. M.A. Meetani, M.A. Rauf, S. Hisaindee, A. Khaleel, A. AlZamly, A. Ahmad, *RSC Adv.* 1 (2001) 490–497.
163. G. Fan, Z. Gu, L. Yang, F. Li, *Chem. Eng. J.* (2009) 534-541.
164. N. A. Youssef, S. A. Shaban, F. A. Ibrahim, A. S. Mahmoud, *Egypt. J. Petr.* 25 (2016) 317–321.
165. S. Al-Qaradawi, S. R. Salman, *J. Photochem. Photobiol. A* 148 (2002) 161–168.

166. P. O'Brien, Z. Ozolins, *Inorganica Chim. Acta*, 161 (1989) 261-266.
167. A. Kortenkamp, M. Casadevall, S. P. Faux, A. Jenner, R. O. J. Shayer, N. Woodbridge, P. O'Brien, *Arch. Biochem. Biophys.* 329 (1996) 199-207.
168. R. Zügler, T. Nyokong, *J. Mol. Catal. A: Chem.* 366 (2013) 247– 253.
169. S.-L. Chen, X.-J. Huang, Z.-K. Xu, *Cellulose* 18 (2011) 1295–1303.
170. N. Smirnova, Y. Gnatyuk, N. Vityuk, O. Linnik, A. Eremenko, V. Vorobets, G. Kolbasov, , *Internat. J. Mater. Eng.* 3 (2013) 124-135.
171. C.R. Chenthamarakshan, K Rajeshwar, E.J. Wolfrum, *Langmuir* 16 (2000) 2715-2721.
172. Q. Wu, J. Zhao, G. Qin, C. Wang, X. Tong, S. Xue, *Appl. Catal. B* 142 (2013) 142–148.